Spring 2014

A unified bond theory, probabilistic meso-scale modeling, and experimental validation of deformed steel rebar in normal strength concrete

Chenglin Bob Wu
Missouri University of Science and Technology, wuch@mst.edu

Department: Civil, Architectural and Environmental Engineering

A UNIFIED BOND THEORY, PROBABILISTIC MESO-SCALE MODELING, AND EXPERIMENTAL VALIDATION OF DEFORMED STEEL REBAR IN NORMAL STRENGTH CONCRETE

by

CHENGLIN WU

A DISSERTATION

Presented to the Faculty of the Graduate School of the

MISSOURI UNIVERSITY OF SCIENCE AND TECHNOLOGY

In Partial Fulfillment of the Requirements for the Degree

DOCTOR OF PHILOSOPHY

in

CIVIL ENGINEERING

2014

Approved by

Dr. Genda Chen, Advisor
Dr. Richard K. Brow
Dr. John J. Myers
Dr. Mohamed A. Elgawady
Dr. Lesley H. Sneed

ABSTRACT

Bond between deformed rebar and concrete is affected by rebar deformation pattern, concrete properties, concrete confinement, and rebar-concrete interfacial properties. Two distinct groups of bond models were traditionally developed based on the dominant effects of concrete splitting and near-interface shear-off failures. Their accuracy highly depended upon the test data sets selected in analysis and calibration. In this study, a unified bond model is proposed and developed based on an analogy to the indentation problem around the rib front of deformed rebar. This mechanics-based model can take into account the combined effect of concrete splitting and interface shear-off failures, resulting in average bond strengths for all practical scenarios. To understand the fracture process associated with bond failure, a probabilistic meso-scale model of concrete is proposed and its sensitivity to interface and confinement strengths are investigated. Both the mechanical and finite element models are validated with the available test data sets and are superior to existing models in prediction of average bond strength (< 6% error) and crack spacing (< 6% error). The validated bond model is applied to derive various interrelations among concrete crushing, concrete splitting, interfacial behavior, and the rib spacing-to-height ratio of deformed rebar. It can accurately predict the transition of failure modes from concrete splitting to rebar pullout and predict the effect of rebar surface characteristics as the rib spacing-to-height ratio increases. Based on the unified theory, a global bond model is proposed and developed by introducing bond-slip laws, and validated with testing of concrete beams with spliced reinforcement, achieving a load capacity prediction error of less than 26%. The optimal rebar parameters and concrete cover in structural designs can be derived from this study.

ACKNOWLEDGMENTS

I would like to express my sincere gratitude to Dr. Genda Chen for his great support, encouragement, and precious advices during my study at Missouri University of Science and Technology. I am also deeply grateful for the great working environment provided by Dr. Chen. It has been a pleasure and privilege to have worked with him.

Appreciation is extended to the members of advisory committee, Drs. Richard Brow, John Myers, Mohamed Elgawady, and Lesley Sneed for their valuable time, advice and effort to review this dissertation.

I also appreciate the assistance from my friends and fellow colleagues during those memorable hours inside and outside the highbay laboratory, including Mr. Jason Cox, Mr. John Bullocks, Mr. Brian Swift, Mr. Garry Abott, Mr. Christopher Gionati, Mr. W. J. Bevans, and Dr. Zhibin Lin. I would also like to acknowledge the financial support through a grant from the U.S. National Science Foundation under Award No. CMMI-0900159 and the enamel-coated rebar prepared by Pro-Perma Engineered Coating, Inc., Rolla, MO.

Finally, I would like to dedicate this work to my parents Professors Yimo Yang and Xiaoqiang Wu. It was their continuing support, understanding and love that made this work possible.

TABLE OF CONTENTS

LIST OF ILLUSTRATIONS

Page

LIST OF TABLES

Page

1. INTRODUCTION

1.1. BACKGROUND

Bond mechanism has been studied since the introduction of reinforced concrete (RC) structures. The bond performance of reinforcement in concrete not only determines the structural behavior under service load, but also influences the structural safety at critical locations. Bond mechanism of steel rebar to concrete has been intensively investigated during the past 40 years. As commonly understood, the bond strength comes from both interfacial forces (such as adhesion and friction) and mechanical interlock (for deformed bars). Dominated by the interlock action, the tensile force along the rebar direction is transferred from the rebar to surrounding concrete, which is in turn transferred into tensile stress in the hoop direction. Two groups of rebar-concrete bond models have been investigated intensively.

The first group of bond models started with Tepfers when a "hydraulic pressure" analogy was introduced to the tensile force relationship between the rebar and hoop directions (Tepfers 1973). Based on this analogy, the stress in rebar was linearly related the stress in concrete with a constant coefficient. The focus on the following bond research was thus directed to the concrete confinement strength incorporating various fracture models (Reinhardt 1992). This simplification with the "hydraulic pressure" analogy led to the conclusion that the bond strength is independent of the deformation pattern and interfacial properties, which was not in agreement with the experimental observations that the deformation pattern is essential to bond strength and the fixed ratio between the stresses in rebar and concrete is not reliable (Darwin and Graham 1993). It was further observed that the interfacial properties significantly influence the bond strength (Idun and Darwin 1999), and thus the development length for spliced reinforcement (Orangun, Jirsa, and Breen, 1977).

The second group of bond models that focus on the effects of deformation pattern and interfacial properties was represented by Cairns and Jones (1995). They considered that the concrete surrounding steel rebar is subjected to the maximum tensile stress in

hoop direction. Such a complete plastic model for concrete confinement caused inaccuracy in simulations as discussed further in the literature review section.

As an effective barrier, protective coating to steel corrosion has been increasingly used in RC structures. It can decelerate the corrosion process of steel rebar. The corrosion in rebar can potentially change the rebar-concrete bond behavior and interfacial property over time. Therefore, to understand the mechanical effects of rebar deformation and rebar-concrete interfacial property is not only interesting to academic research, but also meaningful to practical application particularly for the condition evaluation of existing RC structures. On the other hand, the "hydraulic pressure" analogy can give the overall simplified understanding of the rebar-concrete bond strength. Therefore, it is quite desirable to develop a unified bond model to logically take into account the effects of rebar-concrete interaction and concrete confinement.

1.2. LITERATURE REVIEW

1.2.1 Local Bond Behavior: Concrete Confinement Focused Studies. In 1973, Tepfers developed one of the earliest analytical solutions for the rebar-concrete bond strength of a cylindrical specimen with the hydraulic-pressure analogy (Tepfers 1973). As the rebar was pulled out of the concrete cylinder, the bursting pressure in radial direction increased rapidly. The radial cracks thus appeared from the inner face of the thick-wall cylinder surrounding the rebar and propagated outwards. The bond strength was reached when the cracks in the thick-wall cylinder exceeded a critical length and the remaining wall thickness suddenly fractured. The tangential stress in the cracked zone was evaluated from an assumed crack opening displacement (COD) as a function of the radial distance according to a softening concrete constitutive relation without the Poisson's effect. Reinhardt (1992) and van der Veen (1990) assumed a linearly-distributed tangential displacement in the cracked zone (constant tangential stress), and introduced a nonlinear softening model as a product of exponential and power functions. The softening model involved several parameters such as the fracture energy of concrete and the softening rate. To more accurately represent the nonlinear fracture processing, Rosati and Schumm (1992) introduced a parabolic tangential displacement in the cracked zone (linear tangential stress). In addition to the complexity in softening model, the aggregate

size effect on the fracture process of the cracked concrete was overestimated due to use of the maximum aggregate size. Olofsson and Ohlsson (1995) and Noghabai (1995) simplified the cracked concrete model with a linear softening formulation so that it can be easily implemented in the numerical simulation of concrete structures with spiral reinforcement.

Gambarova and Rosati (1996), Cappellini (1996), and Nielsen and Bicanic (2002) introduced an elasto-cohesive model or the so-called smeared crack model for the splitting process of a thick-walled concrete cylinder at crack locations. However, the number of radial cracks as a model parameter is difficult to determine due to the presence of micro-cracks in concrete. The same issue remained with the study by Den Uijl and Bigaj (1996) even though they established the bar and radial components of a bond stress through the bond slip along rebar ribs. Wang and Liu (2003) implemented an elasto-cohesive model with bi-linear concrete softening criteria so that the dependence on the number of radial cracks was lifted. Instead, the splitting damage in the bar direction and the tensile damage in the hoop direction were respectively averaged and smeared into the cylinder model. In comparison with Nielsen and Bicanic (2002), Wang and Liu (2003) provided a comparable bond strength when a significant number of small cracks occurred but overestimated the bond strength when the ratio between the concrete cover and rebar diameter increased.

After the bursting pressure of the thick-walled cylinder due to rebar pull-out had been determined, the rebar-concrete bond strength was evaluated by assuming a 45° bearing angle or equal to the pressure between bar and concrete (Tepfers, 1973). In comparison with experimental data, the models developed with the hydraulic pressure analogy overestimated the rebar-concrete bond strength up to 100%. Eligehausen et al. (1983) back-calculated an effective bearing angle of 26.5° to 45° by considering a plastic zone of concrete over the rebar length and 1.5 times the rebar diameter from the rebar surface, and letting the rebar-concrete bond strength equal to 0.5~1.0 times the bursting pressure as evaluated by Tepfers (1973). The hydraulic pressure analogy was also challenged by Reynolds and Beeby (1982) since the bond strength of a spliced joint of two bars in contact is less than twice as much as the bond strength of each bar as would be predicted by the hydraulic-pressure analogy.

1.2.2 Local Bond Behavior: Rebar-Concrete Interface Focused Studies. As indicated in Section 1.1, there is a need to analyze the stress state adjacent to rebar ribs in order to fully understand the rebar-concrete bond mechanics and more accurately predict the bond strength of deformed rebar in concrete. To this end, Cairns (1979) began to investigate what factors other than concrete splitting significantly contributed to the bond strength. Cairns and Jones (1995) and Cairns and Abdullah (1996) conducted a series of detailed stress analyses taking into account the rib deformation and surface condition of rebar for each experimentally-observed failure mode. For uncoated rebar, the concrete bearing angle against steel rebar was mainly related to the cohesive force of concrete. For epoxy-coated rebar, the effective bearing angle was equal to the rib face angle of rebar.

On the other hand, experimental results indicated that both the deformation pattern and surface condition of uncoated rebar affected the effective bearing angle and thus the rebar-concrete bond strength for a given failure mode of concrete crushing at the rib-front area (Choi and Lee 2002). The model by Choi and Lee (2002) still considered a constant bearing angle of 30°. In addition, the coefficient of friction at the assumed failure plane was likely between concrete and concrete and not between concrete and rebar as stated in Choi and Lee (2002). In his local bond model, Wang (2009) introduced an imaginary bar by repeatedly connecting the tip of one rib to the toe of the followed rib of rebar, corresponding to the minimum rib face angle possible in the original rebar, and accounted for partial effects of the deformation pattern and surface condition of rebar. How the fictitious rib-face angle or concrete bearing angle affects the bond strength is yet to be investigated particularly when the rib spacing-to-height ratio of rebar increases.

Cairns and Jones (1995) indicated that the two groups of bond models (concrete confinement and rebar-concrete interface focused studies) generally overestimated and underestimated the rebar-concrete bond strength, respectively, both providing limited perspectives on the overall bond behavior. In fact, CEB-FIP Task Group (2000) stated that the core of bond is a balance of the confinement strength, provided by concrete cover or transverse reinforcement, and the shear strength in the vicinity of rebar ribs. Most of the existing models included a parameter of relative rib area that is not well supported by the test results (Rehm 1957, 1961, Darwin and Graham 1993). In addition, Darwin et al. (1992) showed a slight variation of the effective bearing angle along the rebar length. The

contradiction to the fixed bearing angle theory was noticed but never explained in the literature.

1.2.3 Global Bond Behavior: Lap Splice and Development Length. Lap splices and development lengths of deformed rebar are of continuing interests to both researchers and practitioners due to their important role in structural performance. Early researchers (Chamberlin 1956, Tepfers 1973, Orangun et al. 1977) have already pointed out the complexity of bond behavior between deformed rebar and concrete in terms of non-uniform bond stress distribution over the development length, uncertain concrete bearing angle on rebar ribs, and percentage concrete confinement contribution. Based on a series of experimental studies and a regression analysis of the test data sets, several empirical equations for bond strength have been proposed by Tepfers (1973), Orangun et al. (1977), Darwin et al. (1992), Zuo and Darwin (2000), Canbay and Frosch (2005), and Esfahani and Kianoush (2005). For example, the bond strength of a splice joint was found by Zuo and Darwin (2000) to be proportional to $\sqrt[1/4]{f_c'}$, which signifies the influence of the fracture of surrounding concrete under a non-uniform bond stress distribution over the splice length. More comprehensive studies on the effects of such parameters as deformation properties and surface conditions of rebar were conducted in Darwin and Graham (1993) and Choi et al. (1991).

Based on the experimental observations and test data sets, various analytical models were proposed to explain the effects of concrete confinement and transverse shear component. In the "hydraulic pressure" analogy, concrete softening was considered to account for the effect of partial plastic confinement (van der Veen 1990, Reinhardt 1992, Rosati and Schumm 1992, Noghabai 1995, Cairns and Jones 1995, Pantazopoulou and Papoulia 2001, Nielsen and Bicanic 2002, Wang and Liu 2003). In their analytical model, Cairns and Jones (1995) considered the importance of bearing angle and deformation property effects. A similar model was used to investigate the coating effect by Cairns and Abdullah (1996). Focused on the shear component of a bond force, other models proposed by Wang (2009) and Choi and Lee (2002) were either not applicable for long development length or largely depended upon the specific set of data used. A transition method from the local (component such as rebar pullout specimens) to global (system

such as RC beams) bond behavior was proposed by Lackner and Mang (2003). Similarly, the solution to bond distribution in asymmetric structural members was proposed by linking the local bond and the bond of lapped splices in structural members (Russo et al. 2009). Although effective in establishing a direct link between local and global bond behaviors, these methods did not reflect the effects of coating and deformation patterns. This greatly undermined the value of these methods since rebar characteristics played an important role in bond failure associated with concrete splitting.

1.2.4 Finite Element Analysis. Finite element models based on damage mechanics, fracture mechanics, micro mechanics, and structural mechanics with distributed/discrete cracks and element-embedded crack-inner softening bands were proposed to understand the complex stress field and crack propagation during a debonding process under monotonic loads (CEB-FIP Task Group 2000). Finite element modeling provides the most versatile tool for the understanding of interface mechanics between deformed rebar and concrete due to complicated geometries and heterogeneous materials. Most of these models were developed for two dimensional problems; and only a few of them were intended to solve three dimensional (3D) bond problems (Darwin et al. 1994). Even in the 3D models, the fracture plane was fixed and the crack distribution highly depended upon the mesh generation rather than the fracture properties of matrix materials. Recently, a more advanced 3D finite element model was proposed to analyze the bond between corroded reinforcement and concrete (Richard et al. 2010). This model considered damage plasticity properties of the interface layer around the reinforcement and fracture properties of the matrix materials for the understanding of fracture progress. The numerical results from the 3D model agreed well with their corresponding experimental results. However, many fracture and plasticity material properties specified in the aforementioned model were difficult to obtain from experiments and the heterogeneity of matrix materials was not taken into account.

To date, it is still a challenge to develop a 3D meso-scale bond model with heterogeneous materials that require less intensive computations and with material properties that can be readily obtained from experiments. Herein, the meso-scale is referred to as elements at millimeter length scale. The size of elements is typically smaller than the characteristic length of materials (Bazant et al. 2007). At this scale, the

uncertain distribution of material properties (Yang et al. 2009) becomes critical to the understanding of the fracture process of heterogeneous brittle materials. In general, the nonlinear fracture process of heterogeneous quasi-brittle materials can be treated as the overall behavior of a collection of meso-scale elements with linear and randomly distributed material properties to failure (Romstad et al. 1974).

1.3. RESEARCH SIGNIFICANCE, OBJECTIVES, AND OUTLINE

1.3.1 Research Significance. As a naturally occurring phenomenon, corrosion causes dangerous and expensive damage in nearly every U.S. industry sector from infrastructure and transportation to production and manufacturing. According to the 2002 study by Federal Highway Administration and NACE International, the total annual direct cost of corrosion (such as structural replacement, organic coating, etc.) in the U.S. was approximately $276 billion or 3.1% of the nation's Gross Domestic Product (Koch et al. 2002). This staggering figure corresponded to a per capita cost of approximately $1,000 per person per year. Under the infrastructure category, the annual direct cost for highway bridges alone was estimated to $8.3 billion since corroded steel and steel reinforcement is responsible for approximately 15% of the structurally deficient bridges out of nearly 600,000 bridges in the National Bridge Inventory. Corrosion in transportation infrastructure is not only the main reason for substantial financial cost, but also a potential hazard to public safety and the environment.

Since 1970s, fusion-bonded epoxy coating has been widely used in bridge construction due to its effective barrier to oxygen and chloride as well as its flexibility to bend at job sites. When damaged during transportation and handling, however, epoxy coating can accelerate the corrosion of steel rebar as discovered in 1986 from the substructure of the Long Key Bridge, Florida, after five years of service. Since then, corrosion has been observed in several bridges in Virginia and other states. The relatively weak bond between the epoxy coating and its steel substrate allowed moisture trapped underneath the coating, thus spreading corrosion from the damage location.

Porcelain enamel is typically a silicate-based material that is deposited from slurries and fused at high temperature and has stable chemical properties in harsh environments such as high temperature, acid and alkaline. Enamel coating has recently been applied to

deformed rebar as a physical barrier between the steel rebar and its surrounding concrete or as a delay mechanism to the penetration of aggressive chloride ions, thus prolonging the service life of RC structures (Chen et al. 2010). Its chemical bond with steel is important for the long-term performance of structures. Overall, enamel coating can be an effective alternative to epoxy coating in protecting steel from corrosion (Tang et al. 2012, 2013).

Enamel coating can also increase the bond strength between deformed rebar and concrete while epoxy coating reduces the rebar-concrete bond strength. Through chemical reaction, the enamel coating with 50% calcium silicate particles by weight can enhance the adhesion at the rebar-concrete interface up to seven times (Yan et al. 2011). The roughened coating surface also helps enhance the friction of coated rebar to concrete. Through a series of tests, it is observed that the enhanced adhesion and friction reduces the effective bearing angle and ultimately increases the bond strength.

Rebar-concrete bond strength includes three main components: adhesion, friction, and mechanical interlock. Due to the chemical reaction of enamel with steel, the adhesion and friction components of enamel-coated rebar in concrete are more significant than those of epoxy-coated rebar (Yan et al. 2011). On the other hand, enamel coating may slightly reduce the rib heights of rebar, which potentially reduces the mechanical interlock between the rebar and concrete. To understand the relation between enamel coating and the rebar-concrete bond strength, the interfacial condition becomes very important in mechanical modeling. Furthermore, the increase in rebar-concrete interfacial strength potentially changes from a pullout to concrete splitting failure mode, thus signifying the role of concrete confinement. As a result, it is quite necessary to simultaneously investigate the effects of both concrete confinement and rebar-concrete interface mechanics in the modeling of enamel-coated rebar in concrete. The representative concrete confinement focused study (Tepfers 1973) and the representative rebar-concrete mechanics focused study by Cairns (1979) must be combined for the development of a unified rebar-in-concrete bond theory and its associated mechanical model.

Due to the complexity at the interface of enamel-coated rebar and concrete, the theoretical analysis using the first principle in engineering mechanics may not be sufficiently sophisticated enough to take into account all the important details and explain

the experimental observations. To shed insight on the interfacial mechanics and its influence on the overall rebar-concrete bond strength, finite element models at meso-scale needs to be established. Such models must be able to simulate the entire process of rebar debonding from its surrounding concrete, including post-debonding residual strength due to friction effect.

1.3.2 Research Objectives. Motivated by the desire of understanding the bond behavior between coated rebar and concrete, the main objectives of this study are:

- To develop and validate a unified rebar-concrete bond theory and its associated mechanical model to account for the effects of both concrete confinement and rebar-concrete interface mechanics.
- To apply the unified bond theory into the analysis of RC members with lap splice reinforcement and validate the deduced member behavior with experimental results from flexural tests.
- To develop and validate a finite element model of rebar-concrete components with rebar coating effects.

To achieve the above objectives, five major technical tasks were undertaken in this study, including (1) theoretical development of a unified local bond theory for RC components, (2) local bond theory validation with controlled pull-out tests, (3) transformation from local to global bond behavior for RC members and structures, (4) global bond behavior validation with beam tests, and (5) development and validation of a meso-scale finite element model for rebar-in-concrete specimens. Each task is briefly described as follows.

1.3.2.1 Unified local bond theory. In this task, a unified rebar-concrete bond model is proposed based on an analogy to the indentation of steel rebar rib into concrete. The proposed model includes key parameters such as rib spacing-to-height ratio, rib face angle, coefficient of friction, rebar-concrete adhesive, concrete compressive and shear strengths, and confinement (concrete cover to rebar diameter ratio). It can predict various failure modes as the rib spacing-to-height ratio changes. The effective bearing angle obtained from a combined effect of confinement pressure and bearing stress by ribs varies with the deformation pattern and surface condition of rebar. The proposed model is validated with a large set of test data and compared with other existing models. It is

applied to investigate the interrelation between the model parameters and failure mechanisms.

1.3.2.2 Local bond behavior and theory validation. Local bond behavior is studied with pull-out specimens, taking into account various types of rebar coating and confinement conditions. A short embedment length of rebar in concrete is adopted to achieve a uniform bond stress. Two types of concrete strengths are considered. A specially designed steel jacket is used to control the confinement on steel rebar and force the occurrence of different types of failure modes. The bond stress-slip relationship is obtained through the experiment data. Failure details such as the effective bearing angle and the number of splitting cracks are observed. The ultimate bond strength data are also used to validate the proposed unified bond theory.

1.3.2.3 Analytical model for global bond behavior. An analytical model is proposed to include the effects of rebar characteristics and coating. The confinement stress condition around multiple bars is analyzed through an equivalent elliptical hollow cylinder stress analysis. A sectional slip distribution is used to reflect the non-uniform bond stress distribution over the development length.

1.3.2.4 Global bond behavior and experimental validation. Global bond behavior is studied on both beam and column specimens with lap spliced reinforcement. The beam specimens address parameters such as coating type, confinement condition, concrete strength, rebar size, and development length. Each beam specimen is tested upside down with four-point loads so that the center reinforcement splice region is subjected to a constant moment. The failure modes and details are closely examined. Load-deflection and load-strain curves are developed to identify various limit states in the entire debonding process of rebar in concrete. Two full-scale column specimens are constructed and tested to examine the bond performance of enamel coated and uncoated rebar in column-footing joints. Load-strain curves are obtained and compared to examine the bond strength and performance. The test data is also used to validate the proposed analytical model for global bond behavior.

1.3.2.5 Probabilistic finite element model for RC components at meso-scale. Based on the meso-scale concrete model (Tang and Zhu 2003, Zhu et al. 2004), an extended 3D meso-scale damage model is proposed and developed. The proposed model

takes into account concrete and mortar heterogeneities with material properties that follow the Weibull distribution. It is used to evaluate the key material parameters such as the bond associated stiffness. The equivalent principle strain is introduced and applied as a damage criterion for different failure modes of meso-scale elements. The proposed model is validated with the experimental results reported by Yan et al. (2012) in terms of failure patterns and the relation between the bond stress and displacement. Two bond failure modes related to concrete splitting are clearly identified with the developed model.

1.3.3 Organization of Dissertation. This dissertation contains 7 chapters. Chapter 1 serves as an introduction to the milestone development of two existing bond theories, research significance, research objectives, and the scope of work. Each of Chapters 2-6 covers the works done for each of the five main technical tasks. Chapter 2 involves the theoretical development of a unified local bond theory that leads to the formulation of a general bond strength equation. Chapter 3 deals with the design, test, and analysis of pull-out specimens for the understanding of local bond behavior and for the experimental validation of the unified bond theory. Chapter 4 presents the development of an analytical model for global bond behavior by applying and extending the unified local bond theory into RC members and structures. Chapter 5 describes the experimental setup, execution, and analysis of RC beams and columns for the understanding of global bond behavior and for the validation of the analytical model for global bond. Chapter 6 introduces the development of a new probabilistic meso-scale concrete damage model and numerical simulations on the fracture process induced by debonding. Finally, Chapter 7 summarizes the major findings from this study and provides an outlook of future researches.

2. A UNIFIED LOCAL BOND THEORY WITH INDENTATION ANALOGY

2.1. ANALOGY BETWEEN DEBONDING AND INDENTATION

As indicated in Section 1.2, the effective bearing angle of concrete on rebar ribs is a key parameter to relate the rebar-concrete interfacial strength to concrete confinement effect. The bearing angle is determined by the stress field near the rebar ribs. Figure 2.1 shows half a cross section of deformed rebar with s_r and h_r representing the spacing and height of periodical ribs, respectively. As the rebar of a pull-out specimen is being pulled (downward in Figure 2.1) out of its surrounding concrete, the ribs act as a series of conical shape indenters that are pressed against concrete in their front face and separated from concrete in their back face. Therefore, an indentation analogy can be used to evaluate the near-rib stress field.

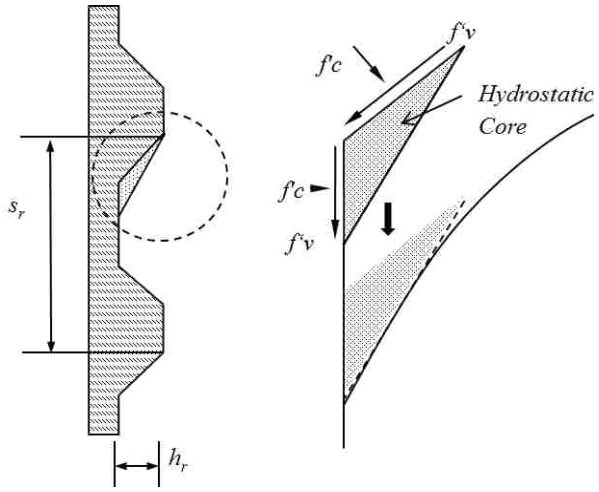

Figure 2.1. Indentation Analogy

Concrete crushing is often observed from pull-out tests in the rib front face as circled in Figure 2.1. This observation indicates the existence of a hydrostatic pressure zone near the rib-front area. Therefore, the normal component of the rebar-concrete interfacial force corresponds to the concrete compressive strength f'_c as shown in Figure 2.1. This concrete crushing zone forms a new wedge of the indenter and acts like the

"core" zone mentioned by Johnson (1985).

A classical indentation process differs from the debonding process in that:

- The rebar-concrete interface in the flat portion and the stress free back face of the ribs as indicated in Figure 2.2 do not exist in the indentation process.
- The indentation process occurs in the semi-infinite elastic body while the dedonding process often occurs in a finite body such that concrete confinement and near rib stress condition are balanced.

Despite the above difference, the stress field in the indentation problem closely resembles the near rib stress distribution in the debonding problem as schematically indicated by the indenter induced displacement field in Figure 2.1. To minimize their differences, the stress in interested area such as the back face of ribs can be modified to meet the stress free condition as indicated by the free surface Γ in Figure 2.2. In this case, the stress at the Γ surface is first calculated from the indentation solution and then cancelled by introducing a counter stress vector that is equal in magnitude and opposite in direction. Note that the key line between ribs is displayed in Figure 2.2.

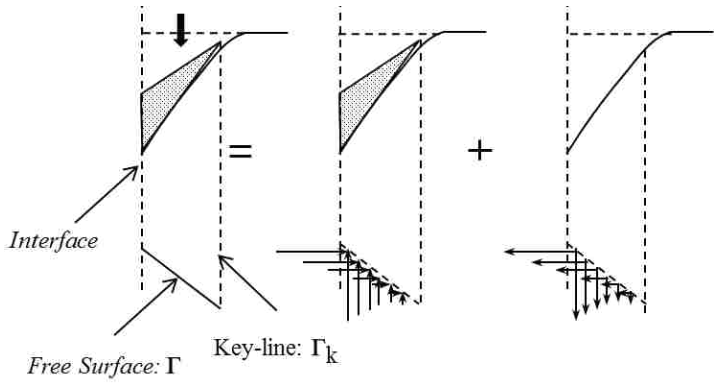

Figure 2.2. Stress Modification at the Back Face of Ribs

2.2. DEVELOPMENT OF THE NEAR-RIB STRESS FIELD

Figure 2.3 shows a conical shape indenter pressed into a semi-infinite space in the Cartesian (x, y, z) and cylindrical (r, θ, z) coordinate systems. As shown in Figure 2.3, the radius of the indenter is represented by *a*. The normal pressure and shear traction are

denoted as p_m and $c_1 p_m$, respectively. Here, c_1 represents the ratio between the shear traction and the normal pressure.

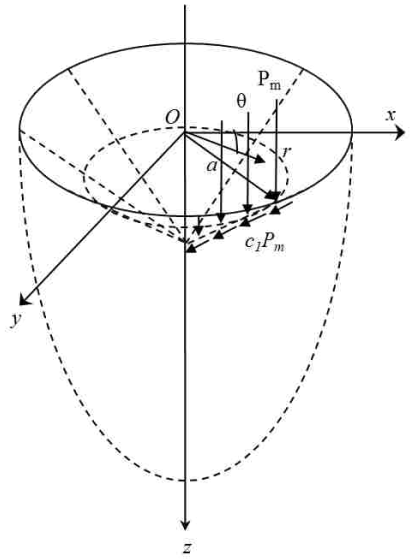

Figure 2.3. Cartesian and Cylindrical Coordinate Systems

2.2.1 Stress Induced by Normal Pressure. A semi-infinite space subjected to a conical shape indenter under uniformly distributed normal pressure is an axis-symmetrical problem studied by Sneddon (1948). The induced elastic stress field under the normal pressure p_m is thus independent of the coordinate θ. The three non-zero stress components (σ_z, σ_r, τ_{rz}) normalized by p_m can be expressed into:

$$\left[\frac{\sigma_z}{p_m}\right]_N = -[J_1^0 + \frac{z}{h_r} J_2^0] \tag{2.1}$$

$$\left[\frac{\sigma_r}{p_m}\right]_N = -\frac{2(1-\nu^2)}{(1-\nu)} J_1^0 - \left[\frac{\sigma_z}{p_m}\right]_N - \left\{2\nu J_1^0 + \frac{h_r}{r}[(1-2\nu) J_0^1 - \frac{z}{h_r} J_1^1]\right\} \tag{2.2}$$

$$\left[\frac{\tau_{rz}}{p_m}\right]_N = -\frac{z}{h_r} J_2^1 \tag{2.3}$$

where the subscript N for each normalized stress signifies the normal pressure, ν is the Poisson ratio of concrete, and various functions in Eqs. (2.1-2.3) can be evaluated by

$$J_2^0 = \left[(\frac{r}{h_r})^2 + (\frac{z}{h_r})^2 \right]^{-1/2} - \frac{\cos\phi}{c} \tag{2.4}$$

$$J_1^1 = \frac{h_r}{r}\left\{ \left[(\frac{r}{h_r})^2 + (\frac{z}{h_r})^2 \right]^{1/2} - c\cos\phi \right\} \tag{2.5}$$

$$J_2^1 = \frac{h_r}{r}\left\{ \left[1+\left(\frac{z}{h_r}\right)^2 \right]^{1/2} \frac{\cos(\vartheta-\phi)}{c} - \frac{z}{h_r}\left[\left(\frac{r}{h_r}\right)^2 + \left(\frac{z}{h_r}\right)^2 \right]^{-1/2} \right\} \tag{2.6}$$

$$J_1^0 = \frac{1}{2}\ln\left\{ \frac{c^2 + 2c\left(1+\frac{z^2}{h_r{}^2}\right)^{1/2}\cos(\vartheta-\phi)+1+\frac{z^2}{h_r{}^2}}{\left[\frac{z}{h_r}+\left(\frac{r^2}{h_r{}^2}+\frac{z^2}{h_r{}^2}\right)^{1/2}\right]^2} \right\} \tag{2.7}$$

$$J_0^1 = \frac{1}{2}\left[\frac{r}{h_r} J_1^0 + \frac{h_r}{r}(1-c\sin\phi) - \frac{z}{h_r} J_1^1 \right] \tag{2.8}$$

$$c = \left\{ \left[\left(\frac{r}{h_r}\right)^2 + \left(\frac{z}{h_r}\right)^2 - 1 \right]^2 + 4\left(\frac{z}{h_r}\right)^2 \right\}^{1/4} \tag{2.9}$$

$$\tan\vartheta = \frac{h_r}{z};\ \tan 2\phi = 2\frac{z}{h_r}\left[\left(\frac{r}{h_r}\right)^2 + \left(\frac{z}{h_r}\right)^2 - 1 \right]^{-1} \tag{2.10}$$

Note that the normal pressure p_m is related to the indentation angle α by

$$\cot\alpha = \frac{p_m 2\nu(1-\nu)}{\lambda(1-2\nu)} \tag{2.11}$$

in where $\lambda = \dfrac{E\nu}{(1+\nu)(1-2\nu)}$ is the Lame's constant, and ν is the Poisson's ratio. The indentation angle α is equal to or smaller than the rib face angle β since the crushing concrete in front of the rib face serves as part of the indentation wedge, which will be further discussed in Section 2.3.

2.2.2 Stress Induced by Shear Traction. In Sneddon's analysis, the influence of shear traction was ignored. The elastic stress field induced by a shear traction was solved by Hanson (1992) using the potential theory for transversely isotropic materials. That is,

$$\left[\frac{\sigma_z}{p_m}\right]_S = \left(\frac{\lambda\nu}{\lambda+2\nu}\right)^{1/2} c_1 z g'(z) \tag{2.12}$$

$$\left[\frac{\sigma_r}{p_m}\right]_S = -\left(\frac{\lambda\nu}{\lambda+2\nu}\right)^{-1/4} c_1^{\,2}\,\frac{(1+2\nu)g(z)+zg'(z)}{2(1-\nu)} \tag{2.13}$$

$$\left[\frac{\tau_{rz}}{p_m}\right]_S = \frac{\sqrt{2}}{4} c_1 \left\{ z\left[f_1'(z) - f_2'(z)\right] - \left[f_1(z) + f_2(z)\right]\right\} \tag{2.14}$$

where the subscript S for each normalized stress component signifies the shear traction and several functions in Eqs. (2.12-2.14) can be further expressed into:

$$g(z) = \frac{\sqrt{l_2^{\,2}(h_r) - h_r^{\,2}} - \sqrt{r^2+z^2}}{r} \tag{2.15}$$

$$f_1(z) = \ln\left[l_2(h_r) + \sqrt{l_2(h_r)^2 - r^2}\right] + \ln\left[z + \sqrt{r^2+z^2}\right] \tag{2.16}$$

$$f_2(z) = \frac{\left[2h_r^{\,2} - l_2^{\,2}(h_r)\right]\sqrt{h_r^{\,2} - l_1^{\,2}(h_r)}}{h_r r^2} + \frac{z\sqrt{r^2+z^2}}{r^2} - \frac{h_r^{\,2}}{r^2} \tag{2.17}$$

$$l_1(h_r) = \frac{1}{2}\left(\sqrt{(r+h_r)^2+z^2} - \sqrt{(r-h_r)^2+z^2}\right) \tag{2.18}$$

$$l_2(h_r) = \frac{1}{2}\left(\sqrt{(r+h_r)^2+z^2} + \sqrt{(r-h_r)^2+z^2}\right) \tag{2.19}$$

Therefore, the total stress field due to the "core" indentation can be written as a summation of the effects of both normal and shear tractions:

$$\left[\frac{\sigma}{p_m}\right]_O = \left[\frac{\sigma}{p_m}\right]_N + \left[\frac{\sigma}{p_m}\right]_S \tag{2.20}$$

Here, σ represents any stress component (σ_z, σ_r, τ_{rz}).

2.2.3 Radial Stresses along Key Line and Rebar-Concrete Interface. To cancel the stress at the free surface in Figure 2.2, the stress components at the surface is first evaluated. To this end, the free surface Γ can be mathematically described by

$$\Gamma:\ r = (z - s_r + h_r\tan\beta)\tan\beta\ ;\ \left(s_r - 2h_r\tan\beta \le z \le s_r + 2h_r\tan\beta\right) \tag{2.21}$$

By substituting Eq. (2.21) into Eq. (2.20), the stress along the free surface due to indentation can be expressed into $\left[\frac{\sigma}{p_m}\right]_{O-\Gamma}$. Therefore, the counter stress or stress modifier required to apply at the free surface is:

$$\left[\frac{\sigma}{p_m}\right]_{C-\Gamma} = -\left[\frac{\sigma}{p_m}\right]_{O-\Gamma} \tag{2.22}$$

For representative deformed rebar, the vertical stress component σ_z at the free surface is approximately 10 times as large as the radial component σ_r and the shear component τ_{zr}. Therefore, the vertical stress component represents the main stress modifier at the surface Γ.

2.2.3.1 Along the key line. The stress along the key line as shown in Figure 2.2 is equal to a superimposed effect of the indentation and the stress modifier. The stress along the key line caused by the stress modifier $\left[\frac{\sigma}{p_m}\right]_{C-\Gamma}$ can be evaluated using the Timoshenko's beam theory. As such, the total radial stress along the key line is

The stress along the key line as shown in Figure 2.2 is equal to a superimposed effect of the indentation and the stress modifier. The stress along the key line caused by the stress modifier $\left[\frac{\sigma}{p_m}\right]_{C-\Gamma}$ can be evaluated using the Timoshenko's beam theory. As such, the total radial stress along the key line is

$$\left[\frac{\sigma}{p_m}\right]\Bigg|_{r=h_r} = \left[\frac{\sigma}{p_m}\right]_O\Bigg|_{r=h_r} + \frac{12(z-\frac{s_r}{2})}{s_r^3}\int_\Gamma \left[\frac{\sigma}{p_m}\right]_{C-\Gamma} n_i\,(h_r - r)dS \tag{2.23}$$

where n_i is the directional cosine between a stress component of $\left[\frac{\sigma}{p_m}\right]_{C-\Gamma}$ and the z axis, and dS represents a infinitely small length on the rib-back face. It can be seen from Eq. (2.23) that the tensile stress generated by the boundary effect, particularly in vertical direction, can be significant when the rib spacing-to-height ratio is small.

Preliminary analysis indicates that $\left.\frac{\sigma_r}{p_m}\right|_{r=h_r,\, z\to 0}$ is approximately zero when $\frac{s_r}{h_r}$ approaches 7. When $\frac{s_r}{h_r}$ is greater than 7, the influence of the boundary Γ becomes insignificant. The radial stress is mainly determined by the indentation pressure. Furthermore, the radial stress is significant only within a distance of h_r along the vertical axis. In fact, the accumulative radial traction in this region represents approximately 77% of the total traction along the key line when $\frac{s_r}{h_r} \geq 10$. Therefore, it is reasonable to assume that the radial stress generated in the debonding process is mainly limited to the near rib area.

2.2.3.2 Along the rebar-concrete interface. The radial stress along the flat portion of rebar-concrete interface can be expressed into:

$$\left.\frac{\sigma_r}{p_m}\right|_{r\to 0} = \left.\frac{\sigma_r}{p_m}\right|_{O,\, r\to 0} \tag{2.24}$$

When $\frac{h_r}{z}$ approaches 0.1 and ν = 0.15-0.5, Eq. (2.24) results in a tensile stress of 0-0.001 p_m, regardless of the indentation angle α.

2.3. UNIFIED BOND STRENGTH FORMULATION

Based on the numerical analyses in Section 2.2, the stress distributions along various boundaries are depicted in Figure 2.4 for different rib spacing-to-height s_r / h_r ratios. The stress states near the rib areas can be divided into three groups: $s_r / h_r \leq 7$, $7 < s_r / h_r \leq 10$, and $10 < s_r / h_r$. They are briefly summarized as follows:

- For $s_r / h_r \leq 7$, the tensile stress generated along the key line may result in a tearing-off failure. The tensile stress along the rebar-concrete interface indicates no contact in the flat portion along the interface.

- For $7 < s_r / h_r \leq 10$, the radial stress generated along the key line is in compression. The integration of the radial stress along the vertical axis over a distance of h_r constitutes approximately 77% of the total integration over the entire vertical axis so that the radial stress is significant only near the ribs. The tensile stress along the interface indicates no contact between the rebar and concrete in the flat portion of rebar.
- For $s_r / h_r > 10$, the radial stress generated along the key line is in compression and concentrated in the near rib area. Part of the flat rebar region is subjected to compression, indicating that the rebar and concrete remains in contact in that area. Therefore, the bond strength contributed from the flat portion should be taken into account in this case.

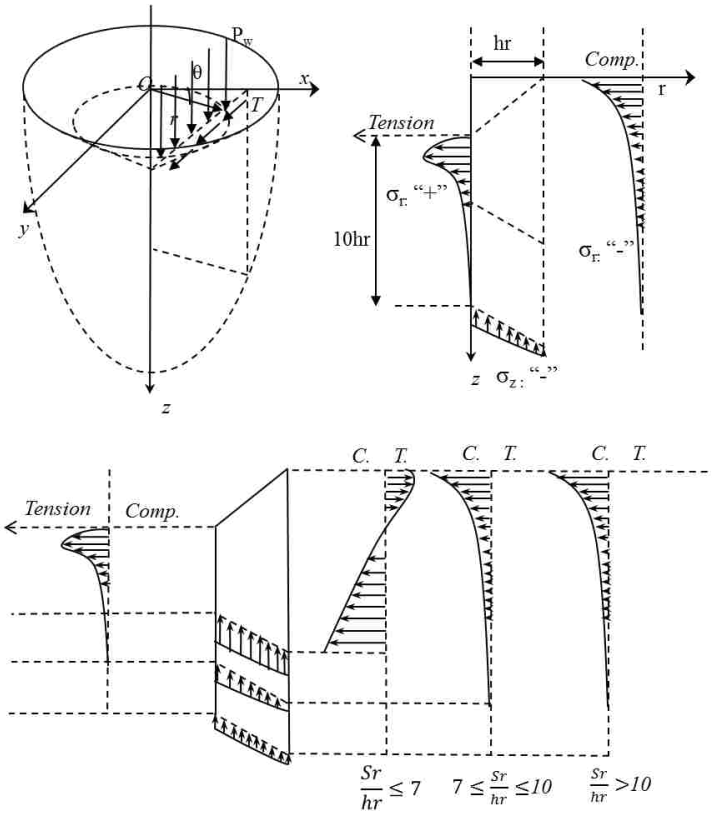

Figure 2.4. Point Loading and Stress Distributions along Boundaries

Based on the above findings, appropriate simplifications and assumptions are made to formulate the bond strength equations for the three cases that cover the entire application range in practice. These bond strength equations are detailed as follows.

2.3.1 Low Rib Spacing-to-Height Ratio: $s_r / h_r \leq 7$**.**

2.3.1.1 Failure mechanism and corresponding experimental findings. Rehm (1957, 1961) observed from various tests that the concrete at rib front underwent gradual crushing when the rib spacing-to-height ratio was lower than 7 and the rib face angle was greater than 40°. Darwin and Graham (1993) confirmed the early observation with a critical rib face angle of 60° and a rib spacing-to-height ratio lower than 7. This experimental observation can be explained by the possible concrete tearing-off along the key line as illustrated in Figure 2.5a. The torn part was gradually crushed mainly under the action of interface forces on the rib front face as shown in Figure 2.5b.

Rehm (1957, 1961) observed from various tests that the concrete at rib front underwent gradual crushing when the rib spacing-to-height ratio was lower than 7 and the rib face angle was greater than 40°. Darwin and Graham (1993) confirmed the early observation with a critical rib face angle of 60° and a rib spacing-to-height ratio lower than 7. This experimental observation can be explained by the possible concrete tearing-off along the key line as illustrated in Figure 2.5a. The torn part was gradually crushed mainly under the action of interface forces on the rib front face as shown in Figure 2.5b.

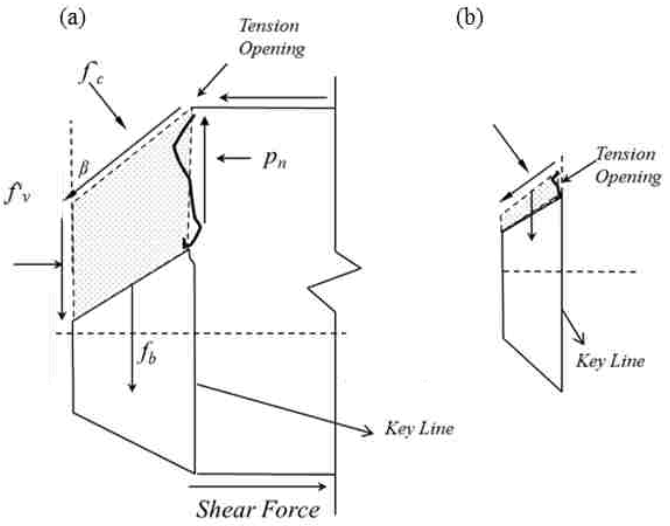

Figure 2.5. Failure Mechanism at Low Rib Spacing-to-Height Ratio (a) General Case; (b) Simplified Free Body Diagram

2.3.1.2 Critical rib face angle. Both Rehm (1957, 1961) and Darwin and Graham (1993) used a critical rib face angle as the primary condition to qualitatively explain the "plow-through" failure when the rib spacing-to-height ratio is low. The critical rib face angle exists because the pressure force along the rebar direction must be sufficiently large to ensure that the "plow through" failure can initiate and propagate through the concrete key line.

At the ultimate state immediately prior to the "plow through" failure, the bearing stress on the rib front face reaches the concrete compressive strength $f_c^{'}$. Let $c_2 = f_v' / f_c'$ be the ratio between the shear stress on the rib front face and the concrete compressive strength. Here, the uniaxial concrete strength is used since the tri-axial confinement is impossible to form due to early radial crack growth. For a low rib spacing-to-height ratio, the radial pressure p_n in Figure 2.5a is insignificant and can be neglected as a first-order approximation. Additionally, there is no contact force on the flat portion of the rebar. Therefore, the free-body diagram of the concrete key can be simplified as shown in Figure 2.5b. In this case, at the imminent "plow through" failure, the horizontal forces per linear thickness of the concrete key are in equilibrium. That is,

$$f_c^{'} S \cos\beta_{cr} - c_2 f_c^{'} S \sin\beta_{cr} = 0 \tag{2.25}$$

Yielding the following critical rib face angle β_{cr}:

$$\beta_{cr} = arc\cot(c_2) \le \beta \tag{2.26}$$

where S represents the length of the rib front face. The critical angle rib face angle must be equal to or smaller than β since the steel rib remains elastic. When $c_2 = 0.83$ (Rehm 1957, 1961), $\beta_{cr} = 50.3°$, which is less than $\beta = 60°$ widely used in representative deformed rebar.

An improvement to the above critical rib face angle estimation can be made by taking into account the effect of concrete cover by introducing a balancing pressure p_n that is uniformly distributed over the key line. In this case, the horizontal force (over a unit thickness) equilibrium equation in Eq. (2.25) becomes:

$$f_c^{'} S\cos\beta_{cr} - c_2 f_c^{'} S\sin\beta_{cr} - p_n s_{r0} = 0 \tag{2.27}$$

where $s_{r0} = s_r - s_{flat}$ and s_{flat} represents the flat portion at the tip of the rebar rib. Eq. (2.27) yields a critical rib face angle:

$$\beta_{cr} = arc\cot(c_2 + \frac{p_n}{f_c'}\frac{s_{r0}}{h_r}) \le \beta \tag{2.28}$$

When $s_{r0}/h_r = 6$ and $s_{flat} \cong h_r$, $\beta_{cr} = 44.7°$ when $p_n / f_c' = 0.03$ and $\beta_{cr} = 40°$ when $p_n / f_c' = 0.06$. To ensure that the considered balancing pressure is realistic, a thick-walled hollow cylinder with inner and outer diameters of d_b and $d_b + 2c$ (d_b = rebar diameter and c = clear concrete cover), respectively, is analyzed under internal pressure p_n. When d_b = 25.4 mm (1 in.) and c = 50.8 mm (2 in.), the internal pressure corresponding to a hoop stress equal to the tensile strength of concrete is found to be $p_n = 1.1 f_t$ (f_t is the uniaxial tensile strength of concrete). Therefore, both scenario calculations are quite possible in practical applications and the scenario analysis provides a theoretical foundation for the earlier findings by Rehm (1957, 1961).

To facilitate the understanding of the "plow through" failure mode, the initial tearing-off condition at the key line must be evaluated. At the beginning of the "plow through" failure, the concrete key remains intact and can be used as a cantilever beam to estimate the near rib stress conditions under the interface forces as shown in Figure 2.5b.

Specifically, the average shear stress σ_{rz} over the key line and the flexural tension stress σ_{rr} at the extreme fiber of the key line section can be evaluated by:

$$\sigma_{rz} = f_c^{'} \frac{h_r}{s_{r0}}(1 + c_2 \cot \beta) \tag{2.29}$$

$$\sigma_{rr} = 3 f_c^{'} (\frac{h_r}{s_{r0}})^2 (1 + c_2 \cot \beta) \tag{2.30}$$

The shear strength is equal to $0.5 f_t$ for a uniaxial stress state and f_t for a pure shear stress state. For a less conservative estimate, the shear strength equal to f_t is considered. Therefore, the shear-to-flexural stress ratio can be expressed into a function of s_{r0} / h_r by:

$$\frac{\sigma_{rz}}{\sigma_{rr}} = \frac{s_{r0}}{3h_r} \tag{2.31}$$

When s_{r0} / h_r changes from 2 to 6, shear failure governs between 3 and 6, and flexural failure controls between 2 and 3. However, $s_{r0} / h_r < 3$ is impractical in applications. Therefore, the "plow through" failure mode is accompanied by the shear failure along the key line. Note that if the lower shear strength $0.5 f_t$ was used, the shear failure along the key line would always govern.

Based on various tests (Idun and Darwin, 1999; Wu et al., 2012), the average c_2 values of fusion-bonded epoxy-coated, uncoated, and enamel-coated rebar in normal strength concrete are approximately 0.52, 0.6, and 0.7. According to Eq. (2.26), their corresponding critical rib face angles β_{cr} are 63°, 59°, and 55°, respectively.

2.3.1.3 Bond strength. Corresponding to Eq. (2.25), the total vertical forces per linear thickness of the concrete key, prior to the imminent "plow through" failure, are equal to $f_c^{'} S \sin \beta + c_2 f_c^{'} S \cot \beta = f_c^{'} h_r (1 + c_2 \cot \beta)$. Therefore, the average bond strength $\overline{f}_b$ over the rib spacing s_r due to the "plow through" failure can be estimated by

$$\overline{f}_b = f_c^{'} \frac{h_r}{s_r}(1 + c_2 \cot \beta) \tag{2.32}$$

To ensure a "plow through" failure, concrete confinement must be sufficient to prevent the splitting failure due to the excessive hoop tension stress. The minimum radial

pressure $p_{n,\min}$ can be determined by equating the friction on the key line caused by the radial pressure to the bond strength in Eq. (2.32). That is,

$$\overline{f}_b = p_n \mu_{cc} \tag{2.33}$$

where μ_{cc} is the coefficient of friction between crushed and uncrushed concrete, which is taken to correspond to an internal friction angle of 30° similar to the concrete and soil interface. Eq. (2.33) results in

$$p_{n,\min} = f_c' \frac{h_r}{s_r} \frac{(1+\cot\beta_{cr}\cot\beta)}{\mu_{cc}} \tag{2.34}$$

When the confinement induced radial stress is smaller than $p_{n,\min}$, the concrete key cannot be fully crushed before concrete splitting occurs. For a representative case when $\beta = 60°$, $\mu_{cc} = 0.4$, $s_r / h_r = 7$, $f_c^{`} = 34$ MPa (5,000 psi), Eq. (2.34) gives a minimum confining radial stress of $p_{n,\min} = 16$ MPa (2,320 psi), which corresponds to a concrete cover-to-rebar diameter ratio of approximately 1.8. Therefore, "plow through" failure will not occur when the concrete cover-to-rebar diameter ratio is less than 1.8.

2.3.2 Medium Rib Spacing-to-Height Ratio: $7 < s_r / h_r \le 10$ **.**

2.3.2.1 Failure mechanism and corresponding experimental findings. As the rib spacing-to-height ratio falls into a medium range of 7 to 10, the shear mechanics dominates the bond behavior of rebar in normal strength concrete. In this case, the force equilibriums in two orthogonal directions are used to determine the effective bearing angle. Depending upon the shear strength and confinement level, the effective bearing angle varies and leads to different failure patterns.

Previous researches showed that the concrete at the rib-front area becomes "compact powder" due to high stress concentration (Lutz and Gergely 1967, Esfahani and Rangan 1998). It was found that the effective bearing zone plays a critical role in transferring the bearing component of bond forces to their surrounding concrete.

2.3.2.2 Existence of crushing zone. The cross section of half a reinforcing bar with a crushing zone at the rib-front area is presented in Figure 2.6. Possible failures in this case include three cases: (1) rib sliding, (2) concrete crushing, and (3) concrete shear-off. The conditions for various failure modes to occur are discussed below.

In the case of concrete crushing as shown in Figure 2.6, all the forces applied on the crushed zone (shaded area in Figure 2.6) must be in equilibrium along the normal and tangential directions of the sliding plane, respectively. That is,

$$-f_{c1}S_1\cos(\beta-\alpha)+f_{v1}S_1\sin(\beta-\alpha)-f_{c2}S_2\cos\alpha-f_{v2}S_2\sin\alpha+f_nS_3=0 \tag{2.35}$$

$$-f_{c1}S_1\sin(\beta-\alpha)-f_{v1}S_1\cos(\beta-\alpha)+f_{c2}S_2\sin\alpha-f_{v2}S_2\cos\alpha+f_vS_3=0 \tag{2.36}$$

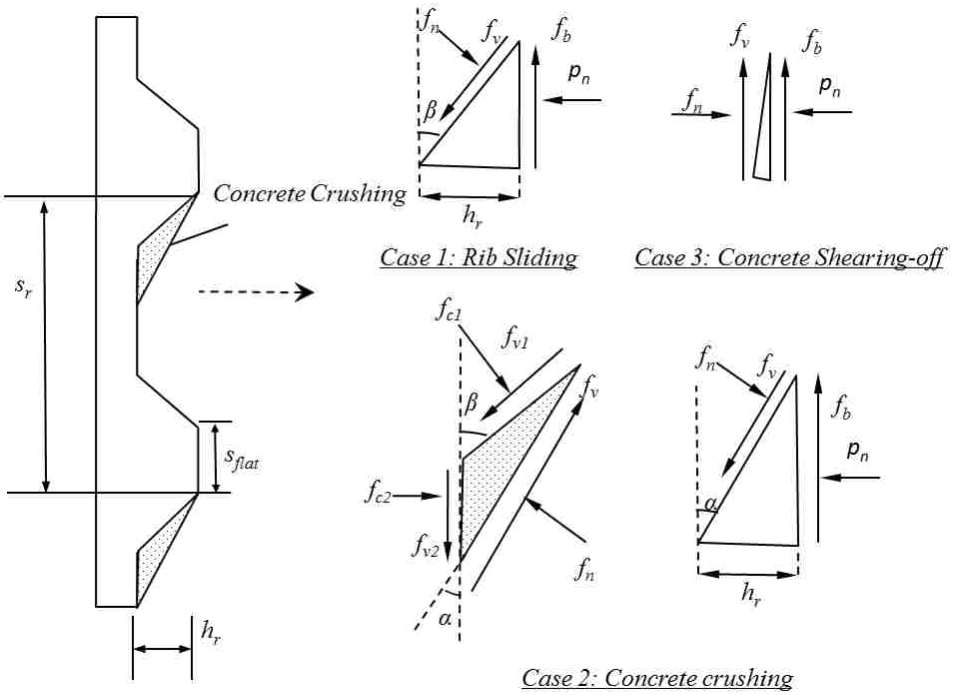

Figure 2.6. Failure Mechanism at Medium Rib Spacing-to-Height Ratio

After introducing the geometrical relations: $S_2\sin\alpha=S_1\sin(\beta-\alpha)$ and $S_1\cos(\beta-\alpha)+S_2\cos\alpha=S_3$, Eq. (2.35) and Eq. (2.36) can be simplified into:

$$f_n=f_{c1}+\frac{S_2}{S_3}[(f_{c2}-f_{c1})\cos\alpha+(f_{v2}-f_{v1})\sin\alpha] \tag{2.37}$$

$$f_v=f_{v1}+\frac{S_2}{S_3}[-(f_{c2}-f_{c1})\sin\alpha+(f_{v2}-f_{v1})\cos\alpha] \tag{2.38}$$

where S_1, S_2, and S_3 are the areas of various surfaces as shown in Figure 2.7. For simplicity, let $f_{c1} = f_{c2} = f_c^{'}$ and $f_{v1} = f_{v2} = c_2 f_c^{'}$. Eqs. (2.37) and (2.38) then become $f_n = f_c'$ and $f_v = c_2 f_c'$.

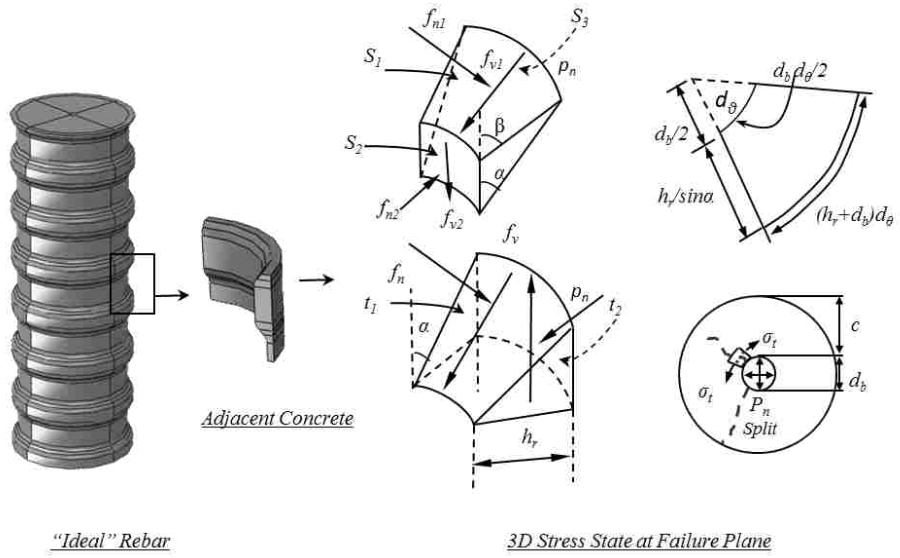

Figure 2.7. Surface Areas and Near-rib versus Confinement Stress

The radial and vertical force equilibriums of the uncrushed part of the rib-front area in Figure 2.6 respectively yield

$$f_c^{'} t_1 \cos\alpha - c_2 f_c^{'} t_1 \sin\alpha - p_n t_2 = 0 \tag{2.39}$$

$$-f_c^{'} t_1 \sin\alpha - c_2 f_c^{'} t_1 \cos\alpha - f_b t_2 = 0 \tag{2.40}$$

where t_1 and t_2 are the areas of the free-body diagram as illustrated in Figure 2.7, $\bar{f}_b$ represents the average bond strength over the rib spacing s_r, $t_2 = t_1 \cos\alpha$, and $\bar{f}_b s_r = f_b t_2$. Let $c_0 = p_n / f_c^{'}$ be the ratio between the radial pressure applied on the key line and compressive strength of concrete. Eqs. (2.39) and (2.40) lead to:

$$\alpha = \arctan\left(\frac{1-c_0}{c_2}\right), \quad \frac{f_b}{f_c^{'}} = c_2 + \tan\alpha, \quad \frac{\bar{f}_b}{f_c^{'}} = \frac{h_r}{s_r}\left(1 + c_2 \cot\alpha\right) \tag{2.41}$$

Whether the crushing zone exists or not mainly depends on the relation between the calculated α and the β value. When $\alpha < \beta$, the crushing zone is present and α can be determined by both c_0 and c_2 from Eq. (2.41). For the three cases in Figure 2.6, failure can occur inside the concrete $c_2 = c_{concrete}$ related to the cohesion and internal friction angle and at the rebar-concrete interface $c_2 = c_{interface}$ related to the coefficient of friction. Following is a brief summary of the effective bearing angle α and the average bond strength $\bar{f}_b$ in three cases as illustrated in Figure 2.6:

Case 1: Rib sliding ($\alpha \geq \beta, c_2 \leq (1-c_0)\cot\beta$)

The pull-out specimen fails at the rebar-concrete interface. By replacing f_c' and $f_{v1} = c_2 f_c'$ with f_n and $f_v = c_2 f_n$, $c_0 = p_n / f_n$, and letting $\alpha = \beta$, Eqs. (2.39) and (2.40) result in

$$\alpha = \beta \text{ and } \frac{\bar{f}_b}{p_m} = \frac{h_r}{s_r}\frac{1 + c_2 \cot\beta}{c_0} \tag{2.42}$$

For a weak rebar-concrete interface, the bond strength is governed by the interface contact strength prior to concrete splitting and the effective bearing angle is equal to the rib face angle.

Case 2: Concrete crushing ($\alpha < \beta,\ (1-c_0)\cot\beta < c_2 = c_{interface} < c_{concrete}$)

$$\alpha = \arctan\left(\frac{1-c_0}{c_2}\right) \text{ and } \frac{\bar{f}_b}{f_c'} = \frac{h_r}{s_r}\left(1 + c_2 \cot\alpha\right) \tag{2.43}$$

For a relatively weak interface, the concrete near the rib face crushed prior to concrete splitting failure and the bond strength is governed by the confinement effect. The higher interface bond corresponds to a lower effective bearing angle.

Case 3 Concrete shear-off ($\alpha < \beta, (1-c_0)\cot\beta < c_2 = c_{concrete} < c_{interface}$)

$$\alpha = \arctan\left(\frac{1-c_0}{c_2}\right) \text{ and } \frac{\bar{f}_b}{f_c'} = \frac{h_r}{s_r}\left(1 + c_2 \cot\alpha\right) \tag{2.44}$$

For a strong interface, the bond strength is governed by first the concrete shear along part of the key line, like a block shear failure, and then concrete splitting. As the concrete confinement increases, the effective bearing angle tends to decrease to zero and the

concrete key starts to shear-off. In the extreme case when $\alpha = 0$, $c_0 = 0$ or p_n approaches $f_c^{'}$, transforming from an overall concrete splitting to a pure pull-out failure.

2.3.3 High Rib Spacing-to-Height Ratio: $10 < s_r / h_r$**.**

2.3.3.1 Failure mechanism and corresponding experimental findings. Based on the stress analysis conducted in Section 2.2.3, the flat portion of rebar can be divided into non-contact and contact areas. The effect of the contact area on the bond strength must be taken into account. Experimental results confirmed that the bond strength was underestimated when only the rib effect was considered (Darwin and Graham 1993).

Based on the stress analysis conducted in Section 2.2.3, the flat portion of rebar can be divided into non-contact and contact areas. The effect of the contact area on the bond strength must be taken into account. Experimental results confirmed that the bond strength was underestimated when only the rib effect was considered (Darwin and Graham 1993).

As shown in Figure 2.8a, one part of the flat portion ($s_{r0-1} = 10h_r$) near the rib front face is dealt with in the same way as considered in Section 2.3.2. Another part of the flat portion ($s_{r0-2} = s_{r0} - s_{r0-1}$) near the rib back face was considered as a smooth rebar without any ribs. The remaining flat portion is assumed in non-contact with concrete, thus subjected to no stress. For deformed rebar with a rib spacing-to-height ratio of over 10, the tip of each rib is $s_{flat} \le 2h_r$. The average bond strength can then be obtained from the following weighted summation:

$$\overline{f}_b = \frac{1}{s_r}\left[\, \overline{f}_{b-rib} 10h_r + (s_{r0} - 10h_r)\, \overline{f}_{b-flat} \,\right] \tag{2.45}$$

where $\overline{f}_{b-rib}$ and $\overline{f}_{b-flat}$ represent the average bond strengths due to the rib and flat effects, respectively. The rib effect $\overline{f}_{b-rib}$ can be estimated from Section 2.3.2 with a rib spacing equal to $10h_r$, and a coefficient of friction between the rebar and concrete $\mu_{cs} = 0.53$ for uncoated rebar, $\mu_{cs} = 0.46$ for epoxy-coated rebar; and $\mu_{cs} = 0.53$ for enamel-coated rebar.

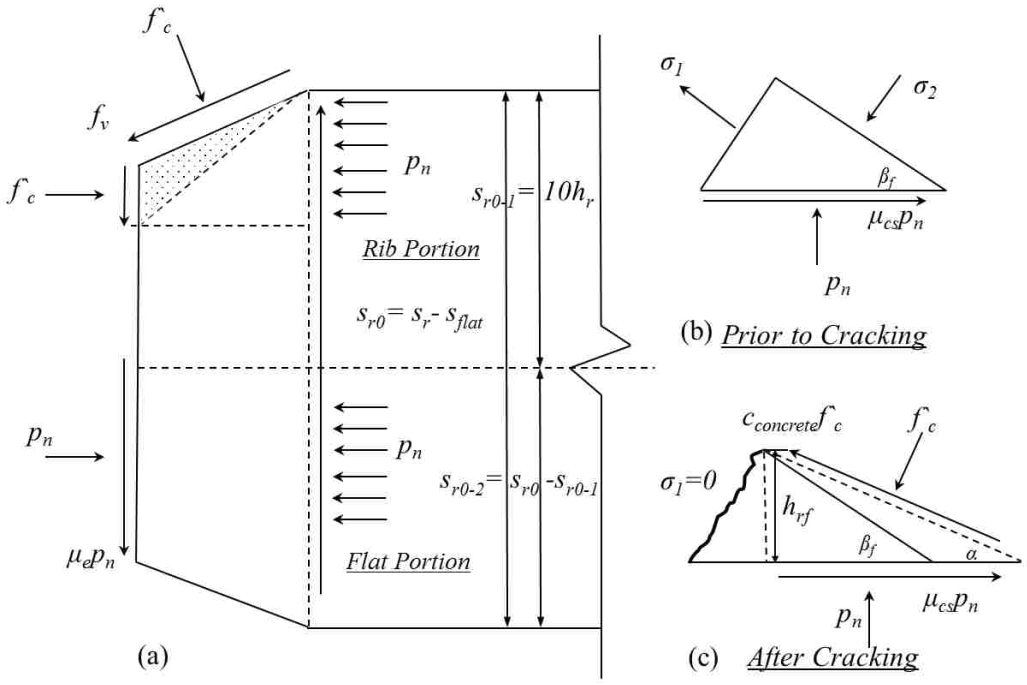

Figure 2.8. Failure Mechanism at High Rib Spacing-to-Height Ratio: (a) Overall Free-body Diagram, (b) and (c) Prior- and Post-cracking Stress State on the Flat Portion

The flat portion effect $\overline{f}_{b-flat}$ can be calculated as follows. Tepfers (1973) analyzed the bond strength of smooth rebar in concrete. However, the rebar-concrete interface mechanics was not taken into account in his analysis. In this study, the Mohr-Coulomb failure criterion is considered at the rebar-concrete contact surface as shown in Figure 2.8c.

When rebar starts slipping against its surrounding concrete, the axis of principal stress is in an angle of $\beta_f = 0.5 \arctan(2\mu_{cc})$ with the radial pressure p_n. It should be noted that μ_{cc} includes the effects of both cohesion and friction forces though the latter is emphasized here. Due to low tensile strength of concrete, σ_1 in Figure 2.8b rapidly drops to zero. At the ultimate state, the free-body diagram is shown by the dashed lines in Figure 2.8c. The effective bearing angle α is achieved when the stress along the sliding plane reaches the concrete shear strength $c_{concrete} f_c^{'}$. If a sufficient concrete cover is provided, the bearing pressure σ_2 will eventually reach $f_c^{'}$ as shown in Figures 2.8b and

2.8c.

2.3.3.2 Bond strength of the Flat Portion. As shown in Figure 2.8c, the force equilibrium equations in the normal and tangential directions of the sliding plane can be written as:

$$p_n \mu_{cs} \frac{h_{rf}}{\tan\alpha} - f_c' h_{rf} - c_{concrete} f_c' h_{rf} \cot\alpha = 0 \tag{2.46}$$

$$p_n \frac{h_{rf}}{\tan\alpha} - f_c' h_{rf} \cot\alpha + c_{concrete} f_c' h_{rf} = 0 \tag{2.47}$$

where h_{rf} is a fictitious rib height that is different from h_r. The ratio between the confinement pressure and concrete strength $\bar{c}_0 = p_n / f_c'$ and $\tan\alpha$ can thus be evaluated by

$$\bar{c}_0 = \frac{1 + c^2_{concrete}}{1 + c_{concrete}\mu_{cs}} \tag{2.48}$$

$$\tan\alpha = \frac{1 - \bar{c}_0}{c_{concrete}} \tag{2.49}$$

Typically, $\mu_{cs} = 0.53$ is smaller than $\mu_{cc} = \tan 30° = 0.58$, and $c_{concrete} = 0.25 + \mu_{cc} = 0.83$ (Cairns and Abdullah 1996). In this case, $\bar{c}_0 = 1.14$ from Eq. (2.48) and $\tan\alpha$ in Eq. (2.49) is negative, which is meaningless in application. This result means that the rebar tends to slip from the concrete before concrete crushing occurs. For a splitting associated failure, the average bond strength of the flat portion is approximately equal to the friction force related to the actual normal stress:

$$\bar{f}_{b-flat} \approx \mu_{cs} p_{n-actual} = \mu_{cs} c_0 f_c' \tag{2.50}$$

2.3.4 Maximum Radial Pressure. The average bond strengths in the three cases discussed in Sections 2.3.1-2.3.3 are all related to the radial pressure p_n or the maximum p_0 in Figure 2.9. To evaluate the radial pressure associated with concrete cover, a plane strain axisymmetric problem with a hollow cylinder is considered as shown in Figure 2.9. The cylinder can be divided into two parts: inner inelastic and outer elastic regions. The inner inelastic region included many axis-symmetrically distributed

radial cracks that cause tension softening in concrete. In this study, the tension softening is accounted for using the smeared crack model (Hillerborg et al. 1976).

In the inelastic region, the tangential/hoop stress-strain ($\sigma_t - \varepsilon_t$) relation is shown in Figure 2.9, including low-strain elastic and high-strain inelastic behaviors. It can be mathematically expressed into:

$$\sigma_t = \begin{cases} E_c \varepsilon_t, & \varepsilon_t \le \varepsilon_{t0} \\ f_{tu} \exp[-(\varepsilon_t - \varepsilon_{t0}) / (\varepsilon_{tu} - \varepsilon_{t0})], & \varepsilon_{t0} \le \varepsilon_t \le \varepsilon_{tu} \end{cases} \tag{2.51}$$

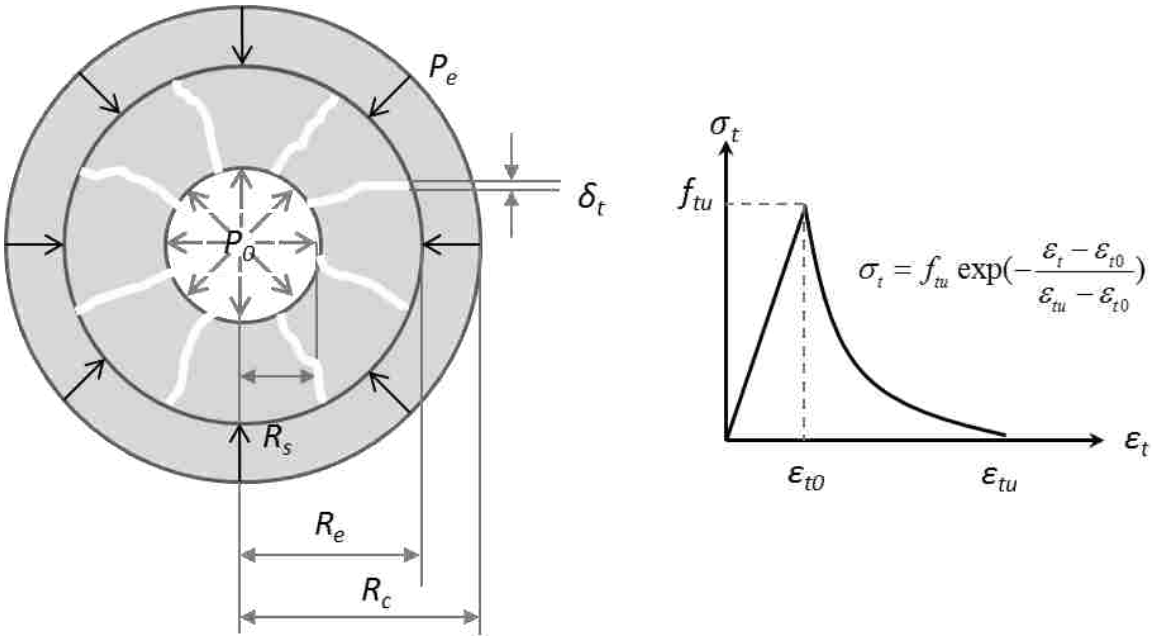

Figure 2.9. Softening Behavior of Concrete Cover

where f_{tu} is the ultimate tensile stress corresponding to the maximum elastic strain in concrete ε_{t0} (=0.0001), and ε_{tu} (=0.002) is the ultimate tangential strain. Let a tangential strain of $\varepsilon_t^{(e)}$ at the crack front be equivalent to the effect of radial cracks in the smeared crack model. The radial displacement can then be approximated by $u_r = r_e \varepsilon_t^{(e)}$. If the radial displacement is considered as a constant in the cracked concrete, the tangential strain is inversely proportional to the radial distance r ($r_0 \le r \le r_e$). That is, $\varepsilon_t = \frac{r_e}{r} \varepsilon_t^{(e)}$.

Take an infinitesimal element in the inner inelastic region. The force equilibrium in the radial direction gives the following equation:

$$p_0 r_0 = p_e r_e + \int_{r_0}^{r_e} \sigma_t dr \tag{2.52}$$

The outer elastic region is a hollow cylinder under internal pressure p_e. The inner and outer radii of the hollow cylinder are r_e and r_c. In this case, the classical Lame's solution relating the internal pressure p_e to the maximum tangential stress f_{tu} at $r = r_e$ can be written as:

$$p_e = f_{tu} \frac{r_c^2 - r_e^2}{r_c^2 + r_e^2} \tag{2.53}$$

Therefore, Eq. (2.52) corresponding to the tensile strength f_{tu} of concrete at $r = r_e$ becomes:

$$p_0 = f_{tu} \frac{r_e}{r_0} \frac{r_c^2 - r_e^2}{r_c^2 + r_e^2} + \int_{r_0}^{r_e} \sigma_t \frac{dr}{r_0} \tag{2.54}$$

Hence, the maximum p_0 is achieved when the first derivative of Eq. (2.54) with respect to is set to zero. The corresponding length of the radial crack is referred to as the critical radial crack length, which can be found from the following characteristic equation:

$$\frac{r_c^4 - 5r_e^4}{(r_c^2 + r_e^2)^2} + \frac{\sigma_t(\varepsilon_t^{(e)})}{f_{tu}} = 0 \tag{2.55}$$

in which $\sigma_t(\varepsilon_t^{(e)})$ represents the tangential stress σ_t at $\varepsilon_t = \varepsilon_t^{(e)}$ in Eq. (2.51). After obtaining the critical radial crack length, the maximum radial pressure max p_0 can be obtained from Eq. (2.54). According to Section 2.1, the radial pressure due to pulling deform rebar out of concrete is mostly concentrated within a depth of h_r along the key line as also observed experimentally by Losberg and Olsson (1979) and Soretz and Holzenbein (1979). Therefore, the effective average radial pressure $p_n \approx \max p_0$.

2.3.5 Model Parameters. As discussed in Sections 2.3.1-2.3.4, the effective bearing angle and the average bond strength mainly depend on rebar geometric parameters ($d_b, \beta, h_r, s_r, s_{flat}$), concrete geometric parameters (c, c_x, c_y), concrete material parameters ($f_c^{'}, c_2, c_0, c_{concrete}$), and interface properties ($c_2, c_{interface}$). Note that

$c_{interface}$ and $c_{concrete}$ represent both cohesion and friction effects for rebar-concrete interface and concrete shear surface, respectively. The Mohr-Coulomb failure criterion can be used to obtain these parameters. Based on the previous research (Cairns and Abdullah 1996), the cohesion force of concrete is estimated to be $0.25 f_c'$, and the internal frictional angle is 30°. These parameters correspond to $c_{concrete} = 0.83$. For the interface between uncoated rebar and concrete, $c_{interface-steel} = 0.6$ (cohesion $= 0.11 f_c'$ and frictional angle = 28°). For the interface between epoxy-coated rebar and concrete, $c_{interface-epoxy} = 0.52$ (cohesion = $0.06 f_c'$ and frictional angle = 25°). For the interface between enamel-coated rebar and concrete, $c_{interface-enamel} = 0.7$ (cohesion = $0.17 f_c'$ and frictional angle = 28°).

2.4. MODEL VALIDATION AND COMPARISON

2.4.1 Test Database and Competing Methods. Experimental data from beam-end and cylinder specimens are used to validate the theoretical model and compare its performance with existing models. Although most of the beam-end specimens have an embedment length of over five times the diameter of rebar and thus may result in non-uniform bond behavior, they are still included in the database due to wide applications and adoptions by many researchers. More importantly, prior research findings (Tepfers 1973, Esfahani and Kianoush 2005) indicated that the average bond strength of long embedment specimens may only be increased by 1.5%.

The selected experimental data (Choi et al. 1991, Darwin and Graham 1993, Idun and Darwin 1999, Miller et al. 2003, De Anda et al. 2004, Wu et al. 2012) were obtained mainly from local bond tests with concrete cover splitting as a primary failure mode. Overall, the collected database resulted from a total of 284 tests, each repeated with at least two samples. The data base covers various test parameters such as rebar size, rib geometry, coating type, concrete strength, and concrete cover.

Both empirical approaches (Orangun et al. 1977, Zuo and Darwin, 2000) and theoretical approaches (Wang 2009, Wang and Liu 2003) are considered for comparison. As the state-of-the-art methodologies in bond strength determination, Wang (2009) and

Wang and Liu (2003) was focused on the shear component and the "hydraulic pressure" analogy, respectively.

2.4.2 Test-over-Prediction Ratio of Bond Strength.

2.4.2.1 Bond of uncoated rebar in concrete. The test-over-prediction bond strength ratios of uncoated rebar in concrete by various researchers are compared in Table 2.1. Both the mean and the coefficient of variation (COV) of various bond models using individual data sets and the overall database are presented in Table 2.1. When all the test data sets were used, this study among all the bond models resulted in a mean ratio of 1.019, closest to one, with the smallest COV value and thus the most accurate prediction in bond strength of uncoated rebar in concrete. The theoretical approach taken by Wang (2009) yielded the second most accurate prediction. The empirical approach by Orangun et al. (1977) led to the least accurate results. Overall, the theoretical approaches including this study are more accurate than the empirical approaches since empirical models lack solid mechanics basis and are thus less versatile in predicting bond behaviors under different conditions investigated by various researchers. The theoretical approach by Wang and Liu (2003) resulted in a non-conservative prediction as they neglected the effect of rebar surface characteristics such as rib geometries and interface bond strength.

The mean test-over-prediction bond strength ratios of various models are also presented in Figure 2.10 using sixe data sets. It can be observed from Figure 2.10 and Table 2 that Orangun et al. (1977) used data sets developed by others and predicted the least accurate bond strength against every data set among all the models. On one hand, the two most accurate predictions by Zuo and Darwin (2000) corresponded to the data sets developed by the same group (Idun and Darwin 1999, Miller et al. 2003). On the other hand, the least accurate prediction by Zuo and Darwin (2000) was also for the data set generated by the same group (Darwin and Graham 1993). Therefore, the prediction accuracy by empirical approaches most likely depended on the test conditions and data sets used in the regression analysis.

Table 2.1. Test-over-Prediction Bond Strength Ratios of Uncoated Rebar in Concrete

Data Set	No. of Tests	Bond Ratio	Orangun et al. (1977)	Zuo and Darwin (2000)	Wang (2009)	Wang and Liu (2003)	This Study
Choi et al. (1991)	29	Mean	1.491	1.247	1.050	0.709	1.004
		COV	0.184	0.187	0.122	0.086	0.069
Dawrin and Graham (1993)	33	Mean	1.479	1.432	1.024*	0.614	1.060
		COV	0.106	0.103	0.086	0.214	0.064
Idun and Darwin (1999)	14	Mean	1.432	1.090	1.150	0.715	0.963
		COV	0.221	0.173	0.146	0.093	0.096
Miller et al. (2003)	35	Mean	1.603	1.095	0.983	0.820	0.974
		COV	0.208	0.103	0.080	0.054	0.103
De Anda et al. (2004)	10	Mean	1.497	1.135	0.965	0.794	1.055
		COV	0.163	0.237	0.091	0.028	0.061
Wu et al. (2012)	12	Mean	1.384	0.724	1.148	0.723	1.041
		COV	0.232	0.262	0.156	0.114	0.036
All	133	Mean	1.481	1.121	1.053	0.729	1.019
		COV	0.186	0.201	0.114	0.098	0.069

*only applicable with a rib spacing-to-height ratio of 10 to 12 with 13 test specimens

Among the three theoretical approaches, the proposed model in this study is most flexible and applicable to various conditions. Wang (2009) did not take full consideration of plastic behaviors during concrete splitting, resulting in a prediction that is insensitive to the variation in confinement extent (Wu et al. 2012). Wang and Liu (2003) neglected the effects of rebar surface characteristics such as rib geometries and interface bond strength. Furthermore, most theoretical approaches failed to distinguish various failure modes associated with different deformation patterns.

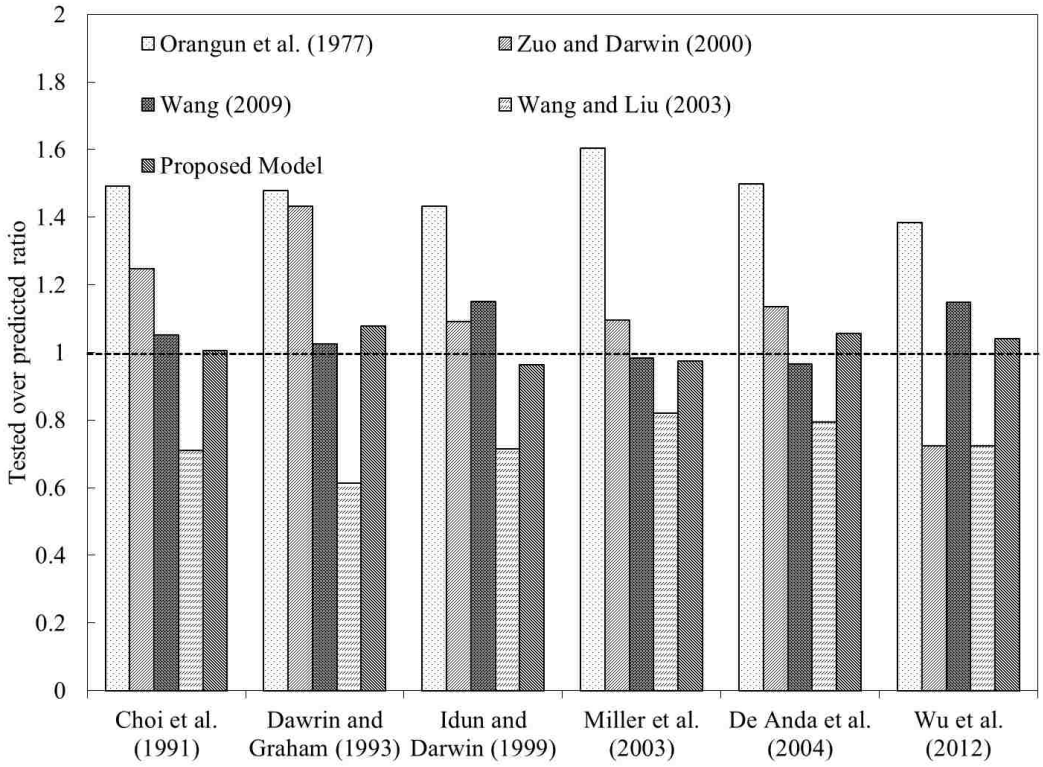

Figure 2.10. Test-over-Prediction Bond Strength Ratios for Uncoated Rebar

2.4.2.2 Bond of coated rebar in concrete. Table 2.2 compares the test-over-prediction bond strength ratios of coated rebar in concrete by various researchers. Both the means and COV values of various bond models using individual data sets and the overall database are presented in Table 2.2. The mean test-over-prediction bond strength ratios are also plotted in Figure 2.11 for each data set used in analysis.

The relative performances of various models for coated rebar in concrete are similar to those for uncoated rebar in concrete. The proposed model gives the most accurate and overall conservative predictions with the smallest COV values. The prediction accuracy by Wang (2009) fluctuates among various data sets used possibly because it overemphasizes the effect of rib geometries rather than the interface bond behavior. Furthermore, Wang (2009) used a fictitious bearing angle and neglected the variation of effective bearing angle along the length of rebar.

Table 2.2. Test-over-Prediction Ratios for Bond Strength of Coated Rebar

Data Set	No. of Tests	Bond Ratio	Orangun et al. (1977)	Zuo and Darwin (2000)	Wang (2009)	Wang and Liu (2003)	This Study
Choi et al. † (1991)	29	Mean	1.972	1.154	1.182	0.752	1.008
		COV	0.356	0.374	0.233	0.124	0.064
Idun and Darwin † (1999)	14	Mean	1.342	1.094	1.112	0.728	1.082
		COV	0.280	0.071	0.186	0.084	0.044
Miller et al. † (2003)	35	Mean	1.802	1.095	0.903	0.821	1.040
		COV	0.180	0.103	0.152	0.054	0.090
De Anda et al. † (2004)	61	Mean	1.597	0.803	0.905	0.782	1.022
		COV	0.157	0.175	0.191	0.089	0.095
Wu et al.* (2012)	12	Mean	1.379	1.143	1.053	0.733	0.997
		COV	0.462	0.324	0.377	0.156	0.067
All	151	Mean	1.618	1.058	1.031	0.763	1.030
		COV	0.287	0.209	0.228	0.101	0.071

† Rebar with fusion bonded epoxy coating; * Rebar with enamel coating.

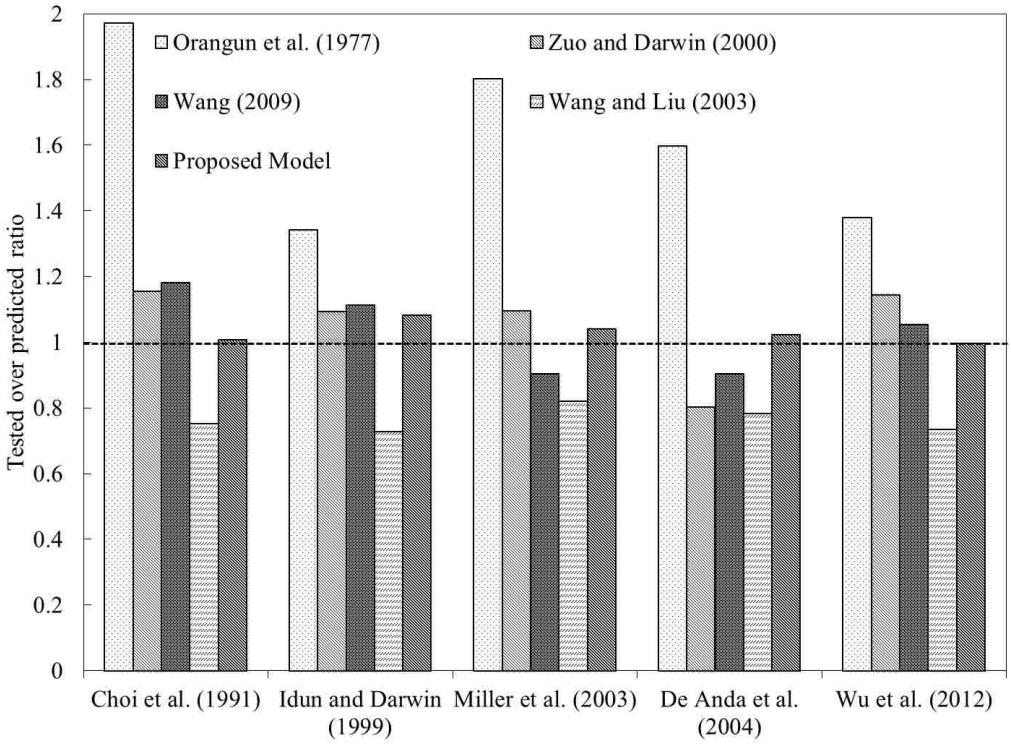

Figure 2.11. Test-over-Prediction Bond Strength Ratios for Coated Rebar

Figure 2.12 shows all bond data sets with uncoated and coated rebar in concrete and further compares the predicted bond strength by the proposed model with the tested bond strength to understand how the proposed model performs at various levels of bond strengths and for various coating conditions. It also includes two straight lines for ±10% variation around the mean line at various bond strengths. It can be clearly observed from Figure 2.12 that, except few, all the test data points fall between the ±10% lines, which is consistent with a COV of approximately 7% for uncoated or coated rebar as seen in Tables 2.1 and 2.2. In fact, by counting the number of test data points, 90% falls within the two straight lines. These consistent predictions demonstrate the applicability of the proposed model in all cases with bond strengths ranging from 4 to 21 MPa.

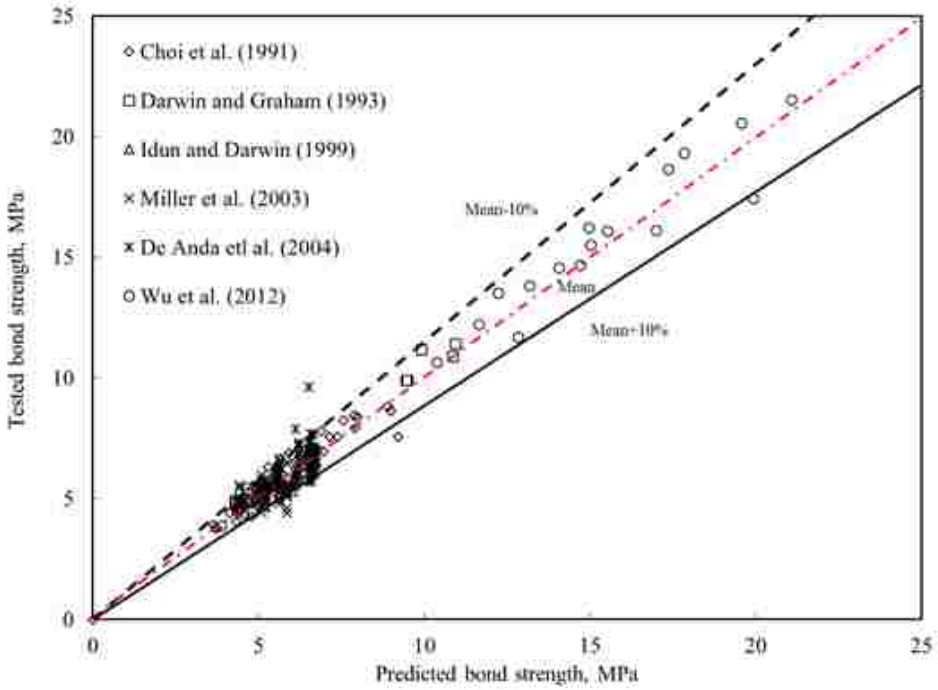

Figure 2.12. Test versus Predicted Bond Strength using the Proposed Model

2.5. NUMERICAL RESULTS AND DISCUSSION

The validated model by a large set of test data is applied to conduct parametric studies and understand the interrelation between the bond strength and various key geometric and material parameters. The results are presented in the form of charts.

2.5.1 Effects of Interface Bonding and Concrete Confinement. Forensic studies of pull-out specimens indicated that concrete crushing zones were rarely evidenced on epoxy-coated rebar (Idun and Darwin, 1999), often observed at the rib front face of uncoated rebar (Cairns and Jones, 1995), and clearly seen at the rib front face of enamel-coated rebar (Wu et al. 2012). The increasing evidence for concrete crushing zones from epoxy-coated to enamel-coated rebar indicated an increasingly significant local bond behavior. The increased crushing zone in size was directly related to a smaller effective bearing angle (Choi and Lee 2002). As a result, shear strength (interface and concrete) increases and splitting strength decreases. The effective bearing angle is evaluated from both shear strength and confinement strength. Therefore, the proposed model is a viable means of understanding failure pattern transition and the balance between shear and splitting strengths in bond behavior.

Figures 2.13 and 2.14 present the bond over concrete strength ratio as a function of bounded shear strength and concrete confinement. It indicates that the confinement ratio is more significant than the interface shear strength in determining the bond strength of rebar in concrete. As the concrete confinement increases, rebar with low interface strength can still reach the maximum shear strength along the key line. At low confinement, however, the enhancement in shear strength is limited.

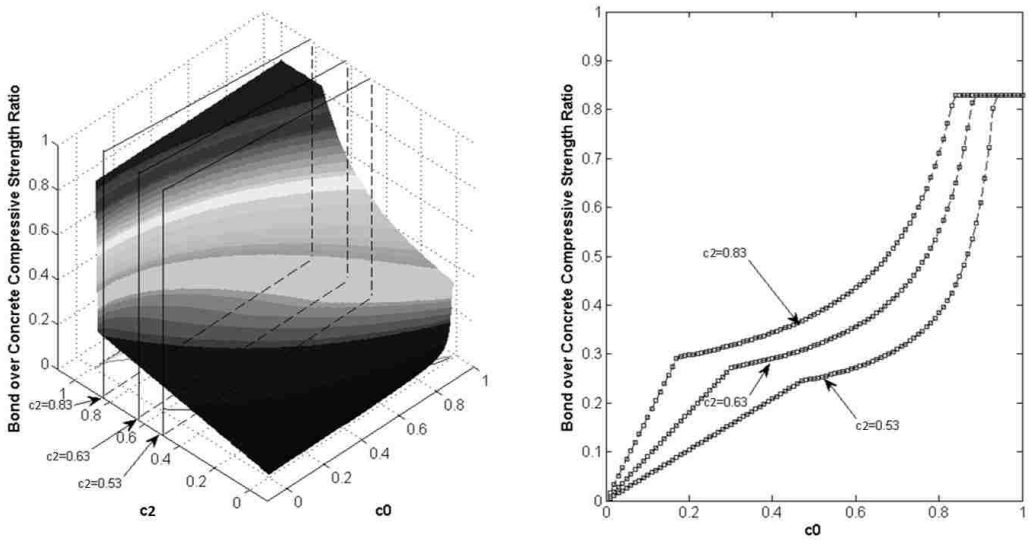

Figure 2.13. Bond-over-Concrete Strength with Various Interface Conditions

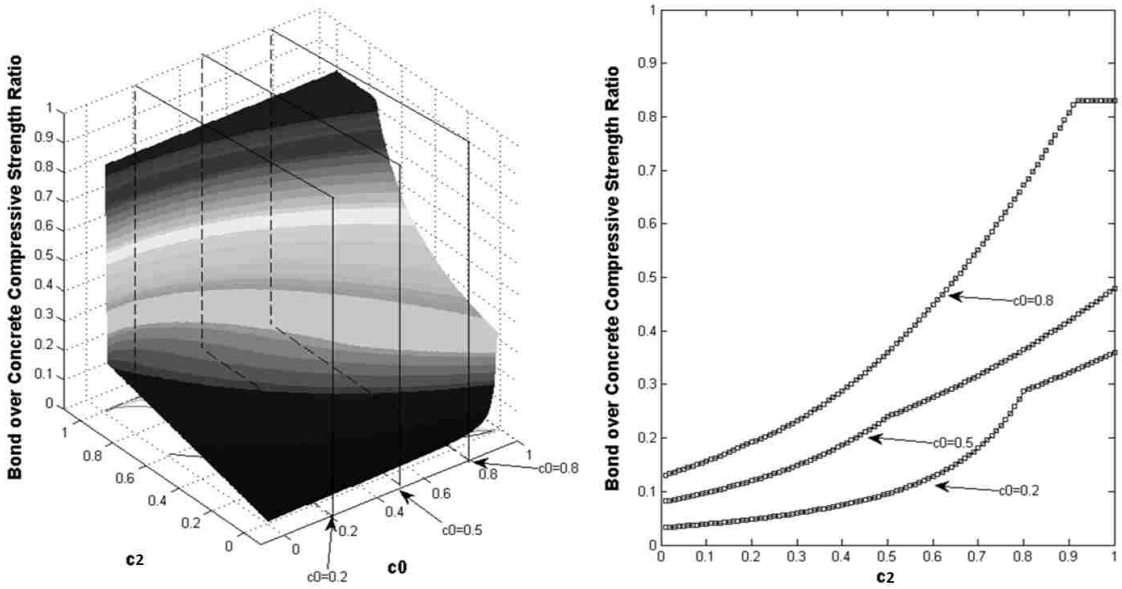

Figure 2.14. Bond-over-Concrete Strength with Various Confinement Ratios

Figure 2.15 presents the bond over compressive strength ratios for different shear strength factors. At low confinement, the enhanced interface bond strength increases the ultimate bond strength significantly. As the confinement increases, this effect diminishes gradually. The effective bearing angle reduces with the increase in confinement. When the interface bond strength is very low, failure occurs on the interface and the bearing angle is equal to the rib face angle (45°). This fact indicates that if the interface is weak, unless the confinement reaches the concrete shear state, bond strength does not increase significantly. This observation is confirmed in Figure 2.16.

With sufficient confinement, bond strength is achieved at shear failure instead of splitting. In the extreme case when the confining stress reaches the compressive strength of concrete, a zero effective bearing angle appears, indicating a concrete shear-off failure. For concrete compressive strength of 35 MPa (5,000 psi), a concrete cover to bar diameter ratio of 5 to 7 will most likely provide a pullout or "plow through" failure.

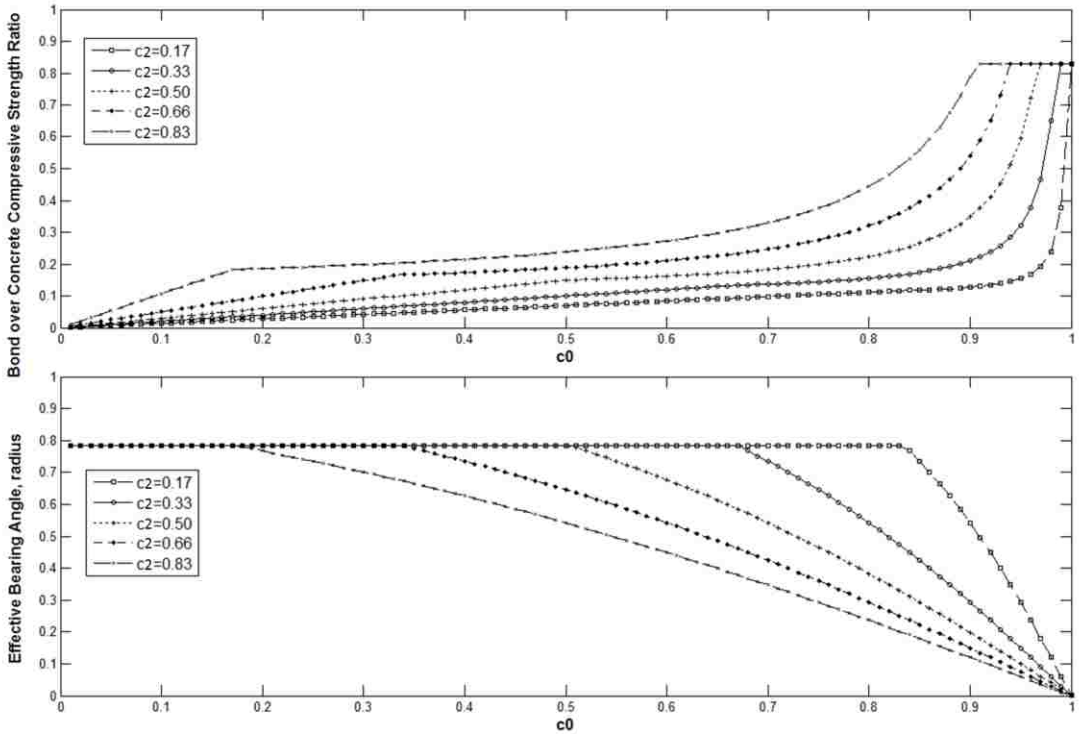

Figure 2.15. Bond Strength and Effective Bearing Angle for Varying Interfaces

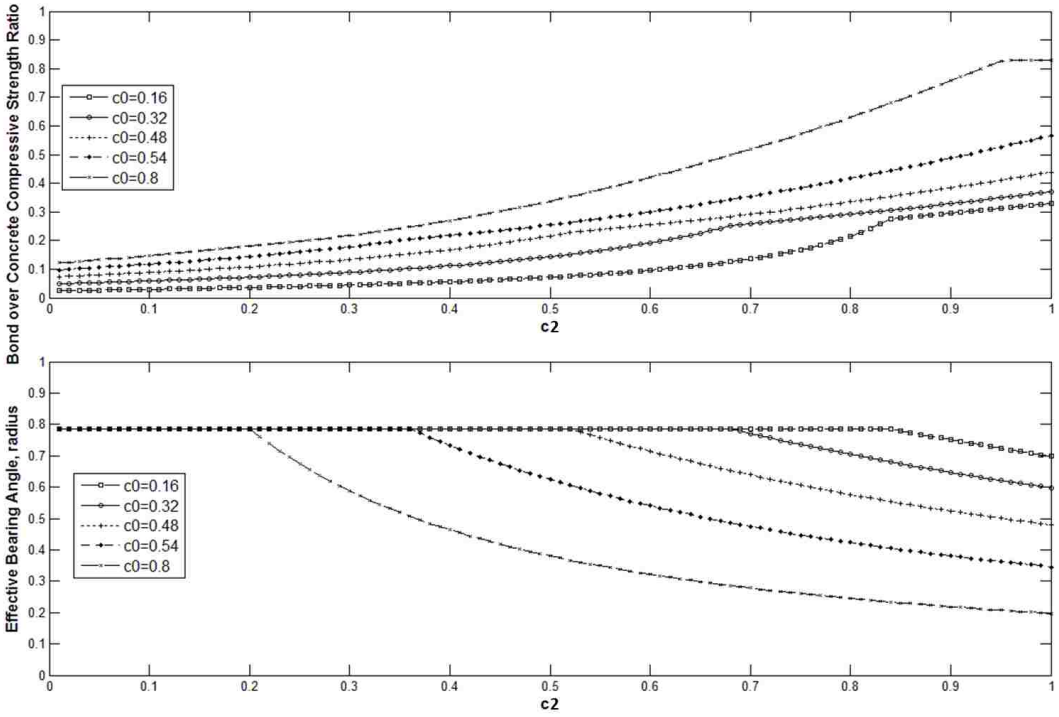

Figure 2.16. Bond Strength and Effective Bearing Angle for Varying Confinement

The maximum bond strength can be achieved when the interface strength and the concrete shear strength are equal. However, since the effective bearing angle is bounded by the rib face angle, it is more efficient to increase the bond strength by varying the rib geometry.

2.5.2 Effect of Deformation Pattern. A representative rib spacing-to-height ratio range of 8 to 12 is considered. By keeping a rib face angle of 45°, bond strength ratios with various rib spacing-to-height ratios are plotted in Figures 2.17 and 2.18. Based on these results, it is clearly seen that a high rib spacing-to-height ratio gives low bond strengths. However, this variation is more sensitive to the confinement ratio than shear strength ratio by comparing Figure 2.17 with Figure 2.18.

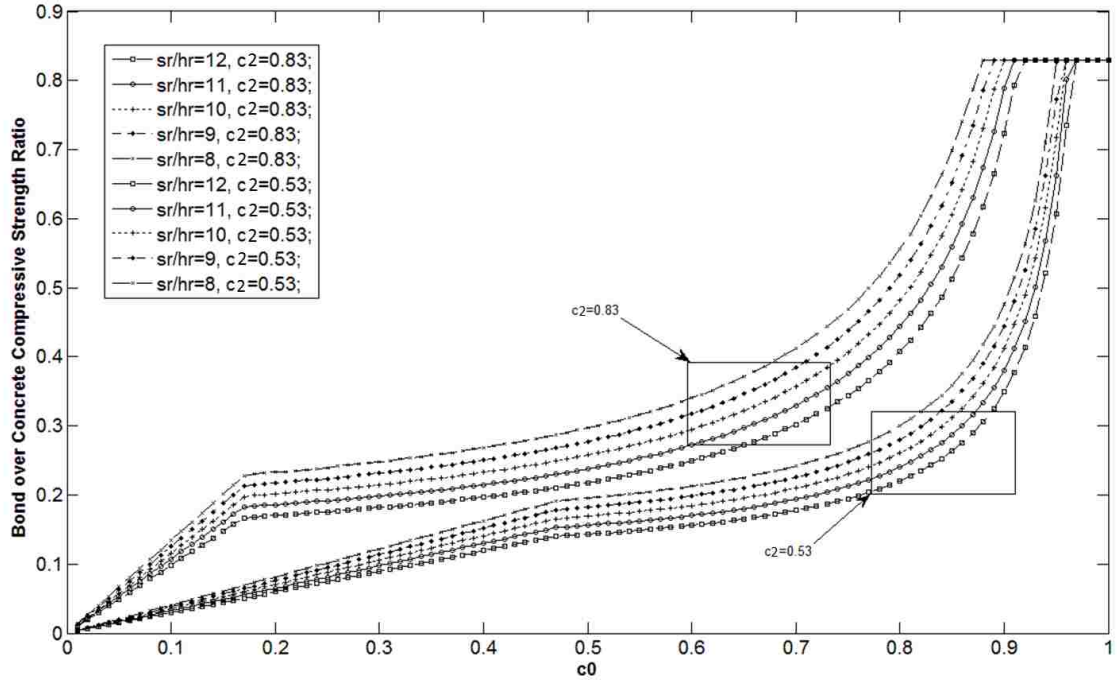

Figure 2.17. Bond Strength as a Function of Confinement with Various Rib Spacing-to-Height Ratios

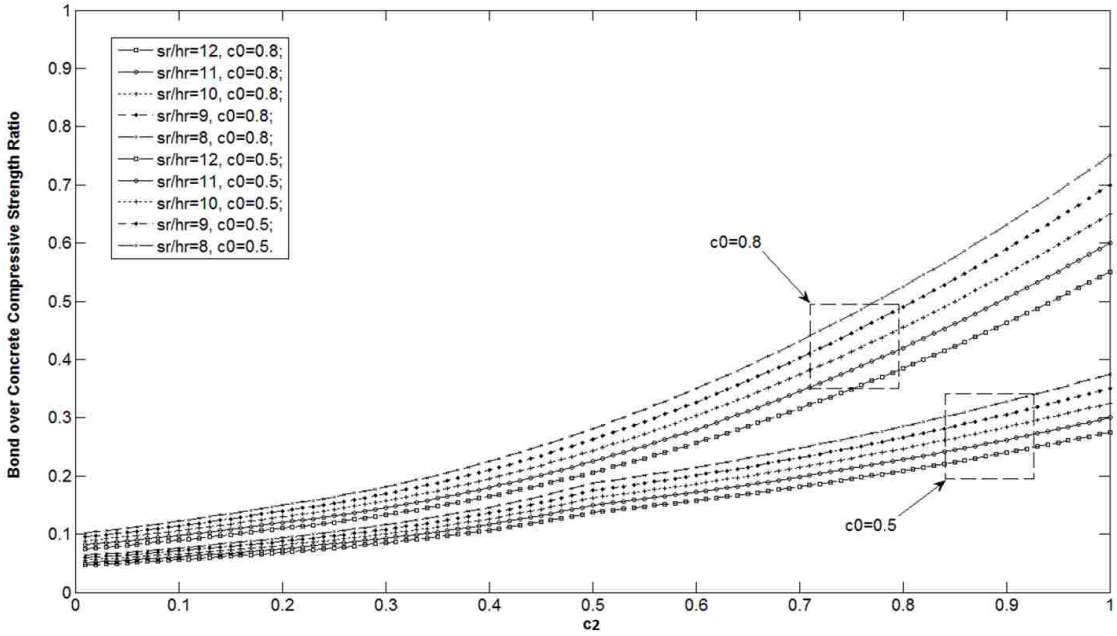

Figure 2.18. Bond Strength as a Function of Interface Condition with Various Rib Spacing-to-Height Ratios

2.6. SUMMARY

A unified bond theory of deformed rebar in concrete has been developed to understand local bond behavior. Its deduced bond strength equations for various practical scenarios have been validated with experimental data sets available to this study. Based on extensive analysis, comparison, and validation, several conclusions can be drawn:

(1) The proposed unified bond theory combines the indentation analogy for near-rebar stress analysis and the hydraulic pressure analogy for concrete confinement analysis. It covers various failure mode transitions by varying rebar-concrete interface bond strengths and unifies two traditionally distinct bond models based on the shear stress analysis and the hydraulic pressure analogy.

(2) At low rib spacing-to-height ratios, the potential failure modes near rebar ribs are "plow through" with concrete shear-off along the key line between ribs. At medium and high rib spacing-to-height ratios, the likely failure modes involve concrete crushing and both interface and concrete shear-off, determining the effective bearing angle of rebar in concrete. As the rib spacing-to-height ratio increases, the role that the confinement provided by concrete cover plays in the occurrence of the failure modes becomes more critical.

(3) The critical concrete cover to ensure a concrete shear-off failure, the critical rib face angle to determine concrete shear-off and crushing, and the critical rib spacing-to-height ratio to control different failure modes can all be explained by the unified theory and match with experimental findings from various researchers.

(4) The predicted average bond strengths are in good agreement with test results with less than 6% relative error. The proposed bond equations are more accurate than at least two theoretical and two empirical approaches available in the literature. They are demonstrated to be robust in all application scenarios with various coatings and confinement conditions.

Future studies will be directed to taken into account the effect of transverse reinforcement on local bond mechanics and behaviors. The transverse cracking induced by slipping of the wedge formed from concrete crushing can be analyzed to establish a local bond-slip law.

3. LOCAL BOND BEHAVIOR AND THEORY VALIDATION

3.1. INTRODUCTION

The unified local bond model described in Chapter 2 can take full consideration of interfacial properties in bond strength equation. It has been validated with specimens with uncoated and fusion-bonded epoxy coated rebar. Based on the collected test data from the literature, epoxy coating has been repeatedly demonstrated to reduce the bond strength between deformed rebar and concrete mainly due to reduced interfacial adhesion and friction. In this chapter, the local bond behavior with enamel-coated rebar is investigated and the pull-out test data collected is used to further validate the unified local bond theory since enamel coating can increase the rebar-concrete bond strength.

3.1.1 Enamel Coating. Recent studies (Day et al. 2006, Morefield et al. 2009) have shown that the chemically reactive vitreous enamel coating with calcium silicate additives is not only a viable corrosion barrier to steel rebar, but also a potential binding agent between the steel rebar and concrete for enhanced bond strength. Calcium silicate (CS) particles that are often used as a major component of Portland cement have been successfully mixed with enamel to demonstrate the improved bond strength between a smooth steel pin and mortar through pin-pull tests (Yan et al. 2012). Comparing to pure enamel that is commercially available, a 50/50 enamel mixture of 50% enamel and 50% CS particles by weight was found to approximately double the bond strength due to the chemical reaction between the CS particles in the enamel coating and the hydrating cement in the mortar. In addition, the roughened enamel coating surface increased the bond strength between the smooth pins and mortar by more than twice. As a result of the significant increases in bond strength, the use of a vitreous enamel coating changes the failure mode of pin-pull specimens from pin pullout to mortar splitting.

However, the bond strength between deformed steel bars and concrete in reinforced concrete (RC) structures is often dominated by the bearing force of ribs against concrete (Wright and MacGregor 2009) in addition to frictional and chemical adhesion forces. Even so, for a given type of deformed bar (same ribs), smooth coatings such as fused epoxy coatings have been shown to significantly reduce the chemical

adhesion and frictional components of epoxy coated rebar, resulting in a smaller rebar-concrete bond strength (Idun and Darwin 1999). Therefore, although the previous study by Yan et al. (2012) has already demonstrated that the use of an enamel coating can increase the surface roughness of smooth pins and the chemical adhesion between the coated pins and mortar, the relative merits of increased roughness and chemical adhesion in the presence of ribs bearing against concrete in RC structures are yet to be understood for practical applications.

3.1.2 Experimental Program. To address the aforementioned issues, a series of studies were recently conducted to characterize the bond strengths of enamel-coated reinforcement in various applications. This study was focused on the testing and analysis of concrete cylinders with relatively short embedment lengths (less than five times of the rebar diameter) of enamel coated rebar (Idun and Darwin 1999). Specifically, the failure mechanism of various enamel coated rebar in concrete was first examined. The effects of bar size/rib pattern, concrete cover, concrete strength, coating condition, and confinement condition on the rebar-concrete bond strength were then investigated.

The experimental program described in this chapter contained a total of 96 pullout specimens in 24 series of 4 specimens each, as designated in Tables 3.1 to 3.4. For each series, two specimens were reinforced with uncoated black rebar and the other two with enamel coated rebar.

3.2. MATERIALS

3.2.1 Rebar. The uncoated bars used in this study met the requirements of ASTM A615 guidelines. For coated rebar, the single layer of 50/50 enamel coating was applied by first dipping sand-blasted black rebar into the 50/50 enamel slurry (glass frit, clay, electrolytes, and Portland cement). The dipped bars were then heated for 2 minutes at 150 °C (302 °F) to drive off moisture, heated again in a gas-fired furnace to 810 °C (1490 °F) for 10 minutes, and finally cooled to room temperature (Morefield et al. 2009). This firing process melted the glass frit and bound the enamel to the steel. The average thickness of enamel coating after firing was approximately 100-200 microns (4-8 mils).

To understand whether the heat treatment process had any thermal effect on the mechanical properties of enamel coated reinforcing bars, tensile tests of both enamel

coated and black deformed bars [Grade 410 (60 in U.S.) No. 19 (#6 in U.S.) and No. 25 (#8)] were conducted according to ASTM A370 guidelines (ASTM 2010). Their difference was found to be insignificant as shown in Figure 3.1. The average yield strength of the uncoated and coated bars was 491 MPa (71.3 ksi) for No. 19 (#6) bars and 506 MPa (73.3 ksi) for No. 25 (#8) bars. The geometries of the deformations of each type of rebar are listed in Table 3.5. For clarity, all parameters are defined and illustrated in Figure 3.2.

The friction of coefficient between enamel coating and concrete was tested following the guideline of ASTM G115-10 (2010). An enamel-coated thin steel plate (3.15 mm or 1/8 in. in thickness) was placed on top of the freshly cast concrete whose properties can be found in Section 3.2.2. A 98 N (22 lbf) weight was placed on top of the plate to which a spring loaded force gage was connected and pulled by a motor at a constant rate of 1 mm/sec. The obtained coefficients of friction are 0.545, 0.582, 0.483, 0.505, and 0.534 from five tests. An average value of 0.53 was then used to represent the coefficient of friction between enamel-coated rebar and normal strength concrete.

3.2.2 Concrete. Type I Portland-cement, 19-mm (¾-in.) coarse limestone aggregates, and natural sands were used in this study. Two mix designs were used at a water-cement ratio of 0.42 and 0.38 with no admixtures, respectively. Their 28-day compressive strengths determined with standard concrete cylinder tests were 36 and 45 MPa (5.2 and 6.5 ksi) with corresponding splitting tensile strengths of 3.7 and 4.2 MPa (540 and 605 psi). Both compressive and tensile strengths are listed in Tables 3.1 to 3.4.

3.2.3 Steel Jackets. Grade 345 (50 in U.S. Customary unit) structural sheet steel used for concrete cylinder jacketing met the requirements of ASTM A572. The steel had a Young's modulus of 207 GPa (30,000 ksi) and Poisson's ratio of 0.28.

Table 3.1. Confined Specimens with No. 19 (#6) Rebar and Test Results

Series	Specimens	d_b in.	c/d_b	f'_c ksi	f_t psi	f_b psi	Avg. f_b psi	CF	n
1	C6B1_0H1	0.75	1.0	6.5	605	946	976	1.32	1
	C6B1_0H2	0.75	1.0	6.5	605	1006			1
	C6C1_0H1	0.75	1.0	6.5	605	1437	1293		1
	C6C1_0H2	0.75	1.0	6.5	605	1148			1
2	C6B2_5H1	0.75	2.5	6.5	605	2418	2329	1.08	2
	C6B2_5H2	0.75	2.5	6.5	605	2240			2
	C6C2_5H1	0.75	2.5	6.5	605	2540	2515		2
	C6C2_5H2	0.75	2.5	6.5	605	2491			2
3	C6B3_5H1	0.75	3.5	6.5	605	3247	3148	1.13	3
	C6B3_5H2	0.75	3.5	6.5	605	3049			3
	C6C3_5H1	0.75	3.5	6.5	605	3500	3557		3
	C6C3_5H2	0.75	3.5	6.5	605	3614			3
4	C6B1_0L1	0.75	1.0	5.2	540	817	893	1.32	1
	C6B1_0L2	0.75	1.0	5.2	540	969			1
	C6C1_0L1	0.75	1.0	5.2	540	1329	1176		1
	C6C1_0L2	0.75	1.0	5.2	540	1023			2
5	C6B2_5L1	0.75	2.5	5.2	540	1929	1831	1.16	2
	C6B2_5L2	0.75	2.5	5.2	540	1733			2
	C6C2_5L1	0.75	2.5	5.2	540	2138	2129		2
	C6C2_5L2	0.75	2.5	5.2	540	2119			2
6	C6B3_5L1	0.75	3.5	5.2	540	3289	3308	1.01	3
	C6B3_5L2	0.75	3.5	5.2	540	3328			3
	C6C3_5L1	0.75	3.5	5.2	540	3322	3340		3
	C6C3_5L2	0.75	3.5	5.2	540	3358			3

Note: d_b=rebar diameter; c=concrete cover; f_t=concrete splitting tensile strength; f_b= bond strength; CF=coating factor; n=number of cracks.

Unit Conversion: 1 in.=25.4mm, 1 ksi=6.895 MPa, 1 psi=6.895 KPa.

Designation: X*Y#_#Z@: X=C for confined concrete and X=N for not confined (unconfined) concrete; *=rebar size in No.; Y=C for coated rebar and Y=B for black rebar (uncoated); #_#=concrete cover to rebar diameter ratio in one decimal point; Z=H for 6.5 ksi concrete and Z=L for 5.2 ksi concrete; @=1 for first specimen and @=2 for second specimen.

Average: 1.17 2

Table 3.2. Confined Specimens with No. 25 (#8) Rebar and Test Results

Series	Specimens	d_b in.	c/d_b	f'_c ksi	f_t psi	f_b psi	Avg. f_b psi	CF	n
7	C8B1_0H1	1.0	1.0	6.5	605	1131	1126	1.16	1
	C8B1_0H2	1.0	1.0	6.5	605	1120			2
	C8C1_0H1	1.0	1.0	6.5	605	1312	1306		1
	C8C1_0H2	1.0	1.0	6.5	605	1299			1
8	C8B2_5H1	1.0	2.5	6.5	605	2248	2349	1.12	2
	C8B2_5H2	1.0	2.5	6.5	605	2450			2
	C8C2_5H1	1.0	2.5	6.5	605	2644	2639		2
	C8C2_5H2	1.0	2.5	6.5	605	2634			3
9	C8B3_5H1	1.0	3.5	6.5	605	2561	2661	1.10	3
	C8B3_5H2	1.0	3.5	6.5	605	2761			3
	C8C3_5H1	1.0	3.5	6.5	605	2789	2917		3
	C8C3_5H2	1.0	3.5	6.5	605	3045			3
10	C8B1_0L1	1.0	1.0	5.2	540	998	989	1.21	2
	C8B1_0L2	1.0	1.0	5.2	540	980			1
	C8C1_0L1	1.0	1.0	5.2	540	1204	1200		1
	C8C1_0L2	1.0	1.0	5.2	540	1196			1
11	C8B2_5L1	1.0	2.5	5.2	540	1620	1997	1.18	2
	C8B2_5L2	1.0	2.5	5.2	540	2374			2
	C8C2_5L1	1.0	2.5	5.2	540	2644	2362		3
	C8C2_5L2	1.0	2.5	5.2	540	2081			2
12	C8B3_5L1	1.0	3.5	5.2	540	2190	2255	1.10	3
	C8B3_5L2	1.0	3.5	5.2	540	2320			3
	C8C3_5L1	1.0	3.5	5.2	540	2512	2473		3
	C8C3_5L2	1.0	3.5	5.2	540	2435			3
Note: d_b=rebar diameter; c=concrete cover; f_t=concrete splitting tensile strength; f_b= bond strength; CF=coating factor; n=number of cracks. Unit Conversion: 1 in.=25.4mm, 1 ksi=6.895 MPa, 1 psi=6.895 KPa. Designation: X*Y#_#Z@: X=C for confined concrete and X=N for not confined (unconfined) concrete; *=rebar size in No.; Y=C for coated rebar and Y=B for black rebar (uncoated); #_#=concrete cover to rebar diameter ratio in one decimal point; Z=H for 6.5 ksi concrete and Z=L for 5.2 ksi concrete; @=1 for first specimen and @=2 for second specimen.							Average:	1.15	2

Table 3.3. Unconfined Specimens with No. 19 (#6) Rebar and Test Results

Series	Specimens	d_b in.	c/d_b	f'_c ksi	f_t psi	f_b psi	Avg. f_b psi	CF	N	L in.	α
13	N6B1_0H1	0.75	1.0	6.5	605	645	663	1.25	2	0.049	36
	N6B1_0H2	0.75	1.0	6.5	605	680			2	0.053	34
	N6C1_0H1	0.75	1.0	6.5	605	851	829		2	0.068	28
	N6C1_0H2	0.75	1.0	6.5	605	807			2	0.065	29
14	N6B2_5H1	0.75	2.5	6.5	605	1746	1773	1.11	3	0.062	30
	N6B2_5H2	0.75	2.5	6.5	605	1800			3	0.063	30
	N6C2_5H1	0.75	2.5	6.5	605	1996	1963		3	0.075	26
	N6C2_5H2	0.75	2.5	6.5	605	1930			3	0.077	25
15	N6B3_5H1	0.75	3.5	6.5	605	2700	2803	1.11	3	0.079	25
	N6B3_5H2	0.75	3.5	6.5	605	2906			3	0.082	24
	N6C3_5H1	0.75	3.5	6.5	605	3148	3124		4	0.100	20
	N6C3_5H2	0.75	3.5	6.5	605	3100			3	0.103	19
16	N6B1_0L1	0.75	1.0	5.2	540	526	564	1.24	2	0.068	28
	N6B1_0L2	0.75	1.0	5.2	540	602			2	0.071	27
	N6C1_0L1	0.75	1.0	5.2	540	715	699		2	0.079	25
	N6C1_0L2	0.75	1.0	5.2	540	684			2	0.088	22
17	N6B2_5L1	0.75	2.5	5.2	540	1396	1545	1.10	3	0.074	26
	N6B2_5L2	0.75	2.5	5.2	540	1693			3	0.076	25
	N6C2_5L1	0.75	2.5	5.2	540	1565	1697		3	0.085	23
	N6C2_5L2	0.75	2.5	5.2	540	1830			3	0.089	22
18	N6B3_5L1	0.75	3.5	5.2	540	2516	2706	1.10	3	0.099	20
	N6B3_5L2	0.75	3.5	5.2	540	2896			4	0.095	21
	N6C3_5L1	0.75	3.5	5.2	540	3106	2983		4	0.112	18
	N6C3_5L2	0.75	3.5	5.2	540	2860			3	0.122	16
Note: d_b=rebar diameter; c=concrete cover; f_t=concrete splitting tensile strength; f_b= bond strength; CF=coating factor; n=number of cracks; L=length of crushing zone; α=crushing angle. Unit Conversion: 1 in.=25.4mm, 1 ksi=6.895 MPa, 1 psi=6.895 KPa. Designation: X*Y#_#Z@: X=C for confined concrete and X=N for not confined (unconfined) concrete; *=rebar size in No.; Y=C for coated rebar and Y=B for black rebar (uncoated); #_#=concrete cover to rebar diameter ratio in one decimal point; Z=H for 6.5 ksi concrete and Z=L for 5.2 ksi concrete; @=1 for first specimen and @=2 for second specimen.							Average:	1.15	3	0.081	25

Table 3.4. Unconfined Specimens with No. 25 (#8) Rebar and Test Results

Series	Specimens	d_b in.	c/d_b	f'_c ksi	f_t psi	f_b psi	Avg. f_b psi	CF	N	L in.	α
19	N8B1_0H1	1.0	1.0	6.5	605	740	725	1.13	2	0.058	32
	N8B1_0H2	1.0	1.0	6.5	605	710			2	0.059	31
	N8C1_0H1	1.0	1.0	6.5	605	785	816		2	0.072	27
	N8C1_0H2	1.0	1.0	6.5	605	847			2	0.078	25
20	N8B2_5H1	1.0	2.5	6.5	605	2240	2130	1.09	3	0.070	27
	N8B2_5H2	1.0	2.5	6.5	605	2020			4	0.069	28
	N8C2_5H1	1.0	2.5	6.5	605	2320	2332		3	0.082	24
	N8C2_5H2	1.0	2.5	6.5	605	2344			3	0.088	22
21	N8B3_5H1	1.0	3.5	6.5	605	2205	2354	1.07	3	0.098	20
	N8B3_5H2	1.0	3.5	6.5	605	2504			3	0.100	20
	N8C3_5H1	1.0	3.5	6.5	605	2300	2529		3	0.118	17
	N8C3_5H2	1.0	3.5	6.5	605	2757			3	0.125	16
22	N8B1_0L1	1.0	1.0	5.2	540	719	714	1.14	2	0.083	23
	N8B1_0L2	1.0	1.0	5.2	540	709			2	0.085	23
	N8C1_0L1	1.0	1.0	5.2	540	749	816		2	0.097	20
	N8C1_0L2	1.0	1.0	5.2	540	883			2	0.092	21
23	N8B2_5L1	1.0	2.5	5.2	540	1990	2005	1.12	3	0.105	19
	N8B2_5L2	1.0	2.5	5.2	540	2019			3	0.101	20
	N8C2_5L1	1.0	2.5	5.2	540	2330	2249		3	0.112	18
	N8C2_5L2	1.0	2.5	5.2	540	2168			3	0.125	16
24	N8B3_5L1	1.0	3.5	5.2	540	2083	2112	1.11	4	0.120	17
	N8B3_5L2	1.0	3.5	5.2	540	2141			4	0.127	16
	N8C3_5L1	1.0	3.5	5.2	540	2471	2336		3	0.150	14
	N8C3_5L2	1.0	3.5	5.2	540	2200			3	0.158	13

Note: d_b=rebar diameter; c=concrete cover; f_t=concrete splitting tensile strength; f_b= bond strength; CF=coating factor; n=number of cracks; L=length of crushing zone; α=crushing angle.

Unit Conversion: 1 in.=25.4mm, 1 ksi=6.895 MPa, 1 psi=6.895 KPa.

Designation: X*Y#_#Z@: X=C for confined concrete and X=N for not confined (unconfined) concrete; *=rebar size in No.; Y=C for coated rebar and Y=B for black rebar (uncoated); #_#=concrete cover to rebar diameter ratio in one decimal point; Z=H for 6.5 ksi concrete and Z=L for 5.2 ksi concrete; @=1 for first specimen and @=2 for second specimen.

Average:	1.11	3	0.099	21

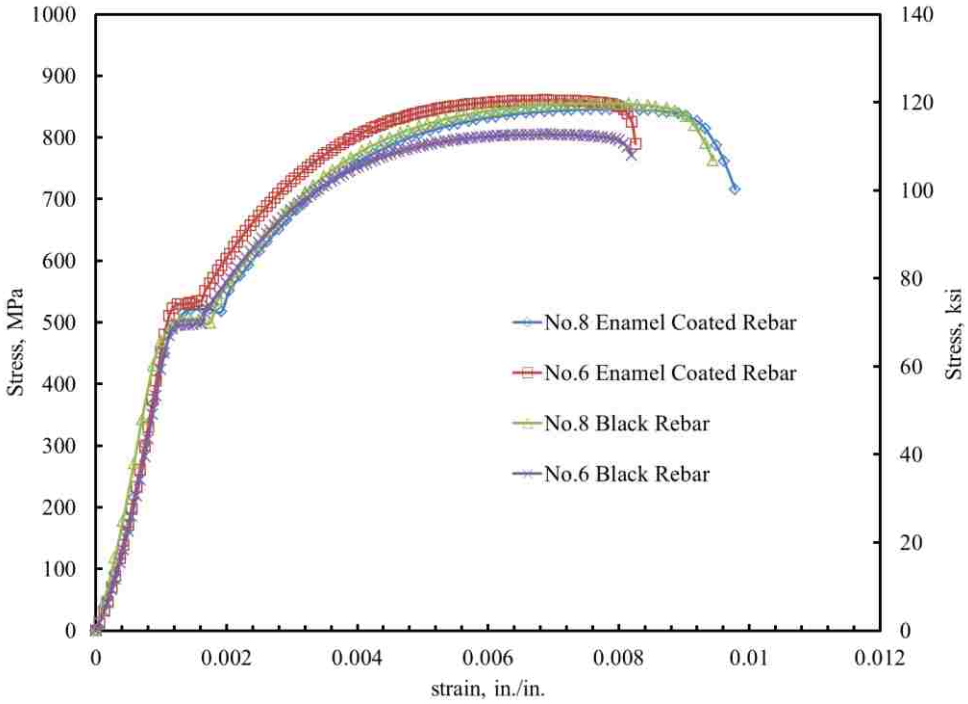

Figure 3.1. Stress-Strain Relationship for Grade 410 (60) No. 19 (#6) and No. 25 (#8) Rebar: Before and After Coating

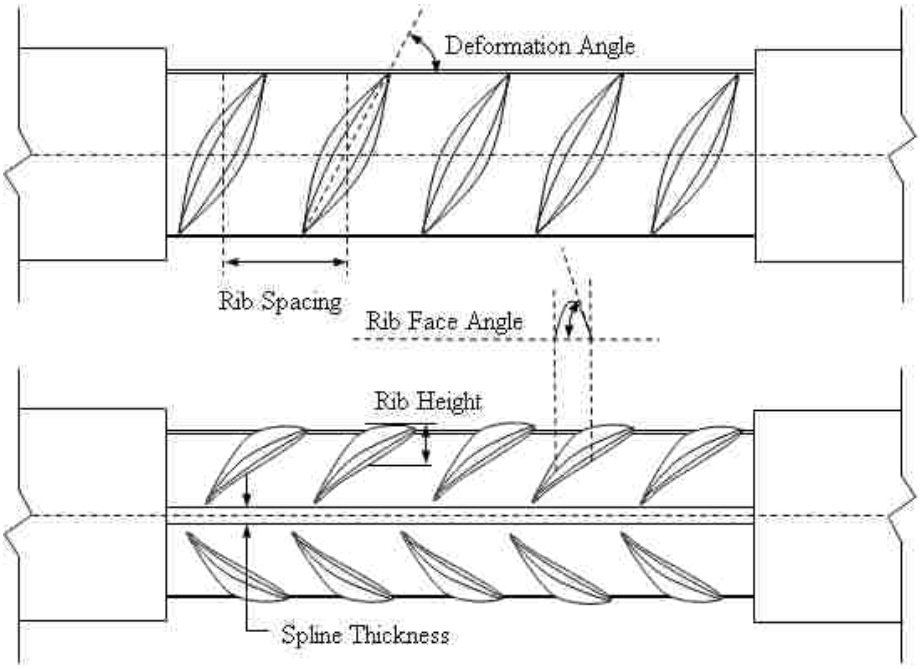

Figure 3.2. Dimensions of Rebar

Table 3.5. Geometrical Details of Rebar

Rebar Type	Rebar Diameter, in.	Deformation Angle, Degree	Rib Face Angle, degree	Rib Spacing, in.	Rib Height, in.	Spline Thickness, in.
No.19 (#6) Uncoated	0.74	70	42	0.47	0.036	0.11
No.19 (#6) Coated	0.77	70	42	0.46	0.037	0.11
No.25 (#8) Uncoated	1.01	80	44	0.60	0.058	0.18
No.25 (#8) Coated	1.00	80	44	0.59	0.061	0.18

*1 in.=25.4mm

3.3. TEST SPECIMENS

Each pullout specimen was a concrete cylinder of 165 mm (6.5 in.) in length with one deformed bar embedded along its centerline. As illustrated in Figure 3.3(a), the specimen was prepared with a short embedment length of only 63.5 mm (2.5 in.) to achieve a relatively uniform bond stress distribution. To reduce arching effects and end restraints, the specimen had a 50.8-mm-long (2-in.) and 38.1-mm-diameter (1.5 in.) bond breaker at each end, which was made of 3.2-mm-thick (0.125 in.) PVC tubing.

The deformed bar was wrapped with Styrofoam strips, and then inserted into the PVC tubes to ensure that the bar was centered inside the concrete cylinder. Silicon was applied at both ends of each bond breaker to avoid leaking during the concrete placement and consolidation. The above procedures formed "ideal" bond breakers that can slide freely without causing any noticeable anchoring effect.

No. 19 (#6) and No. 25 (#8) rebar were used to study the influence of bar parameters. Concrete cover-to-rebar diameter (c/d_b) ratios of 1.0, 2.5, and 3.5 were considered to study the influence of different degrees of confinement contributed by solid concrete. To provide additional quantifiable confinement, the steel jackets described earlier were applied to 48 out of 96 specimens. They were made in three different sizes with a wall thickness of 3.2 mm (0.125 in.) to fit various concrete cylinders. As shown in Figure 3.3(b), each jacket consisted of two semi-circular rings with a gap of 8.9 mm (0.35

in.) at each joint. Each joint was connected with three bolts that were tightened with a torque of 27 N-m (20 lb-ft.) prior to testing.

For clarity, only those specimens with additional confinement provided by steel jackets are referred to as confined specimens in this chapter. The others are designated as unconfined specimens even though solid concrete itself provided some confinement to the rebar. Each pullout specimen is identified with a string of numbers and letters as specified in Tables 3.1 to 3.4.

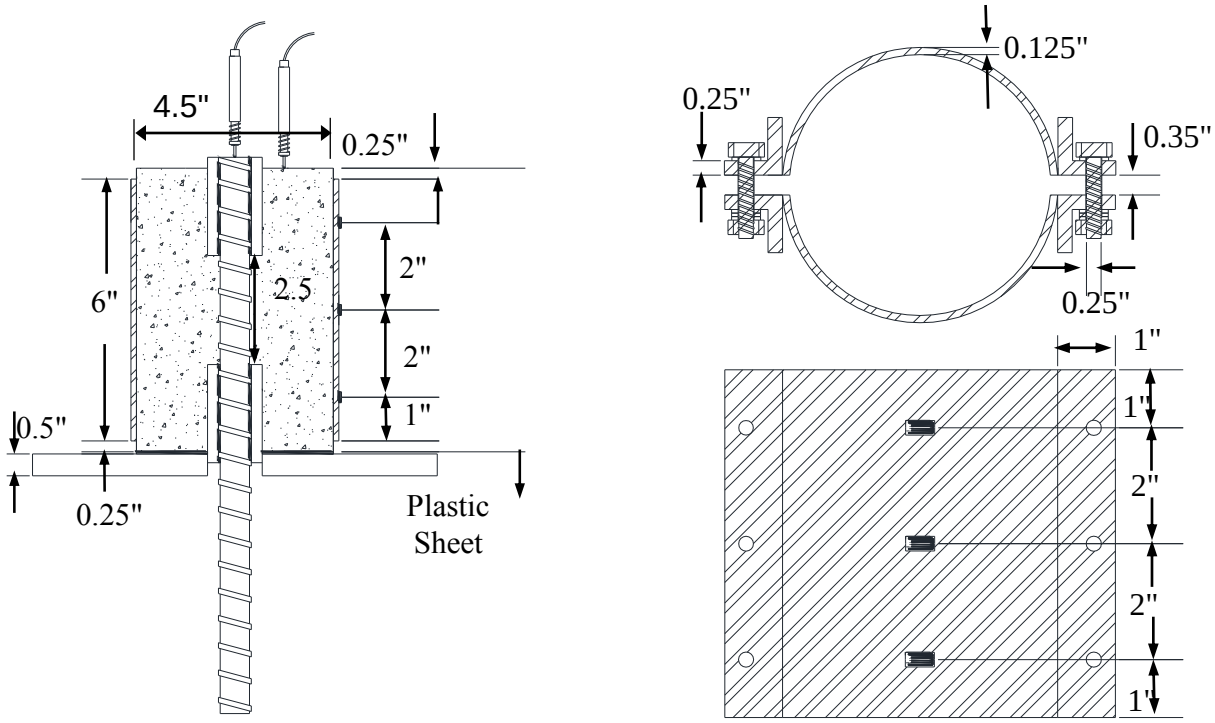

(a) Cross sectional view of confined specimen in test

(b) Details of steel jacket

Figure 3.3. Specimens Details

3.4. TEST SETUP

Each specimen was tested on a Tinius Olsen machine as shown in Figure 3.4(a) with the rebar pulled downward. A 12.7-mm-thick (0.5 in.) steel plate was used to provide an upward reaction to the bottom face of the concrete cylinder. Between the steel

plate and the cylinder was a 6.35-mm-thick (0.25 in.) Neoprene pad with a center hole used to avoid stress concentrations caused by any potentially uneven concrete surface introduced during the casting process. To minimize the restraining effect of end friction, a 1-mm-thick (0.08 in.) greased plastic sheet was inserted between the Neoprene pad and the steel plate.

Each specimen was instrumented with two Linear Variable Differential Transformers (LVDTs) at the end of the rebar and the end concrete surface of the specimen, respectively, as detailed in Figure 3.4(b). The difference in readings of the two LVDTs gave the relative slip between the bar and the concrete cylinder. This instrumentation scheme is desirable for bond slip measurements since it is not affected by any slack that may exist in the test specimen setup. For confined specimens, three strain gages were installed on the outside surface of each steel jacket at three locations as shown in Figure 3.4(b) in order to monitor the level of hoop strain generated during the tests. A load rate of 1.27 mm (0.05 in.) per minute was applied to simulate the quasi-static loading condition in displacement control.

(a) Tinius Olsen machine

(b) Instrumentation detail

Figure 3.4. Test Setup

3.5. RESULTS AND DISCUSSION

3.5.1 Average Bond Stress. The average bond stress was calculated using Eq. (3.1).

$$u_{avg} = \frac{P}{\pi d_b l_d} \tag{3.1}$$

where u_{avg} is the average bond stress, P is the applied load, l_d is the embedment length, and d_b is the diameter of rebar.

3.5.2 Unconfined Specimens.

3.5.2.1 Failure modes. All unconfined specimens failed suddenly in concrete splitting at ultimate loads. It was observed during the tests that rebar was rapidly pulled out of the concrete cylinders immediately after cracks appeared on the side surface of the cylinders. No residual bond strength was evidenced after concrete splitting. The brittle failure mode as shown in Figure 3.5(a) is similar to Mode II A as illustrated in Figure 3.6 (Carins and Abdullah 1996).

(a) Unconfined specimen (b) Confined specimen

Figure 3.5. Failures of Specimens after Test

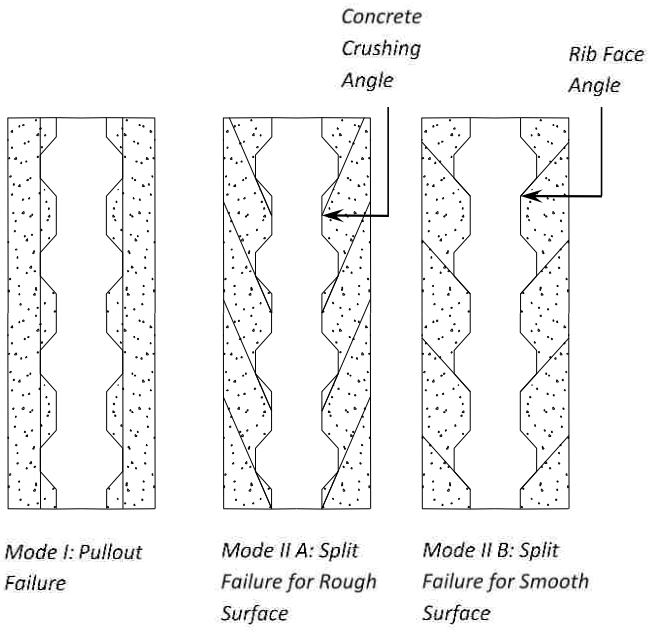

Figure 3.6. Failure Modes (Cairns and Abdullah, 1996)

Forensic studies were conducted on failed specimens. As clearly shown in Figure 3.7(a, b), local concrete crushing was observed near lugs of both coated and uncoated rebar. However, the enamel coated rebar was fully covered with cement debris from the concrete matrix as illustrated in Figure 3.7(a) while the uncoated rebar was locally covered with concrete debris in the rib-front areas only, as illustrated in Figure 3.7(b). The different pattern in concrete debris residuals that remained on the rebar surface indirectly demonstrated the enhanced chemical adhesion and roughness of enamel coated rebar due to the use of chemically active CS particles.

(a) Unconfined specimen with coated rebar

(b) Unconfined specimen with uncoated rebar

(c) Confined specimen with coated rebar

(d) Confined specimen with uncoated rebar

Figure 3.7. Close View of Failed Specimens

3.5.2.2 Coating factor. The maximum bond stress by Eq. (3.1) was referred to as the bond strength of the tested specimen. For each series of four specimens in Tables 3.1 and 3.2, the average bond strength of two specimens with uncoated rebar and the average bond strength of the other two specimens with enamel coated rebar were calculated respectively. The ratio of their average bond strengths was then defined as a coating factor, measuring the effect of enamel coating on the average bond strength. Finally, the average of all the coating factors for each rebar size was determined. This process was implemented in Tables 3.1 and 3.2. Overall, the average increase in bond strength due to enamel coating is approximately 15% with No. 19 (#6) rebar and 11% with No. 25 (#8) rebar. The reduction in coating effect is due to the fact that, as the size of the rebar increases, the bearing force that is closely related to concrete strength becomes more

significant than the chemical adhesion and frictional force that can be enhanced by the use of the enamel coating.

The coating factors for all series of specimens are presented in Figure 3.8. It can be clearly seen from Figure 3.8 that the coating factor decreases as the c/d_b ratio increases. This fact can be explained through the interrelation among the radial pressure applied on the concrete cylinder, concrete cover-to-rebar diameter ration (c/d_b), and concrete-steel friction. The bond strength controlled by concrete splitting is mainly composed of two parts: the chemical adhesion and frictional force between two adjacent rebar ribs and the longitudinal component of the bearing force at the rib front. Both forces increase with the maximum radial pressure that can be developed based on the tensile strength of the concrete in the tangential direction (hoop effect). The maximum radial pressure rapidly increases with c/d_b at the beginning but soon approaches an asymptotic value (Tephers 1973). As a result, the increase of the two forces from uncoated to coated rebar is larger at small c/d_b and significantly smaller at large c/d_b since the enamel coating increases the friction coefficient and chemical adhesion between steel and concrete, extending the concrete crushing zone along the rebar. In other words, the coating factor decreases with increasing c/d_b.

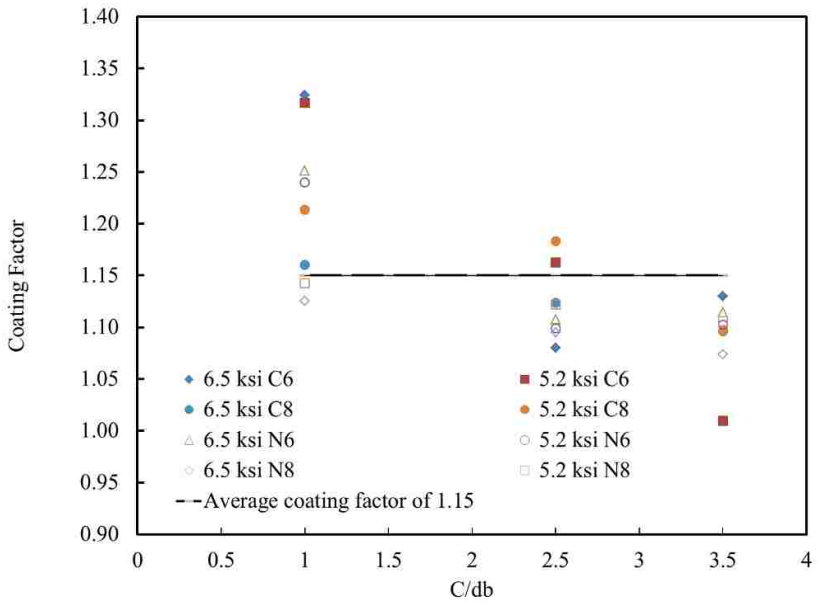

Figure 3.8. Coating Factor

3.5.2.3 Bond-slip curves. For clarity, only representative curves between bond stress and rebar slip are plotted in Figure 3.9 for selected unconfined specimens. The bond-slip curves all show a monotonically increasing behavior. The sudden drop in bond stress at the ultimate load indicated concrete cylinder splitting. Compared to the uncoated specimens, nearly all the coated specimens failed at higher ultimate slips and higher bond strengths. The initial slopes of the bond-slip curves for both coated and uncoated specimens are nearly equal in each series. Therefore, enamel coating contributed little to the stiffness of specimens.

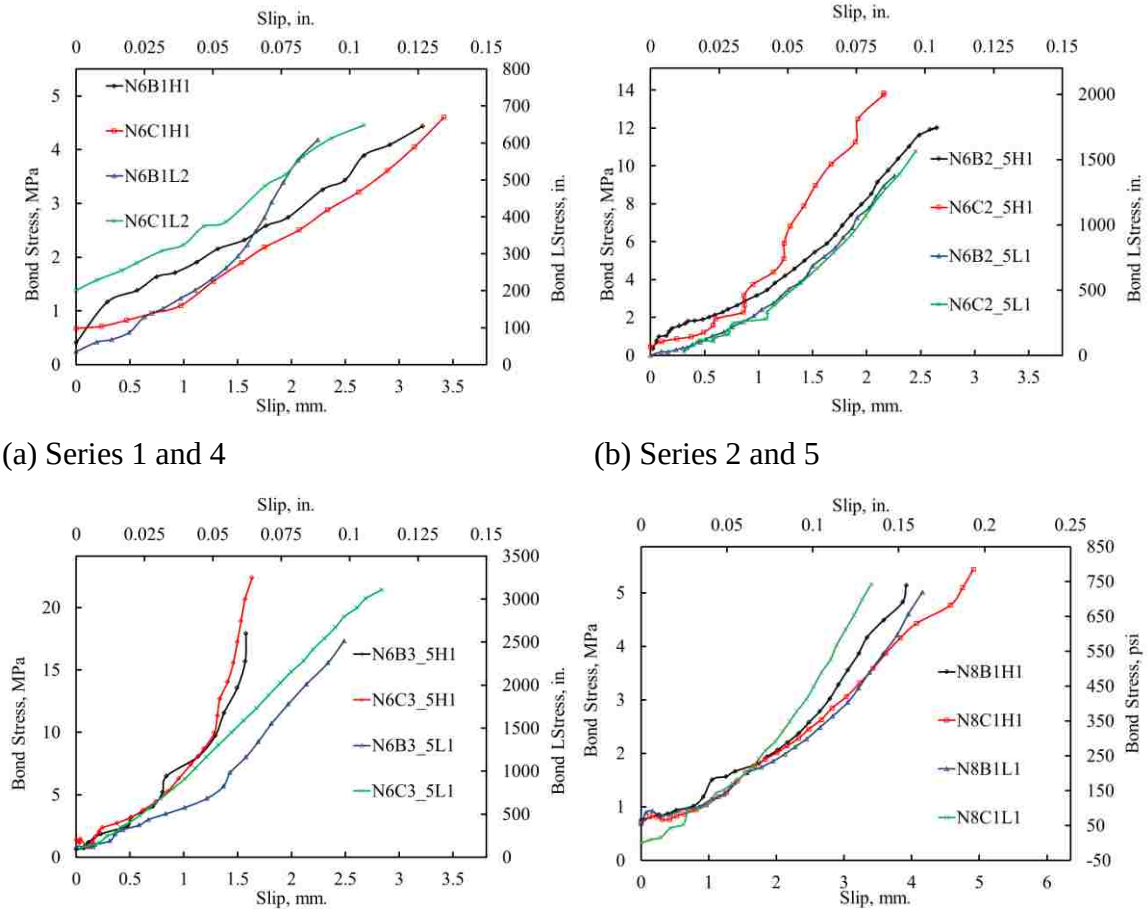

(a) Series 1 and 4

(b) Series 2 and 5

(c) Series 3 and 6

(d) Series 7 and 10

Figure 3.9. Typical Bond-Slip Curves for Unconfined Specimens

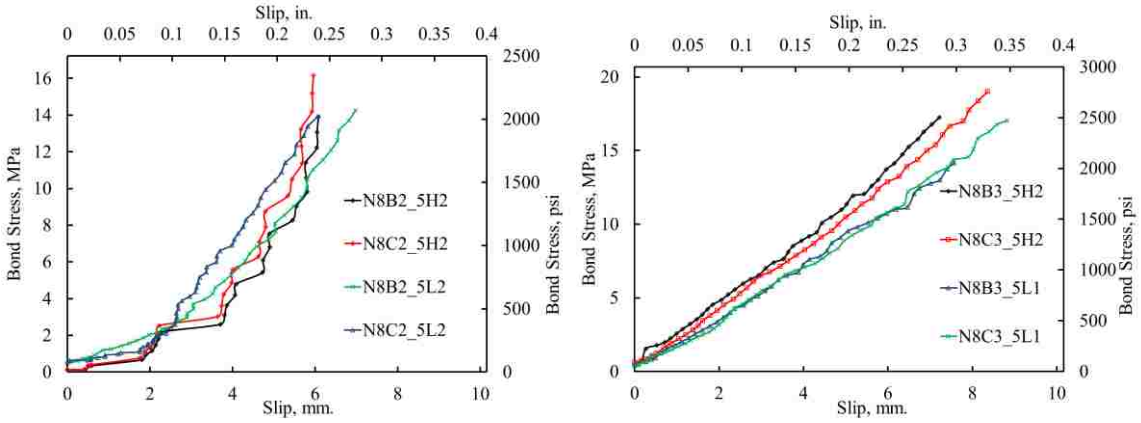

(e) Series 8 and 11 (f) Series 9 and 12

Figure 3.9. Typical Bond-Slip Curves for Unconfined Specimens (cont.)

3.5.3 Confined Specimens. All confined specimens experienced both splitting of the concrete as seen in Figure 3.5(b) and shear-off of the concrete keys in between lugs of rebar as shown in Figures 3.7(c) and (d). Such a failure mode is similar to Mode I as illustrated in Figure 3.6. The radial component of bond forces first generated the hoop stress in the concrete cylinder that was mostly resisted by the solid concrete prior to splitting, and was then balanced by the resistance force provided by the steel jacket after concrete splitting. At the ultimate failure, the concrete keys in between the lugs of rebar were sheared off.

3.5.4 Coating Factor. Similar to the unconfined specimens, the coating factors were calculated and presented in Tables 3.3 and 3.4 for each series of confined specimens with No. 19 (#6) and No. 25 (#8) reinforcing bars, respectively. The average of all coating factors for each rebar size was also determined and listed in Tables 3.3 and 3.4. Overall, the average increase in bond strength due to enamel coating was 17% for No. 19 (#6) rebar and 15% for No. 25 (#8) rebar under confinement provided by the steel jackets. Once again, the reduction in coating effect on bond strength was attributed to the increase in rib height from No. 19 (#6) to No. 25 (#8) rebar so that the bearing force instead of the chemical adhesion and frictional force became more dominant.

By comparing the confined specimens with the unconfined specimens, confinement increased the average coating effect on bond strength from 15% to 17% for

No. 19 (#6) rebar and from 11% to 15% for No. 25 (#8) rebar. Prior to concrete splitting, the additional confinement provided by the steel jackets amplified the frictional effect on bond strength associated with the increased surface roughness by enamel coating. The limited increase in bond strength due to confinement is supported by the relatively small confinement strains as will be discussed in Section 3.5.6. The results imply that, in practical applications, the use of transverse reinforcement on longitudinal main reinforcement can increase the coating effect on bond strength.

3.5.5 Bond-Slip Curves. Representative bond-slip curves for selected confined specimens are presented in Figure 3.10. In contrast to Figure 3.9 for unconfined specimens, all curves in Figure 3.10 had the first ascending stage to the peak bond stress or bond strength and then the descending stage over a significant slip. Except for a few specimens in Figure 3.10(a, b), the bond strengths of all specimens corresponded to sudden drops of the bond-slip curves due to concrete splitting. This is particularly true for specimens with large concrete cover since these cases likely involved more sudden disruptions to the concrete cylinders in the process of load transfer from solid concrete to the steel jacket upon concrete splitting. The descending stages of all bond-slip curves in Figure 3.10 represented the shear process of the concrete keys in between rebar ribs. For most specimens, the descending stages appeared as smooth decaying curves. The few exceptions showed more fluctuations of bond stress with bond slip likely due to non-uniformity of rebar and ribs as the bond slip was measured at the end of each specimen.

Figure 3.10 also indicated that, corresponding to concrete splitting, the bond slip for most specimens with coated rebar is slightly larger than that for specimens with uncoated rebar in the same series. Similarly, since the descending stages represent the shear-off of concrete keys between the rebar ribs, the post peak behavior of bond-slip is controlled by the shear strength of concrete and the geometry of the rebar ribs.

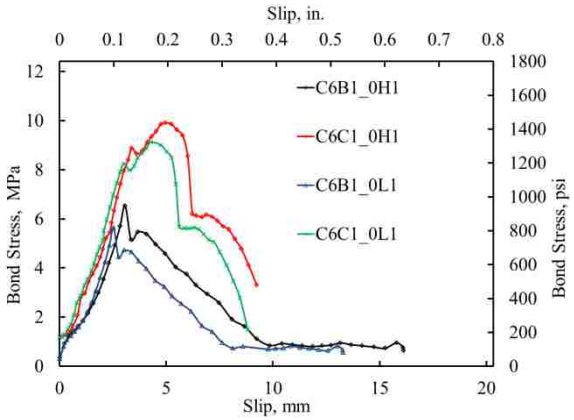

Series 13 and 16

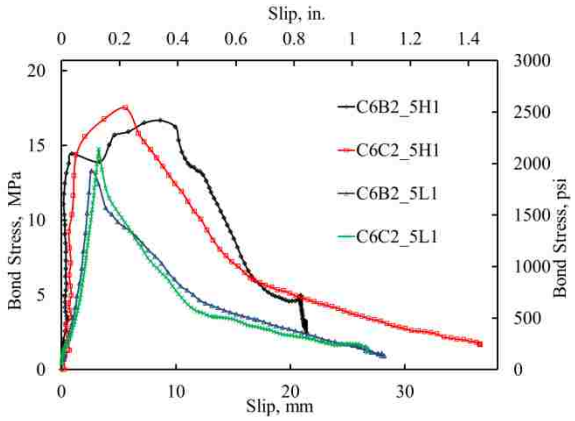

Series 14 and 17

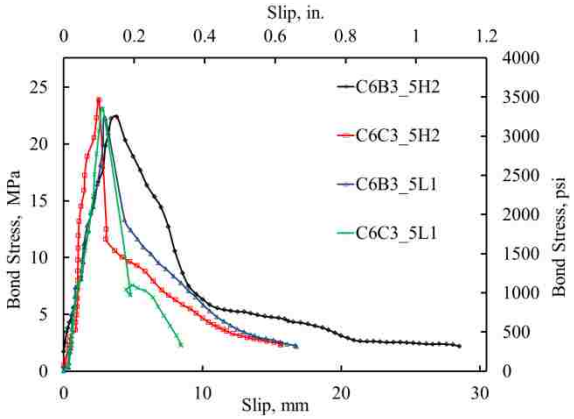

Series 15 and 18

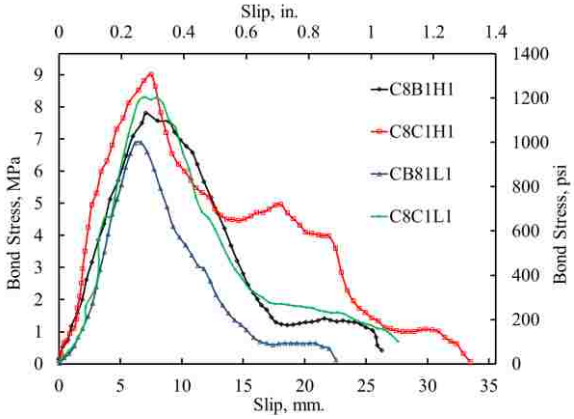

Series 19 and 22

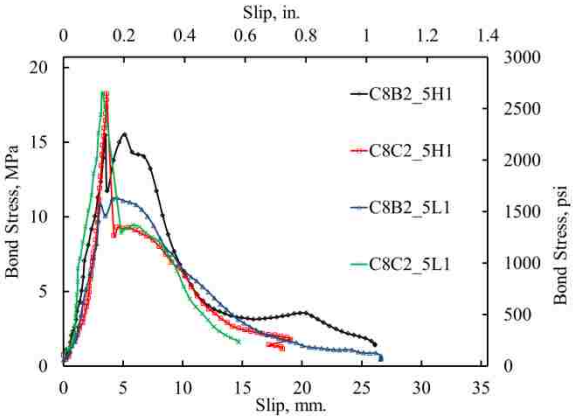

Series 20 and 23

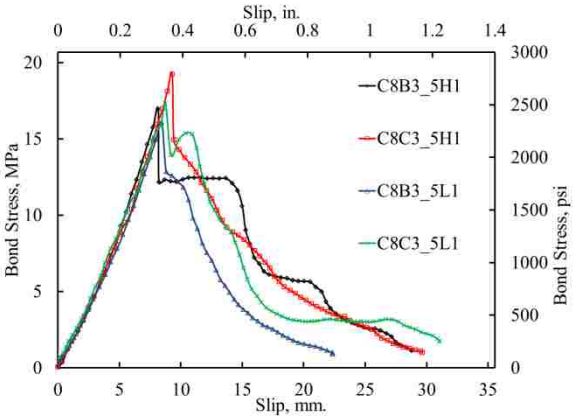

Series 21 and 24

Figure 3.10. Typical Bond-Slip Curves for Confined Specimens

3.5.6 Confinement Effect. Figure 3.11 presents the strains on steel jackets for several confined specimens. In general, the strain readings on the steel jackets were approximately 50 micro-strains prior to concrete splitting, rapidly increased immediately after concrete splitting, and then remained relatively constant until complete shear-off of the concrete keys. No significant difference was found between specimens with coated and uncoated rebar. Corresponding to a c/d_b ratio of 1.0, 2.5, and 3.5, the confinement strains were on the order of 200, 500, and 700 micro-strains for specimens with No. 19 (#6) rebar and on the order of 300, 700, and 900 micro-strains for specimens with No. 25 (#8) rebar, respectively.

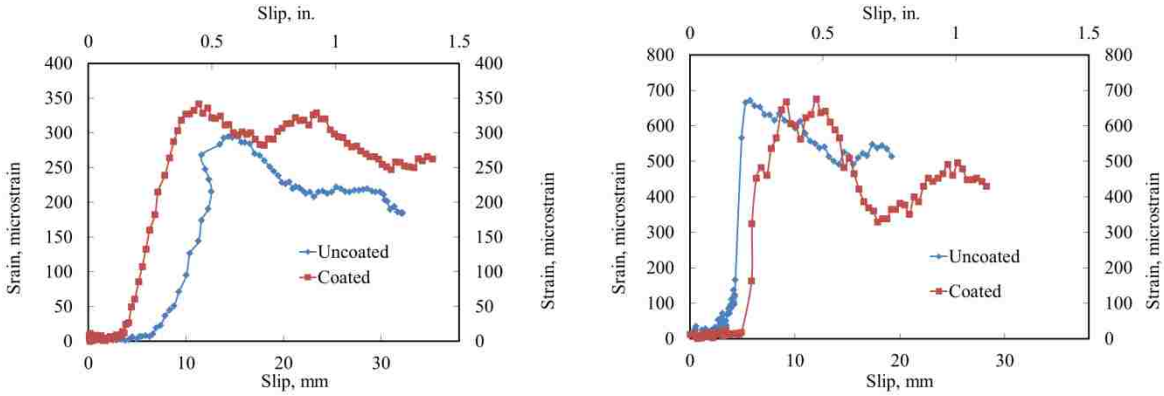

(a) Series 19 (b) Series 20

Figure 3.11. Confining Strain versus Slips

It has been experimentally demonstrated (Darwin and Graham 1993) that, under high confinement, bond strength increases with an increase in the relative rib area of the rebar. The increased bond strength is related to the enhanced frictional effect of the coatings. However, as the bursting pressure on the concrete cylinders was controlled by the splitting strength of the concrete cover, which is independent of the rebar, the increased friction in between ribs had a limited contribution to increasing the bond strength.

It should be noted that, unlike previous studies (Wang and Liu 2003), the steel jackets used in this study were not controlled by any hydraulic pressure. This passive

confinement mechanism induced limited confinement on the concrete cylinders. However, it resembles the mechanism of confining main reinforcement with stirrups in RC members. Therefore, the results obtained with steel jackets are representative of practical applications.

3.6. FURTHER DISCUSSION ON BOND BEHAVIOR

3.6.1 Stages on Bond Slip Curves. As reported by Tassios (1979), the ideal bond-slip curve of deformed bars in concrete can be divided into several stages. In this study, six stages were observed from the test results as summarized in Figure 3.12(a). In stage I, the chemical adhesion between rebar and concrete plays a major role in their bond stress, corresponding to an unnoticeable slip due to strain localization at the rebar-concrete interface layer. At the end of Stage I, the bond stress for enamel coated rebar was almost always higher than that for uncoated rebar as shown in Figures 3.9 and 3.10. This observation demonstrated the aimed enhancement of chemical adhesion by the use of enamel coating.

In stage II, transverse cracks initiate in concrete near the ribs of rebar as the concrete is significantly dilated due to the increasing slip. At the same time, radial splitting cracks initiate and develop steadily. After the bond stress reaches a certain value (Giuriani 1981), local crushing occurs and the crushing zone increases as detailed in Figure 3.12(b). For the unconfined specimens with sufficient concrete cover, the bond strength was attained when the splitting cracks penetrate through the concrete cover.

For confined specimens, the bond stress continues to increase beyond the second stage and the local concrete crushing zone increases until the concrete shear keys between lugs are completely demolished. This stage is defined as Stage III or V, depending on the level of lateral confinement. At low confinement, Stages III and V may not be distinguishable from the test data. In this case, concrete keys start to be sheared off before the splitting crack completely penetrates through the concrete cover as indicated by Figure 3.13 after the tested cylinder was separated into two pieces. Therefore, the sudden drop in bond stress due to splitting of the concrete cover (stage IV) is not observed. After all the concrete keys are sheared off, the bond stress decreases over a significant slip in Stage VI and approaches the friction-induced residual bond strength. At

high confinement, after the splitting cracks completely penetrate through the concrete cover, a sudden drop in bond stress, Stage VI, is clearly observed as illustrated in Figure 3.12(a).

3.6.2 Number of Radial Cracks. The number of radial cracks that penetrated through the concrete cover is reported in Tables 3.1 to 3.5. Overall, no significant difference was observed between the coated and uncoated rebar. For both types of rebar, concrete cover was fully penetrated. The average number of splitting cracks ranges from 1 to 3 as the concrete cover increased. This is mainly because a stiffer concrete cylinder with thicker cover makes it more difficult to pull the rebar out of the cylinder without additional cracks. Furthermore, fewer cracks were observed for confined specimens since steel jackets took a significant portion of the tensile hoop stress in the concrete, forcing rebar to shear off concrete at higher bond forces.

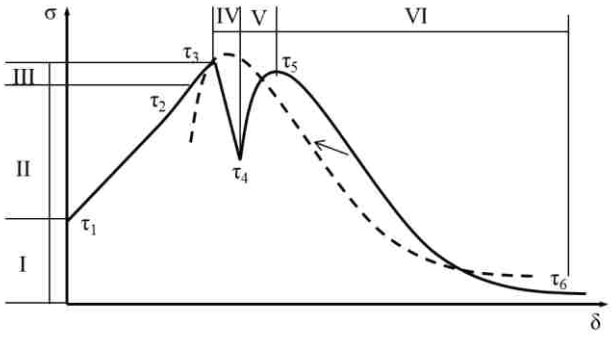

(a) Bond-slip curve-all stages

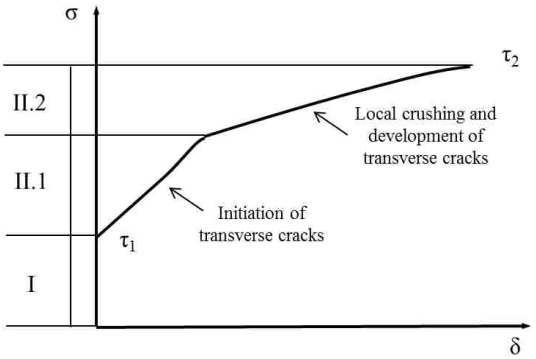

(b) Bond-slip curve-stages I and II

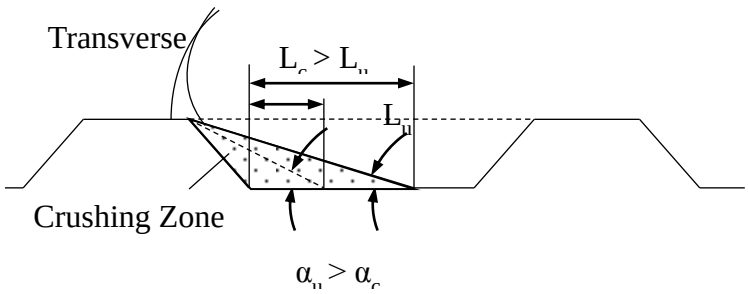

(c) Changing of failure surface due to coating effect

Figure 3.12. Analysis of Bond-Slip Behavior

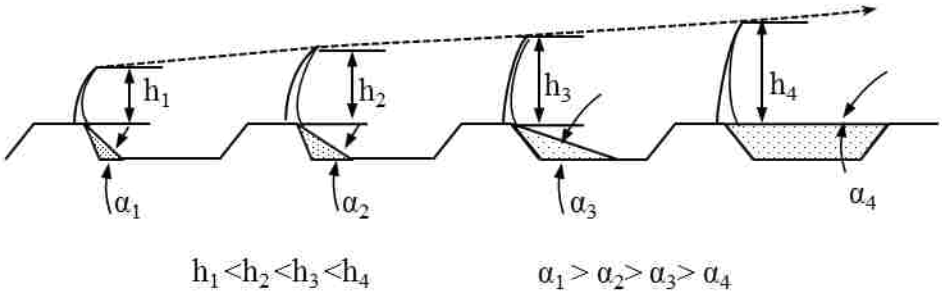

(d) Varying of failure status

Figure 3.12. Analysis of Bond-Slip Behavior (cont.)

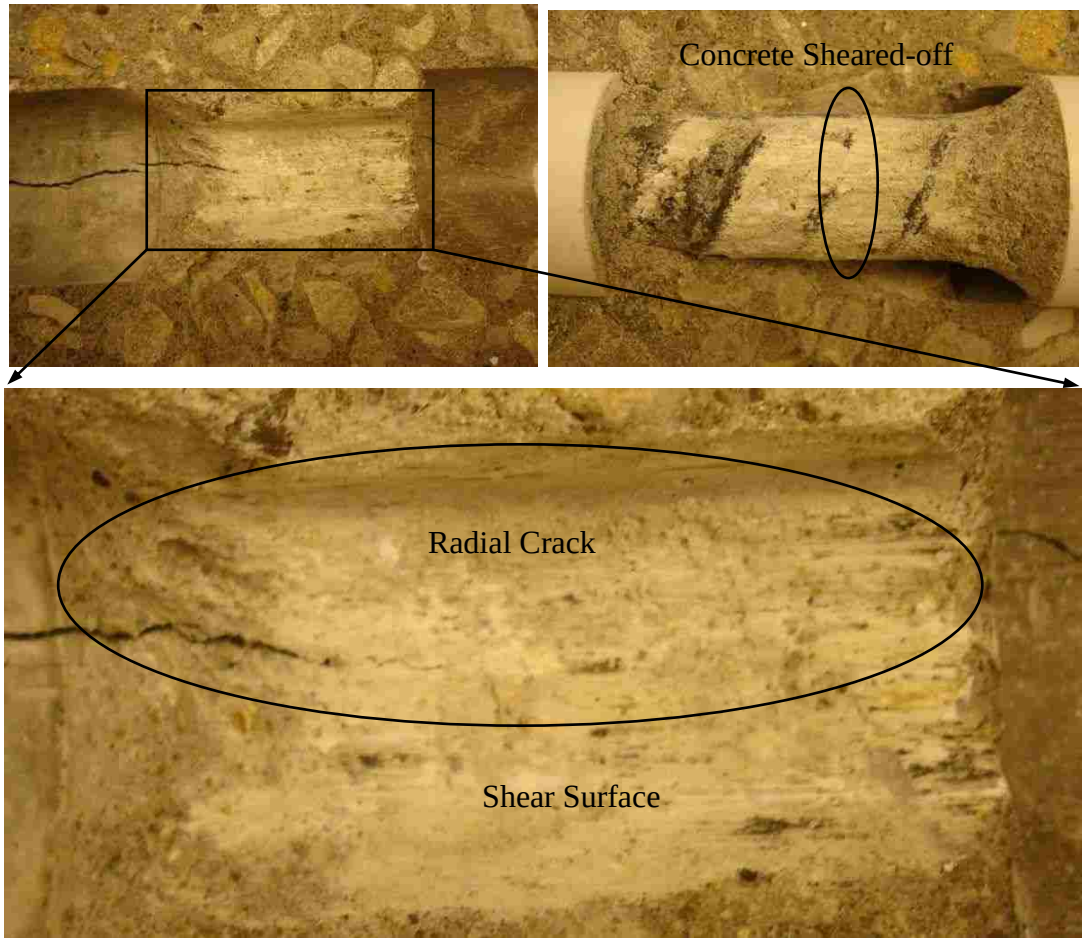

Figure 3.13. Combined Shear-off and Splitting Actions of Confined Cylinder

3.6.3 Local Concrete Crushing. As stated earlier, the same failure modes (Mode IIA) were observed for unconfined specimens with and without enamel coated rebar, both involving concrete crushing and splitting. However, close examinations on the interfaces of failed specimens revealed that the concrete crushing zone (represented by a crushing angle α and a crushing length L) for enamel coated rebar was significantly larger than that for uncoated rebar as illustrated in Figure 3.12(c). The crushing angle α_c (the crushing length L_c) for coated rebar is smaller (larger) than α_u (L_u) for uncoated rebar. The crushing angle and length of all unconfined specimens included in Tables 3.3 and 3.4 verified the illustration in Figure 3.12(c). This is because the rougher surface and thus higher frictional resistance of enamel coated rebar with surrounding concrete allowed a smaller portion of a concrete key between two adjacent ribs to be mobilized as the rebar was pulled out of the concrete cylinder.

The concrete crushing angle played an important role in the bond strength. In the analytical study by Cairns and Jones (1995), the bond strength was found to be inversely proportional to the tangent of the concrete crushing angle. Therefore, a smaller crushing angle indicates a higher bond strength. It was also found during the forensic study that the crushing angle increased along the rebar from the loading end as illustrated in Figure 3.12(d) and evidenced in Figure 3.14 for specimen N6C3_5L1. The increase in crushing angle from Zone 4 to 1 was likely due to the decreasing radial stress along the rebar. Figure 3.15 clearly indicated that the crushing angle decreased with the increase of c/d_b due to the increase in concrete confinement and thus the frictional resistance from the coating effect.

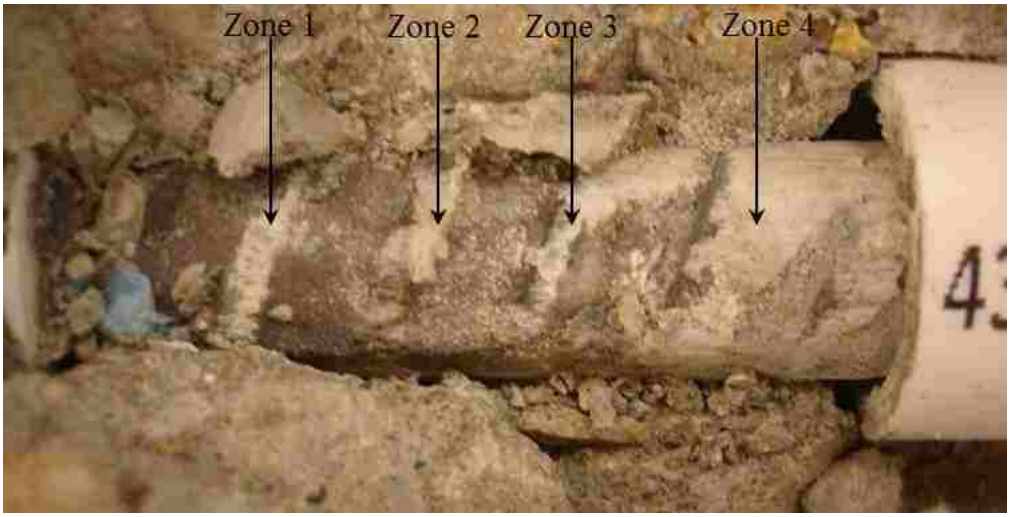

Figure 3.14. Variation of Crushing Zones of Unconfined Cylinder at Rib Fronts

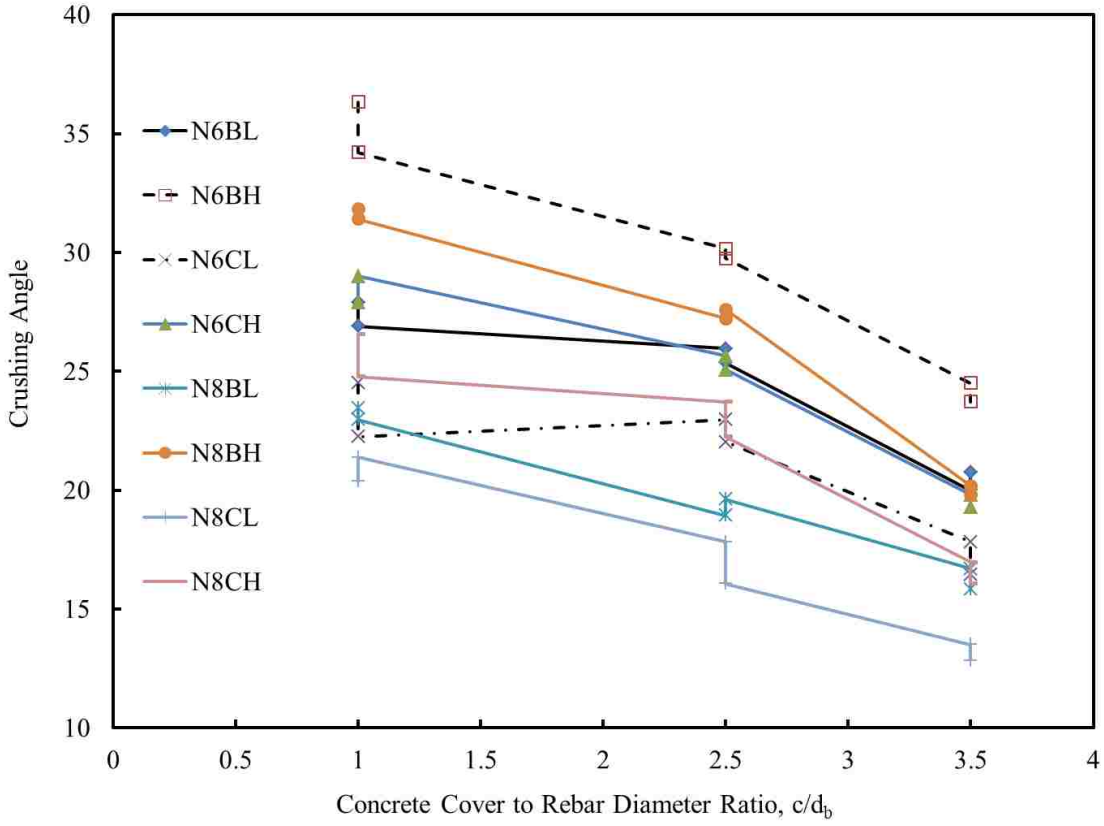

Figure 3.15. Change of Crushing Angles with Concrete Cover to Rebar Diameter Ratio (Unconfined Specimens)

3.7. SUMMARY

Based on the test results and analysis of 96 specimens, 48 with coated rebar and 48 with uncoated rebar, the following conclusions can be drawn:

(1) The use of vitreous enamel coating can increase the bond strength of deformed rebar in normal strength concrete. Overall, an average increase of approximately 15% in bond strength was observed, taking into account the effects of confinement (with and without steel jacket), rebar size [No. 19 (#6) and No. 25 (#8)], and concrete cover (1.0, 2.5, and 3.5 times the rebar diameter). This is likely because the surface of enamel coated rebar became roughened and the chemical adhesion was increased between the calcium silicate in the enamel coating and the cement matrix of the concrete.

(2) Unconfined specimens failed suddenly due to concrete splitting. The failure of confined specimens was initiated with concrete splitting and ultimately ended with shear-off of the concrete keys between rebar ribs as the rebar was pulled out of the concrete cylinders. However, the bond slip required from concrete splitting to shear-off is often small. In most cases, bond strengths were achieved at concrete splitting.

(3) Confinement slightly increased the bond strength of coated rebar in concrete, which is controlled by concrete splitting, from 15% to 17% with No. 19 (#6) rebar and from 11% to 15% with No. 25 (#8) rebar. However, the confinement provided by steel jackets can retain a significant portion of the post-peak residual strength. Steel jackets provided a passive confinement mechanism to rebar in concrete cylinders, resembling the effect of stirrups on main reinforcement in RC members.

(4) As the size of rebar increased from No. 19 (#6) to No. 25 (#8), the rib bearing effect against concrete increased significantly; thus the other two contributors to the rebar-concrete bond strength, chemical adhesion and frictional effects that can be enhanced by enamel coating, became less important. As a result, the bond strength decreased with the rebar size.

(5) Compared to uncoated rebar, enamel coated rebar was pulled out of the concrete cylinders with a smaller concrete crushing angle due to the increase in frictional resistance between the rebar and concrete. The crushing angles also changed slightly along the length of the rebar mainly due to the uneven distribution of radial stresses.

Future investigations will be directed to understanding the local bond behavior of enamel coated rebar in high strength concrete under cyclic and rapid loadings. Empirical and analytical bond-slip models for enamel coated rebar will be established to facilitate future engineering design and analysis of RC structures.

4. GLOBAL BOND THEORY AND VALIDATION WITH MEMBER TESTING

4.1. INTRODUCTION

This chapter presents an analytical model for the bond stress of lapped splice in normal strength concrete. The parameters used in this model include the rebar and concrete characteristics and splice length. The model can facilitate the estimation of development length in the absence of test data for local bond-slip relationships. It is also developed to transform the rebar-concrete interaction from local to global bond behavior and provide a direct approach for the performance evaluation of enamel coating. In the latter case, the maximum crack spacing and strain predicted with the proposed model can be used as an effective index for the measure of coating performance.

Due to the complexity in geometry, load transfer, and damage process, almost all the existing studies on the global bond behavior of lap spliced reinforcement in concrete were conducted experimentally with data regression analysis. This study represents the first attempt to formulate an analytical solution of the flexural members with lap spliced rebar in concrete. The simplified closed-form solution is validated with testing of reinforced concrete beams and columns.

4.2. THEORETIC ANALYSIS

This section presents a detailed analysis of both local and global bond behavior. The local bond strength is analyzed using the similar concept as proposed by Wu et al. (2012). The group effect and shear failure caused by rebar splicing is considered separately. Confining stress is obtained by idealizing the spliced rebar as an internally pressurized elliptical thick-walled cylinder as shown in Figure 4.1. Strain softening in concrete is considered at crack locations to reflect the discontinuity in members.

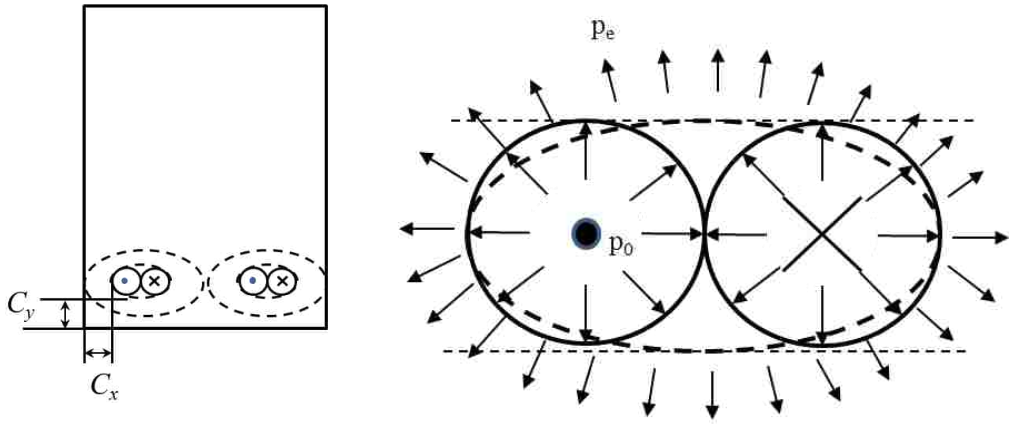

Figure 4.1. Elliptical Thick-walled Cylinder and Equivalent Elliptical Section

4.2.1 Bond Strength of Lap Spliced Joints of a Single Rebar.

4.2.1.1 Effect of concrete cover. Lap splice without transverse reinforcement and insufficient development length tends to fail in concrete cover splitting. The stress fields generated by two pieces of rebar in the lap splice will interact with each other and form a combined stress field. Orangun et al. (1977) suggested that an oval shape of hoop stress field in the splice area should be considered around each rebar individually. However, the bundle effect and non-uniform bursting pressure exist for the two rebar pieces in the splice joint. Therefore, an equivalent elliptical shape of hoop stress field around the two rebar pieces is considered and illustrated in Figure 4.1. The major and minor radii of the equivalent ellipse are equal to the diameter and radius of a single rebar piece, respectively. The internal pressure of the equivalent ellipse p_e is obtained from the pressure from individual rebar pieces p_0 by

$$p_0\, 2\pi d_b \approx p_e\, 2\pi \sqrt{\frac{(\frac{d_b}{2})^2 + d_b^{\,2}}{2}}, \quad p_e \approx p_0 \sqrt{1.6} \tag{4.1}$$

in which d_b denotes the diameter of rebar. Here, the left side of Eq. (4.1) is twice as much as the total pressure force along the entire perimeter of each rebar piece. The right side of Eq. (4.1) represents the approximate total pressure force of the equivalent ellipse. The equivalent pressure is then used as the maximum confining pressure that concrete cover can bear prior to splitting.

4.2.1.2 Effect of transverse reinforcement. The confinement effect from the stirrups was analyzed as an additional hydro-pressure that the concrete cover can sustain. The additional pressure provided by the confining reinforcement was calculated from the classical thick wall cylinder theory. The ultimate bond strength τ_u for the confined condition can then be determined form the pressure through a function $\tau_u(.)$ that depends upon the local bond behavior based on confinement effect as discussed in Section 1.2.1 and can be formulated as derived in Chapter 2.

$$\tau_u = \tau_u(p_e + p_{tr}) \tag{4.2}$$

$$p_{tr} = \frac{2\sigma_{tr}A_{tr}}{s\,d_{tr}} \tag{4.3}$$

in which p_{tr} is the additional pressure due to steel stirrups, and σ_{tr}, A_{tr}, s, and d_{tr} are respectively the stress, the cross sectional area, the spacing, and the diameter of transverse rebar. The stress in confining reinforcement was estimated to be 62.05 MPa (9 ksi) based on the findings by Canbay and Frosch (2005).

4.2.2 Local Bond-slip Law. Similar to the CEB-FIP (2000), the bond-slip relationship can be described by the following equation:

$$\tau[\delta(x)] = \begin{cases} \left(\dfrac{\delta(x)}{\delta_1}\right)^{\lambda} \tau_u, \delta(x) < \delta_1 \\ \exp\{-\alpha[\delta(x) - \delta_1]/(\delta_2 - \delta_1)\}, \delta_1 \le \delta(x) \le \delta_2 \end{cases} \tag{4.4}$$

where τ_u in Eq. (4.2) is also referred to as the peak bond stress at slip δ_1, λ is equal to 0.8 and 1.2 for uncoated and enamel-coated rebar through curve fitting to the experimental data (Wu et al. 2012), $\alpha = 4$ for both types of rebar, δ_1=6 mm (0.24 in.) and δ_2=20 mm. (0.79 in.)

4.2.3 Slip Function at Short Lapped Splice. Since the bond stress is a function of the relative slip between the spliced rebar and concrete, the slip distribution along the lapped splice is crucial in the interpretation of the interface behavior. An elastic or elasto-plastic slip behavior can be defined based on the splice length or anchorage length (Fernández et al. 2007). For a short embedment length l_s *(*$<5d_b$*)*, the rebar behaves like a

rigid member and experiences a constant slip over the embedment length under tension or compression.

4.2.4 Slip Function at Long Lapped Splice. For a long embedment length l_s *(>5d_b)*, non-uniform slip occurs and the bond stress depends on not only the rebar strain ε_s but also the concrete strain ε_c including the crack opening caused by the tension force. In this case, the relative slip between the rebar and concrete can be evaluated by:

$$\delta(x) = \int_0^x (\varepsilon_s - \varepsilon_c) dx \tag{4.5}$$

Taking a second derivative of the slip function and considering the stress-strain relationship of materials yield to:

$$\frac{d^2\delta(x)}{dx^2} = \frac{d\sigma_s(x)}{dx}\left(\frac{1}{E_s} + \frac{a_s}{E_c c_{eff}}\right) \tag{4.6}$$

where $\sigma_s(x)$ is the stress function in steel rebar, E_s and E_c are respectively the modulus of elasticity for reinforcement and concrete, a_s is the area of the reinforcement being spliced, c_{eff} is the effective concrete section that contributes to the bond stress and is defined by the rebar diameter and the clear concrete cover on each side as illustrated in Figure 4.1. By setting up the equilibrium equation of the rebar, the stress in rebar can be related to the bond stress by:

$$\frac{d\sigma_s(x)}{dx} = \frac{\tau[\delta(x)]\pi d_b}{a_s} \tag{4.7}$$

After introducing Eq. (4.7), Eq. (4.6) can then be written into:

$$\frac{d^2\delta(x)}{dx^2} - \left(\frac{1}{E_s a_s} + \frac{1}{E_c c_{eff}}\right)\pi d_b \cdot \tau[\delta(x)] = 0 \tag{4.8}$$

If x for each rebar is defined to start from the point of zero slip ($x_0 = 0$ in Figure 4.2) in the slip function, two boundary conditions $\delta(0) = 0$ and $\delta'(0) = 0$ can be used to solve Eq. (4.8) and yield a slip function prior to the peak bond stress:

$$\delta(x) = \frac{\left[\left(\frac{1}{E_s a_s} + \frac{1}{E_c c_{eff}}\right)\pi d_b\right]\tau_u \cdot x^{\lambda+2}}{(\delta_1)^{\lambda}(\lambda+1)(\lambda+2)} \tag{4.9}$$

The relative slip between the two rebar is a sum of the slip functions from two individual rebar as shown in Figure 4.2. When the stress transferred from the rebar to concrete exceeds the tensile strength of the concrete, a bond-related crack appears, the stress in rebar is redistributed, and the slip function changes locally as illustrated in Figure 4.3.

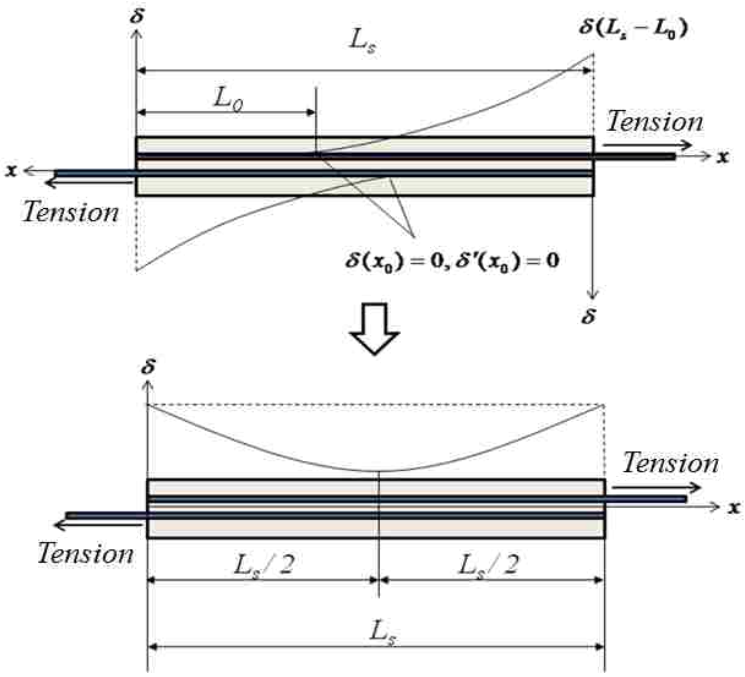

Figure 4.2. Slip Distribution of Rebar in Splice with Uncracked Concrete

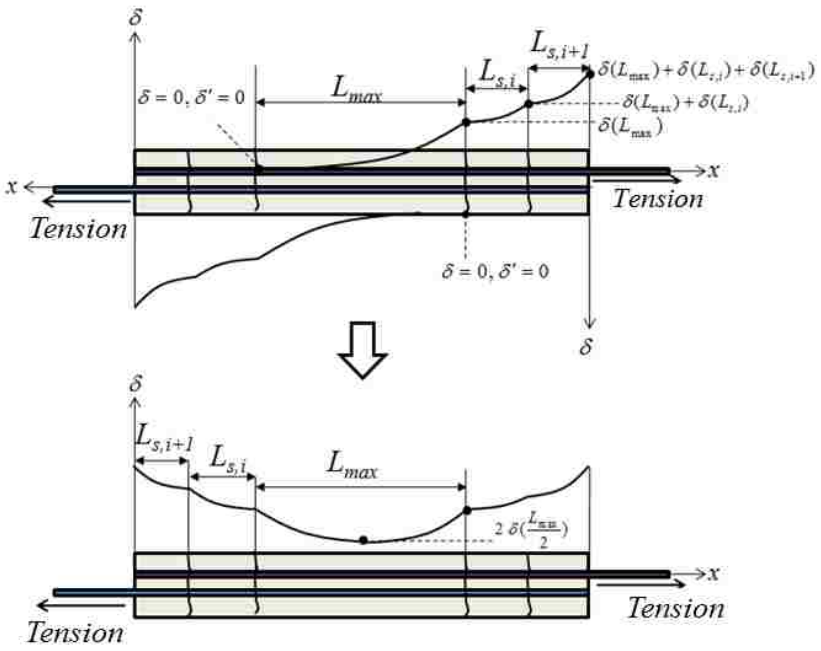

Figure 4.3. Slip Redistribution of Rebar with Cracked Concrete

The distance between two concrete cracks is defined as the crack spacing as illustrated in Figure 4.3. The concrete stress over the crack spacing is always lower than the tensile strength of concrete. The bond stress transferred to concrete over this distance is equal to the strain variation in the rebar. The maximum crack spacing L_{max} can be determined iteratively by the following equation of forces applied on the effective concrete section:

$$\sum F_c(L_{\max}) = 2 f_{tu} c_{eff} \exp[-2\delta(L_{\max}) / (\varepsilon_{tu} L_{\max})] \tag{4.10}$$

$$\sum F_c(L_{\max}) = \sum F_c(\frac{L_{\max}}{2}) - \sum F_s(L_{\max}) = 2 f_{tu} c_{eff} - d_b \pi \int_0^{L_{\max}} \tau[\delta(x)] dx \tag{4.11}$$

in which $F_c(.)$ and $F_s(.)$ are respectively the concrete and rebar forces as a function of location in the bracket, and the summation is for two rebar pieces in the lap spliced joint. It should be noted that the exponential strain-softening model used in the unified bond model in Chapter 2 is adopted here. To reduce computational efforts, the average strain of rebar within the maximum crack spacing is approximately used to represent the overall response in the splice region. The total tension force applied to rebar in the splice region

can be computed from the moment-curvature analysis of a beam under the bending moment at the splice location.

For short embedment lengths or thin concrete covers, a premature failure is expected. For long embedment lengths, three response stages occurred under loading: concrete cracking, zero-slip point shifting, and rebar yielding as illustrated in Figure 4.3. The average strains in the three stages are derived as follows.

4.2.4.1 Prior to concrete cracking. Before the concrete in a tension zone reaches its ultimate tensile strength, no concrete crack occurs, the concrete is perfectly bonded to the embedded rebar, and the concrete and the rebar works as a composite. In this case, the strain relation at the rebar-concrete interface and the Hookie's law for the steel rebar can be expressed into:

$$\varepsilon_s = \varepsilon_c, \ \sigma_s = E_s\varepsilon_s = E_s\varepsilon_c = \sigma_c n \tag{4.12}$$

Then, the total force carried by the rebar and the effective concrete section F_{cs} can be calculated by a summation of the forces by the concrete F_c and the rebar F_s:

$$F_{cs} = F_c + F_s = (a_s E_s + c_{eff} E_c)\varepsilon_c \tag{4.13}$$

Thus, the average strain of the rebar, which is bound by the ultimate tensile strain in concrete, can be estimated by:

$$\varepsilon_{s,avg} = \varepsilon_c = \varepsilon_s = \frac{F_{cs}}{(a_s E_s + c_{eff} E_c)} \le \frac{f_{tu}}{E_c} \tag{4.14}$$

4.2.4.2 Zero-slip point shifting - treated as overlapped effect of rebar. When the stress in concrete at one point exceeds the concrete tensile strength, a bond related crack is initiated at that point. After that, the zero-slip point is shifted from the approximately mid-point of the maximum crack spacing to the open crack by reducing x_0 as illustrated in Figure 4.4.

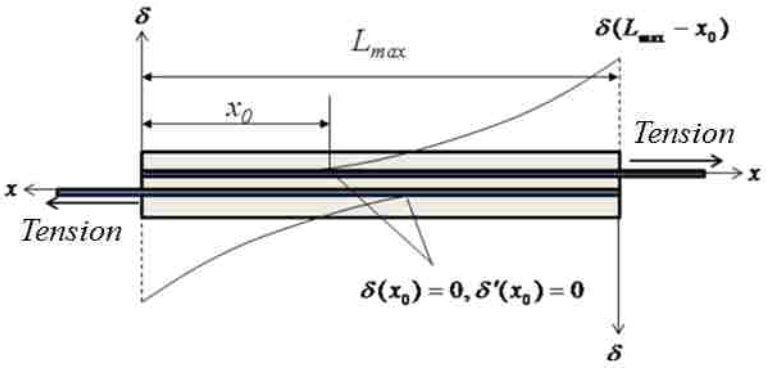

Figure 4.4. Zero-slip Point Shifting (decreasing x_0)

As a result of the zero-slip point shifting, the bond stress, concrete stress, and rebar stress are changed correspondingly with the relative slip function. Let the zero slip occur at a distance of x_0 away from the end of rebar in the spliced area. The bond stress transferred to concrete over the maximum crack spacing L_{max} can be evaluated by:

$$F_{bs}(L_{\max}) = d_b \pi \int_0^{L_{\max}-x_0} \tau[\delta(x)]dx \tag{4.15}$$

The tensile force of concrete at the opening can be determined from:

$$F_c(L_{\max}) = f_{tu} c_{eff} \exp[-2[\delta(L_{\max})/(\varepsilon_{tu} L_{\max})] \tag{4.16}$$

At the zero-slip point, the rebar is subjected to the same strain as the surrounding concrete. Therefore, the rebar force $F_s(0)$, concrete force $F_c(0)$ and the total force $F_{cs}(0)$ at the zero-slip point are related by,

$$F_s(0) = E_s \varepsilon_s(0) a_s = E_s \varepsilon_c(0) a_s = \frac{a_s n}{c_{eff}} F_c(0) \tag{4.17}$$

$$F_{cs}(0) = F_s(0) + F_c(0) = (1 + \frac{a_s n}{c_{eff}}) F_c(0) \tag{4.18}$$

Considering that the total force remains constant over the crack spacing, the total force at any point within the crack spacing is

$$F_{cs}(L_{\max}) = F_{cs}(0) = (1 + \frac{a_s n}{c_{eff}}) F_c(0) \tag{4.19}$$

Therefore the average strain of rebar within the maximum crack spacing can be computed by:

$$\varepsilon_{s,avg} = \frac{2\int_0^{L_{\max}} \varepsilon_s dx}{L_{\max}} = \frac{2}{L_{\max}} \left\{ \varepsilon_s(0) L_{\max} + \int_{x_0}^{L_{\max}} \frac{d_b \pi}{a_s E_s} \left\{ \int_0^{L_{\max}-x_0} \tau[\delta(y)] dy \right\} dx \right\} \quad (4.20)$$

4.2.4.3 Rebar yielding and steady increase of slip. After the zero-slip point rests at an open crack on the rebar end side or $x_0 = 0$ after shifting, the slip at the other end of the crack spacing increase steadily and the steel rebar at that point may eventually start yielding. Therefore, the bond stress transferred from the rebar to concrete is bounded to the yield strength F_{sy} as indicated by:

$$F_s = d_b \pi \int_0^{L_{\max}} \tau[\delta(x)] dx \le F_{sy} \quad (4.21)$$

The increase in slip causes reduced concrete stresses around the open cracks at the other end of crack spacing $\delta(L_{\max})$, which can be computed by:

$$F_c(L_{\max}) = f_{tu} c_{eff} \exp[(-2\delta(L_{\max}) / (\varepsilon_{tu} L_{\max})] \quad (4.22)$$

The concrete force at mid-point of the crack spacing can be written as

$$F_c(0) = F_c(L_{\max}) + F_{bs} \quad (4.23)$$

The displacements in the rebar and concrete at the other hand of the crack spacing must meet the following compatibility condition:

$$u_s(L_{\max}) - u_c(L_{\max}) = \delta_e(L_{\max}) \quad (4.24)$$

By integrating the strains over one crack spacing, the rebar and concrete displacements at the end of the crack spacing can be computed by:

$$\begin{aligned} \delta(L_{\max}) = & \int_0^{L_{\max}} \left\{ \varepsilon_s(0) + \frac{d_b \pi}{a_s E_s} \int_0^x \tau[\delta(y)] dy \right\} dx \\ & - \int_0^{L_{\max}} \left\{ \varepsilon_c(0) - \frac{d_b \pi}{c_{eff} E_c} \int_0^x \tau[\delta(y)] dy \right\} dx \end{aligned} \quad (4.25)$$

Or

$$F_s(0) = \frac{a_s E_s}{L_{\max}} \left\{ \delta(L_{\max}) + \int_0^{L_{\max}} \left[\frac{F_c(0)}{c_{eff} E_c} - \left(\frac{1}{c_{eff} E_c} + \frac{1}{a_s E_s} \right) F_{bs}(x) \right] dx \right\} \quad (4.26)$$

after $\varepsilon_s(0) = F_s(0) / a_s E_s$ and $\varepsilon_c(0) = F_c(0) / c_{eff} E_c$ have been introduced to Eq. (4.25). Thus, the total displacement by two anchorage bars in the lap spliced joint is

$$\sum u_{cs} = 2\int_0^{L_{\max}} \left[\frac{F_s(0) + F_{bs}(x)}{a_s E_s} \right] dx \tag{4.27}$$

Finally, the average strain can be calculated by:

$$\varepsilon_{s,avg} = \frac{2\int_0^{L_{\max}} \varepsilon_s dx}{L_{\max}} = \frac{\sum u_{cs}}{L_{\max}} \tag{4.28}$$

This loading stage continues until the rebar starts yielding as the bond stress exceeds the yield strength of steel. The key material properties of rebar, concrete, and rebar-concrete interface can be obtained from standard mechanical tests. For example, the stress-strain relationship of rebar as shown in Figure 3.1 (Chen et al. 2010) is used in this study.

4.3. MODEL VALIDATION RESULTS AND DISCUSSION

To validate the proposed model, test data sets from the testing of beam and column specimens with spliced joints are used. As detailed in Chen et al. (2010) and Wu et al. (2012), a total of 24 beam specimens (12 with enamel-coated reinforcement and 12 with uncoated reinforcement) and 2 large-scale column specimens (1 with enamel-coated reinforcement and 1 with uncoated reinforcement) were tested.

4.3.1 Beam Specimens with Lapped Splice Rebar. The details of beam specimens are shown in Figures 4.5 and 4.6 for No. 19 (#6) and No. 25 (#8) steel reinforcing bars. All specimens were loaded monotonically to failure under a four-point loading configuration (Chen et al. 2010). Various lengths of splice were considered as indicated in Figures 4.5 and 4.6. The main reinforcement size, coating type, splice length, confinement condition, and material properties are given in Table 1. The beams with enamel-coated rebar have higher loading capacity than those with uncoated rebar, indicating a desirable bond performance of enamel-coated rebar.

4.3.2 Column Specimens with Dowel Rebar. Two column specimens were tested under a cyclic load applied to the top end of the columns as shown in Figure 4.7. Due to the horizontal load, the column-footing joint was subjected to a bending moment. A post-tensioning axial force along the centerline of each column was applied simultaneously to simulate the vertical live load in practical applications.

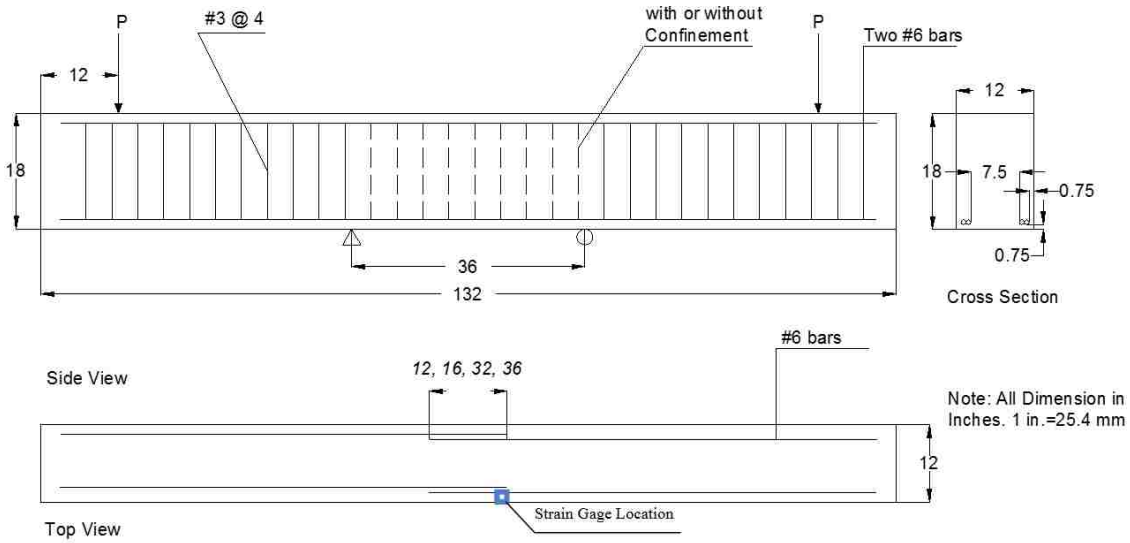

Figure 4.5. Details of Beam Specimens with No. 19 (#6) Rebar Splices

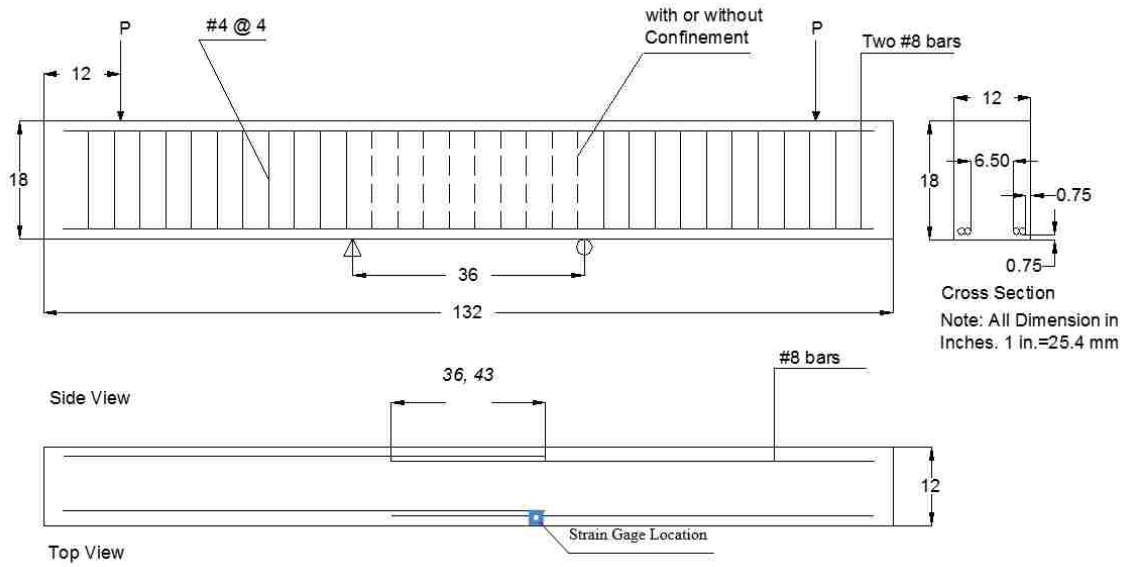

Figure 4.6. Details of Beam Specimens with No. 25 (#8) Rebar Splices

Both columns were loaded to failure in the splice region. The column with enamel-coated reinforcement failed at a higher load and with less damage than that with

uncoated reinforcement. The proposed analytical model was used to analyze the structural behaviors of various tested specimens. The numerical results were compared with the experimental data in terms of the maximum crack spacing and the load-strain curves. It should be noted that the classic moment-curvature method was used to calculate the strain in lap spliced rebar. The effective tension concrete sections for both beams and columns are shown in Figure 4.8 according to the CEB-FIP code requirement. In Figure 4.8, c and d_b represent the clear concrete cover and rebar diameter, respectively. Material properties of the columns are also included in Table 4.1.

4.3.3 Maximum Crack Spacing. The maximum crack spacing for each beam specimen is listed in Table 4.2. It can be seen from Table 4.2 that a good agreement has been achieved between the analytical and experimental results. The maximum relative error in crack spacing prediction is 5.56%. There seems no general trend in terms of under or over prediction of the crack spacing. In particular, the use of enamel coating tends to reduce the maximum crack spacing for all except the two beam specimens with No. 25 （#8） rebar as main reinforcement and no transverse rebar confinement. The reduction in crack spacing reflects the effective increase of bond strength with enamel-coated rebar.

Table 4.1. Coating Type, Splice Length, Confinement, and Material Properties

Specimen Rebar Size Coating	Splice Length (in.)	Confinement	Concrete Compressive Strength (ksi)	Modulus of Elasticity of Concrete (ksi)	Modulus of Elasticity of Reinforcement (ksi)
Beam #6 Uncoated	12	Unconfined	4.0	3600	31760
Beam #6 Uncoated	12	Confined	4.0	3600	31760
Beam #6 Coated	12	Unconfined	4.0	3600	31760
Beam #6 Coated	12	Confined	4.0	3600	31760
Beam #6 Uncoated	16	Unconfined	4.0	3600	31760
Beam #6 Uncoated	16	Confined	4.5	3820	31760
Beam #6 Coated	16	Unconfined	4.0	3600	31760
Beam #6 Coated	16	Confined	4.5	3820	31760
Beam #6 Coated	32	Unconfined	4.0	3600	31760
Beam #6 Coated	32	Confined	4.0	3600	31760
Beam #6 Coated	36	Unconfined	4.0	3600	31760
Beam #6 Coated	36	Confined	4.0	3600	31760
Beam #8 Uncoated	36	Unconfined	4.5	3820	29880
Beam #8 Uncoated	36	Confined	5.5	4227	29880
Beam #8 Coated	36	Unconfined	4.0	3600	29880
Beam #8 Coated	36	Confined	4.5	3820	29880
Beam #8 Uncoated	43	Unconfined	4.0	3600	29880
Beam #8 Uncoated	43	Confined	4.0	3600	29880
Beam #8 Coated	43	Unconfined	4.0	3600	29880
Beam #8 Coated	43	Confined	4.0	3600	29880
Column #8 Uncoated	20	Confined	6.3	3600	29880
Column #8 Coated	20	Confined	6.3	4415	29880

*1 in=25.4 mm.; 1 psi=0.006895 MPa

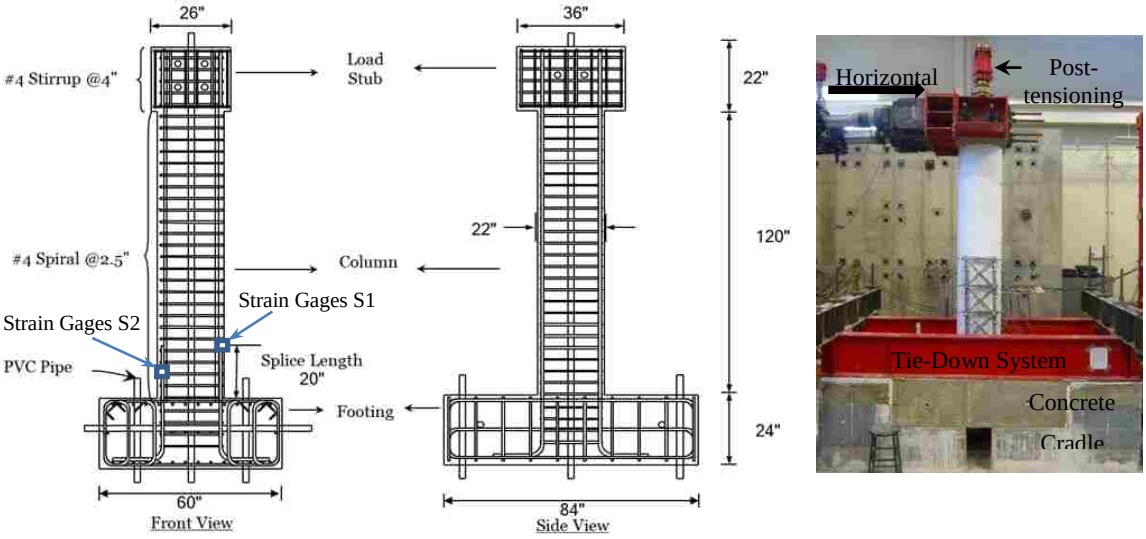

(a) Reinforcement details (b) Test setup

Figure 4.7. Details of Column Specimens (1in. = 25.4 mm.)

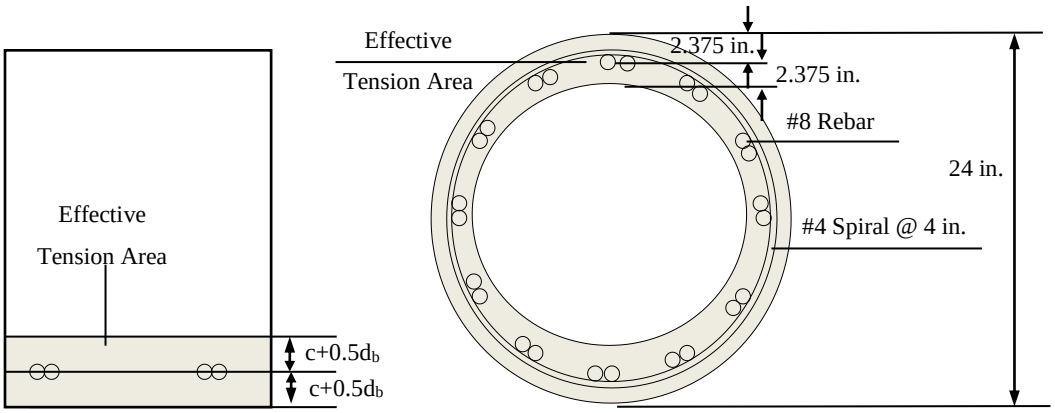

(a) Beam (b) Column

Figure 4.8. Detail of Effective Areas for Composite Section (1in. = 25.4 mm.)

Table 4.2. Maximum Crack Spacing

Specimen	Splice Length (in.)	Confinement	Maximum Crack Spacing		
			Experimental (in.)	Analytical (in.)	Error (%)
Beam #6 Uncoated	12	Unconfined	5.8	5.92	2.07
Beam #6 Uncoated	12	Confined	5.6	5.65	0.89
Beam #6 Coated	12	Unconfined	5.5	5.68	3.27
Beam #6 Coated	12	Confined	5.0	4.98	-0.40
Beam #6 Uncoated	16	Unconfined	6.4	6.45	0.78
Beam #6 Uncoated	16	Confined	6.0	5.95	-0.83
Beam #6 Coated	16	Unconfined	6.0	6.25	4.17
Beam #6 Coated	16	Confined	5.5	5.25	-4.55
Beam #8 Uncoated	36	Unconfined	5.0	4.75	-5.00
Beam #8 Uncoated	36	Confined	4.5	4.65	3.33
Beam #8 Coated	36	Unconfined	5.0	4.55	1.00
Beam #8 Coated	36	Confined	4.5	4.25	-5.56
Column#8Uncoated	20	Unconfined	7.0	6.89	-1.57
Column #8 Coated	20	Confined	6.0	6.12	2.00

*1 in=25.4 mm.

4.3.4 Load-strain Curves. Strain gages (7.62 cm or 3 in. long) were installed on the main reinforcement of beams at the end of a spliced joint as shown in Figures 4.5 and 4.6 and on the main reinforcement of columns at the middle (S1) and end (S2) of a spliced joint as shown in Figure 4.7. The load-strain curves of each pair of beams with uncoated and coated rebar were plotted on the same graph in Figures 4.9 to 4.14. The load-strain curves of columns were plotted in Figure 4.15. The simulation results of the corresponding specimens were also plotted for comparison with the experimental results.

It can be observed from Figures 4.9 to 4.14 that the experimental load-strain curves in each pair of beams are compared well from linear responses prior to and after concrete cracking to nonlinear responses in terms of premature splice failure or steel yielding. The main difference in each pair of beams lies in the ultimate strain at failure since the maximum slip and local bond stress are higher in the specimen with enamel-

coated rebar (Chen et al. 2010). Therefore, the concrete with enamel-coated reinforcement can transfer higher stress and thus induce higher strain in the coated rebar.

Since the coating effect is taken into account in the proposed analytical model, the computed strain is in good agreement with the experimental data except for some details corresponding to local cracking in concrete. In particular, the highly nonlinear response and complicated behavior near the failure of specimens are simulated to the satisfactory accuracy in engineering applications. That is, the increased strength of local bond between the enamel-coated rebar and concrete has been successfully implemented in the prediction of the ultimate tension load that the splice joints can support.

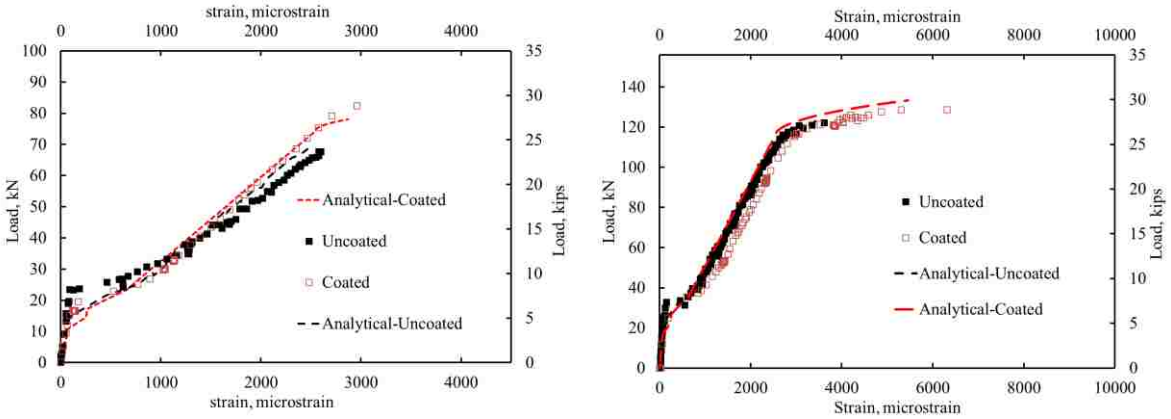

(a) Unconfined (b) Confined

Figure 4.9. Load-strain Curves of Beams with No.19 Rebar and 304 mm. Splice Length

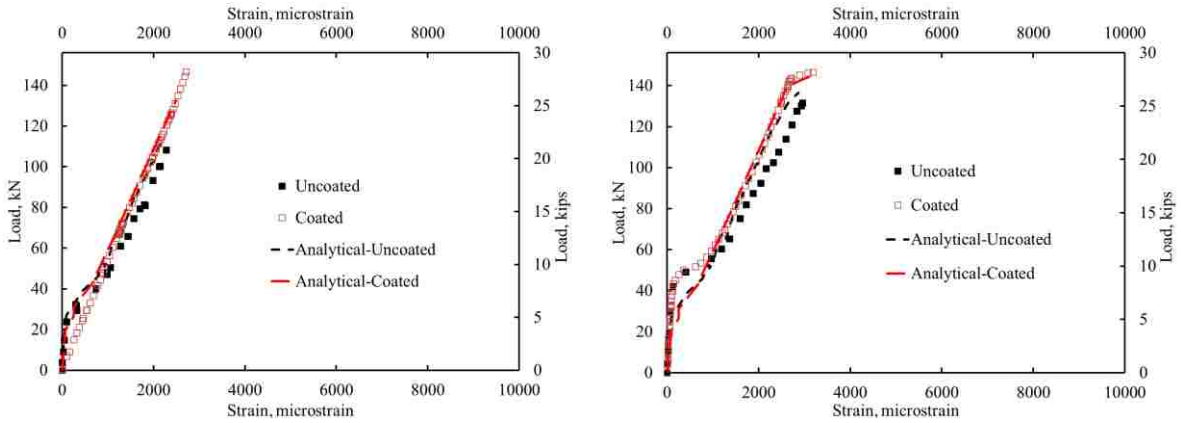

(a) Unconfined (b) Confined

Figure 4.10. Load-strain Curves of Beams with No.19 Rebar and 406 mm. Splice Length

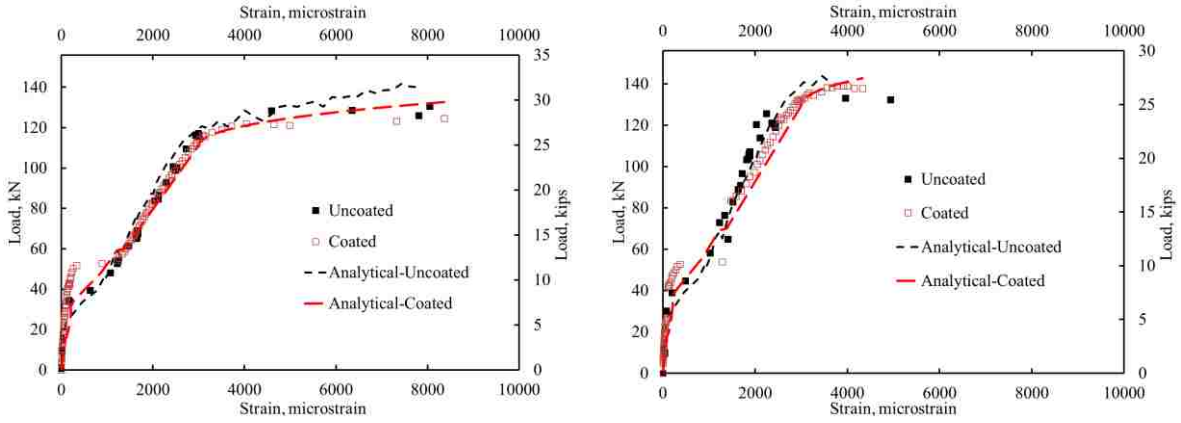

(a) Unconfined (b) Confined

Figure 4.11. Load-strain Curves of Beams with No.19 Rebar and 812 mm. Splice Length

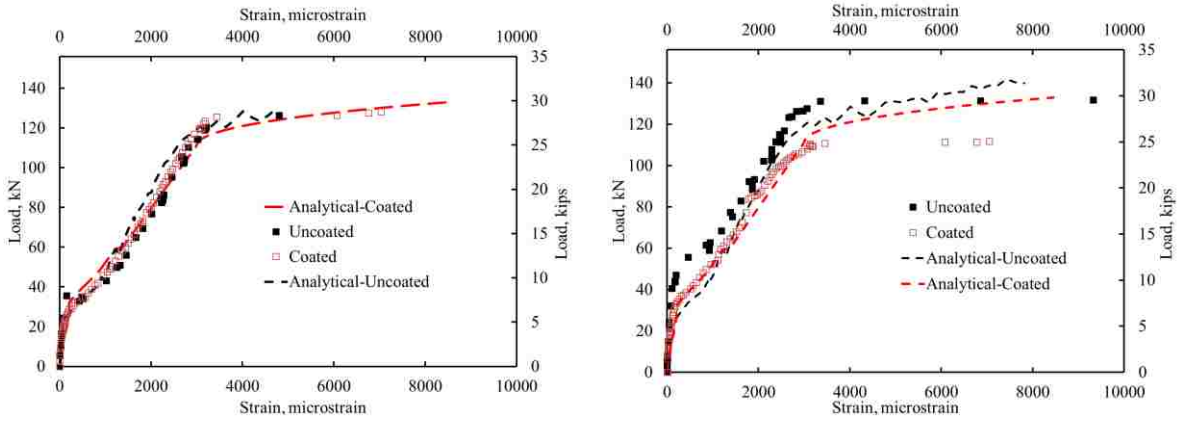

(a) Unconfined (b) Confined

Figure 4.12. Load-strain Curves of Beams with No.19 Rebar and 914 mm. Splice Length

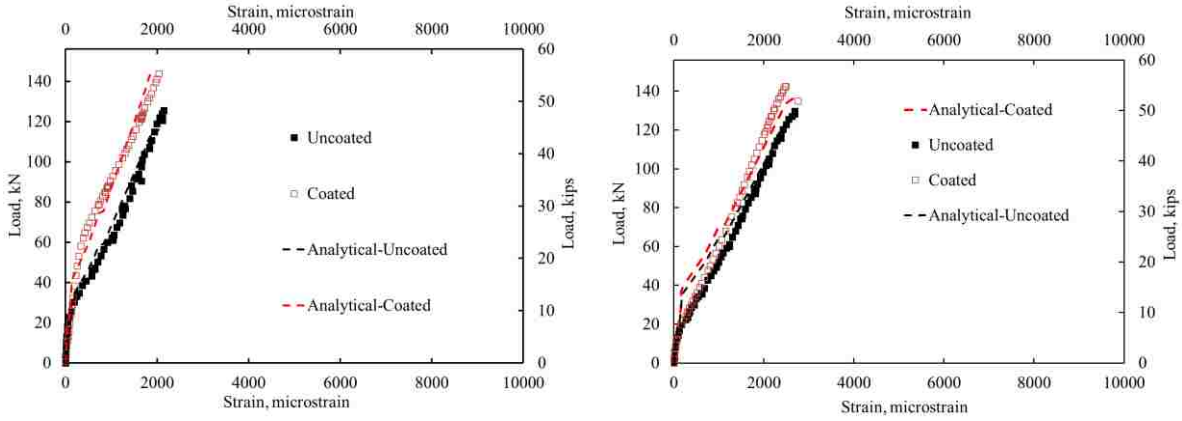

(a) Unconfined (b) Confined

Figure 4.13. Load-strain Curves of Beams with No.25 Rebar and 914 mm. Splice Length

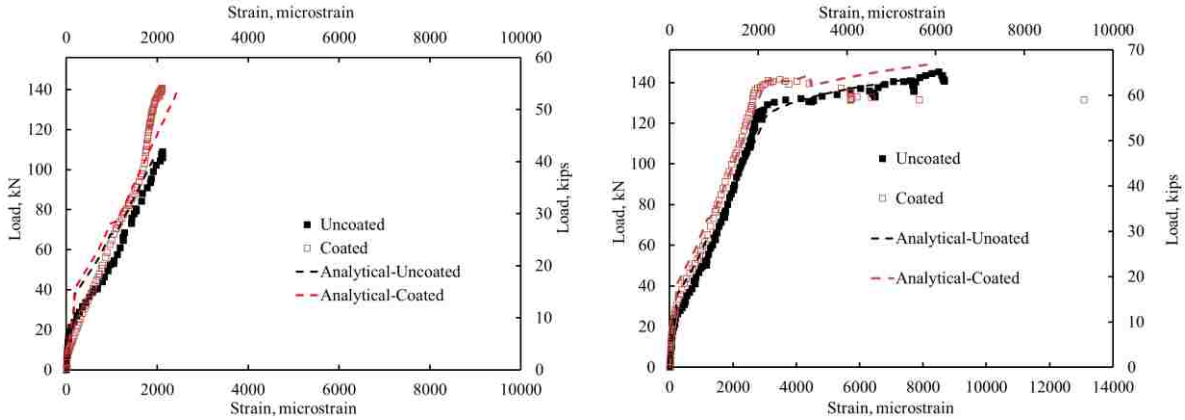

(a) Unconfined (b) Confined

Figure 4.14. Load-strain Curves of Beams with No.25 Rebar and 1 m. Splice Length

The average prediction errors for beam specimens are summarized in Table 4.3. Since the proposed model used strain control, the predicted load at each increment was compared with the experimental data. Overall, the average errors range from 4.67% to 25.6%. The average errors for the confined specimens range from 4.67% to 19.4%, which is more consistent than those for unconfined specimens.

The predicted strains of the tested columns are compared in Figure 4.15 with experimental results. At each location (S1 and S2 shown in Figure 4.7), a pair of strain gages were installed and two sets of data were collected. The comparison between the experimental and analysis showed that the prediction falls in the range of the scattered data. Therefore, a good agreement was achieved using the proposed model. It should be noted here that, although cyclic loading may have caused accumulated damage on the splice, the accumulated damage was not significant enough to alter the applicability of the proposed model developed for monotonic loading. It can be seen from Figure 4.15 that the strain levels are relatively low.

Table 4.3. Prediction Error using the Proposed Model

Specimen	Splice Length (in)	Confinement	Average Error in Load Prediction (%)
Beam #6 Uncoated	12	Unconfined	18.60
Beam #6 Uncoated	12	Confined	4.67
Beam #6 Coated	12	Unconfined	12.32
Beam #6 Coated	12	Confined	8.39
Beam #6 Uncoated	16	Unconfined	7.31
Beam #6 Uncoated	16	Confined	12.84
Beam #6 Coated	16	Unconfined	24.00
Beam #6 Coated	16	Confined	11.25
Beam #6 Coated	32	Unconfined	23.20
Beam #6 Coated	32	Confined	18.60
Beam #6 Coated	36	Unconfined	15.20
Beam #6 Coated	36	Confined	19.40
Beam #8 Uncoated	36	Unconfined	7.80
Beam #8 Uncoated	36	Confined	10.60
Beam #8 Coated	36	Unconfined	6.50
Beam #8 Coated	36	Confined	12.50
Beam #8 Uncoated	43	Unconfined	23.00
Beam #8 Uncoated	43	Confined	6.40
Beam #8 Coated	43	Unconfined	25.60
Beam #8 Coated	43	Confined	7.20*

*The tail portion of response is neglected. 1 in.=25.4 mm.

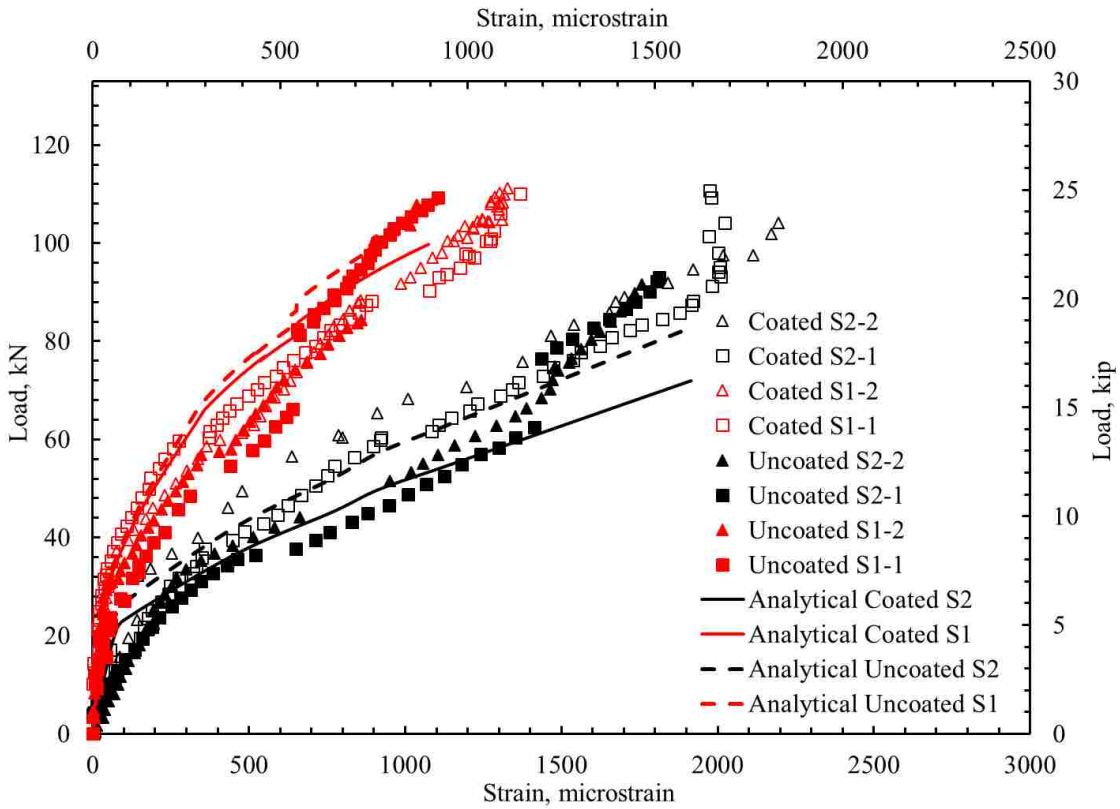

Figure 4.15. Load versus Strain Curves for Beams with 16in. Splice Length

4.4. SUMMARY

An analytical model of flexural members with lap spliced reinforcement in concrete is developed with simplified closed-form solution. Both enamel-coated and uncoated rebar were considered to reinforce normal strength concrete beams and columns. Based on the analytical results and their validation with experimental data, the following conclusions can be drawn:

(1) The analytical solutions of flexural beams and columns are in good agreement with the experimental data sets. For the reinforced concrete beams, the maximum relative errors in the prediction of maximum crack spacing and ultimate load are 5.56% and 25.6%, respectively. These results demonstrated the validity of the proposed analytical model for both symmetrical and asymmetrical lap spliced joints and for pseudo-static and cyclic loading.

(2) Both analytical and experimental results agreeably indicated that the use of enamel coating tends to slightly reduce the maximum crack spacing and notably increase the ultimate load. Therefore, the proposed analytical model explicitly taking into account the rebar-concrete interface parameters can be applied to study the effect of corrosion protective coating on the rebar-concrete bond behavior and successfully transform this effect from components to structural members or systems.

(3) The assumed sectional bond-slip distribution function is valid since it gives a close-to-test prediction of the maximum crack spacing and ultimate load of lap spliced reinforcement in normal strength concrete.

Future studies will be directed to extend the analytical model into including the effect of strain rate and investigate the dynamic performance of enamel-coated rebar in normal strength concrete.

5. EXPERIMENTAL VALIDATION OF GLOBAL BOND THEORY

5.1. INTRODUCTION

This chapter details and validates the global bond theory with flexural tests of RC beams with enamel-coated reinforcement. As described in Chapter 4, the global bond performance is significantly influenced by the local effect such as surface condition changes provided by rebar coating. Chapter 4 included a section of model validation with testing of RC members that were mainly reinforced with epoxy-coated bars and thus had lower bond strength than the RC members with uncoated steel rebar (Idun and Darwin 1999, Canbay and Frosch 2005, Treece and Jirsa 1985, Johnston and Zia 1982, Choi et al. 1990a, 1990b, Hadje-Ghaffari et al. 1994). Depending on the rebar location, a coating factor of 1.2 or 1.5 for epoxy-coated rebar was adopted in the building code (ACI 2011) and bridge specifications (AASHTO 2011). This coating factor corresponds to an average of at least 15% reduction in bond strength in comparison with uncoated rebar. The resulting increase in development length does not only increase the cost of materials, but also makes the quality control of concrete placement more challenging due to rebar congestion in areas of stress concentration.

Enamel coating has recently emerged as a viable corrosion barrier of steel rebar (Tang et al. 2012) and can be modified with chemical additives to enhance the bond strength of steel rebar in concrete. For example, calcium silicate (CS) particles taken from Portland cement were added to enamel frits and mixed with water; the enamel slurries were successfully fused on 6.35 mm-diameter steel pins at high temperature (Day et al. 2006). The CS-modified enamel coating is chemically reactive to cement. It potentially provides a smooth transition from the concrete to steel rebar in RC structures and eliminates the traditionally weak interface formed between the cement paste and the steel as water is often trapped around the steel surface during the hydration process. Yan et al. (2012) found that a mixture of 50% CS particles and 50% commercial enamel (PEMCO International) by weight, referred to as 50/50 enamel coating hereafter, gave the maximum bond strength between steel pins and mortar. Specifically, the 50/50 coating

can increase the bond strength of smooth pins in mortar by over 2 times due to increased adhesion and by over 3 times due to surface roughness, totaling over 7 times.

However, the bond strength between deformed rebar and concrete in practical applications is dominated by the steel rib bearing effect on the concrete in addition to the adhesion and friction at the steel-concrete interface. Therefore, a series of experimental studies were conducted to characterize the bond strength of enamel-coated reinforcement in various applications. Specifically, a local bond study of 50/50 enamel- coated rebar embedded in concrete cylinders was recently conducted and reported (Wu et al. 2012). Overall, the bond strength of enamel-coated rebar in concrete was approximately 15% higher than that of black rebar in concrete. Forensic studies indicated that concrete debris was observed at the rib areas of steel rebar due to the increased adhesion and friction at the steel-concrete interface.

To understand how the steel-concrete bond strength of enamel-coated steel rebar is transferred from a structural component to a structural member/system, the coated and black rebar splice strengths in concrete are investigated in RC beams under 4-point loading in this study. In particular, the effects of coating, rebar size, lap splice length, transverse reinforcement, and concrete strength are evaluated. The bond behavior with enamel-coated rebar in concrete is compared with that of epoxy-coated rebar.

5.2. EXPERIMENTAL PROGRAM

The experimental program consisted of 24 beam splice specimens: 12 reinforced with enamel-coated rebar and 12 with black rebar for comparison. The specimens were designed and tested in a series of 12 identical pairs: coated versus black. All specimens contained Class B ACI / Class C AASHTO splices (ACI 2011, AASHTO 2011).

5.2.1 Materials.

5.2.1.1 Reinforcing steel. These reinforcement are from the same group of steel used in Chapter 3. The properties are described in details in Chapter 3.

5.2.1.2 Concrete. Type I Portland-cement, and 19 mm (0.75 in.) coarse limestone aggregates, and natural sands were used in this study. The constituents were mixed with water at a water-cement ratio of 0.45 with no admixtures. The 28-day compressive

strengths, determined by concrete cylinder tests, ranged from 28 MPa (4061 psi) to 38 MPa (5511 psi) as listed in Table 5.1.

5.2.2 Test Specimens. A total of 24 beams were prepared as shown in Figures 4.6 and 4.7 with long and short splice lengths, respectively. Each beam was measured at 3,353 mm (11 ft.) long, 305 mm (12 in.) wide and 457 mm (18 in.) deep. In the center 914 mm (36 in.) constant moment region of the beam, two spliced rebar were placed on the tension side under a 4-point loading system. As the first initial study on the use of enamel-coated rebar in a tension splice, a relatively wide range of splice lengths from 305 mm (12 in.) to 1,092 mm (43 in.) were designed to evaluate the stress development in the coated rebar. A minimum constant moment region equal to twice the beam height was provided to ensure a negligible effect of concentrated loads on the pure flexural behavior of the beams (Weiss et al. 1999).

All beam specimens were cast with the splice at the bottom but subsequently inverted for testing so that cracks and damage in the tension zone can be observed visually. As indicated in Figures 4.6 and 4.7, they were reinforced with Grade 420 No.19 (#6) or No.25 (#8) rebar in the longitudinal direction and Grade 280 No.10 (#3) or No.13 (#4) closed stirrups in the transverse direction. In the constant moment region, some specimens have no transverse reinforcement in order to study the lateral confinement effect on the splice behavior. Each beam specimen is identified with a series of numbers and letters as specified in Table 5.1.

Table 5.1. Splice Specimen Properties and Test Results

Series	Notation	d_b mm	d_s mm	c^*/d_b	f_c MPa	l_s mm	P_u kN	Mu kN-m	Δ_0 mm	f_s MPa	u_{test} MPa	$u_{test,m}$ MPa	Bond Ratio	Failure† Mode
A	6C12N	19.05	N/A	1.5	27.58	304.8	104.0	95.1	5.8	341.0	5.33	5.49	1.16	S
	6B12N	19.05	N/A	1.5	31.03	304.8	92.83	84.9	5.0	303.5	4.74	4.74		S
B	6C12T	19.05	9.525	1.5	27.58	304.8	125.1	114.4	10.9	414.4	6.47	6.67	1.14	S
	6B12T	19.05	9.525	1.5	29.65	304.8	111.9	102.3	7.6	368.6	5.76	5.83		S
C	6C16N	19.05	N/A	1.5	27.58	406.4	116.1	106.2	7.6	383.4	4.49	4.63	1.44	S
	6B16N	19.05	N/A	1.5	27.58	406.4	80.96	74.0	5.1	265.7	3.11	3.21		S
D	6C16T	19.05	9.525	1.5	31.03	406.4	135.9	124.2	14.5	444.0	5.20	5.20	1.31	S
	6B16T	19.05	9.525	1.5	31.03	406.4	102.8	94.0	7.1	337.8	3.96	3.96		S
E	6C32N	19.05	N/A	1.5	27.58	812.8	142.7	130.5	11.9	468.8	2.75	2.83	1.09	Y/S
	6B32N	19.05	N/A	1.5	37.92	812.8	141.4	129.3	12.2	464.0	2.72	2.59		Y/S
F	6C32T	19.05	9.525	1.5	27.58	812.8	148.8	136.0	15.8	487.4	2.86	2.94	1.05	Y/S
	6B32T	19.05	9.525	1.5	34.47	812.8	150.4	137.5	16.8	491.3	2.88	2.80		Y/S
G	6C36N	19.05	N/A	1.5	27.58	914.4	157.1	143.7	30.5	491.3	2.56	2.64	1.06	Y/S
	6B36N	19.05	N/A	1.5	27.58	914.4	141.9	129.7	16.0	462.0	2.41	2.48		Y/S
H	6C36T	19.05	9.525	1.5	27.58	914.4	171.0	156.3	27.7	491.3	2.56	2.64	1.00	Y/S
	6B36T	19.05	9.525	1.5	27.58	914.4	149.3	136.5	9.9	491.3	2.56	2.64		Y/S

*c = minimum concrete cover; Notation: #L##L; # = rebar size (6 and 8 for 19 mm and 25 mm in diameter); L = C for enamel-coated rebar and L = B for black rebar; ## = splice length (12, 16, 32, and 36 for 305 mm, 406 mm, 813 mm, and 914 mm in length); L = N for no transverse reinforcement and L = T for transverse reinforcement provided. † Failure Mode: S-Splitting prior to Yielding; Y/S-Yielding prior to Splitting.

Table 5.1. Splice Specimen Properties and Test Results (Continued)

Series	Notation	d_b mm	d_s mm	c^*/d_b	f_c MPa	l_s mm	P_u kN	Mu kN-m	Δ_0 mm	f_s MPa	u_{test} MPa	$u_{test,m}$ MPa	Bond Ratio	Failure Mode
I	8C36N	25.4	N/A	1.25	27.58	914.4	247.3	226.2	20.1	480.2	3.33	3.43	1.35	S
	8B36N	25.4	N/A	1.25	31.03	914.4	186.6	170.6	7.1	365.4	2.54	2.54		S
J	8C36T	25.4	12.7	1.25	31.03	914.4	263.8	241.2	9.9	505.7	3.51	3.51	1.10	Y/S
	8B36T	25.4	12.7	1.25	37.92	914.4	250.8	229.4	11.2	482.6	3.35	3.19		S
K[+]	8C43N	25.4	N/A	1.25	27.58	1092	238.2	196.7	9.1	475.7	2.50	2.57	1.15	S
	8B43N	25.4	N/A	1.25	27.58	1092	211.9	193.7	7.1	413.7	2.18	2.25		S
L[+]	8C43T	25.4	12.7	1.25	27.58	1092	280.2	231.4	25.6	505.6	2.65	2.73	1.00	Y/S
	8B43T	25.4	12.7	1.25	27.58	1092	289.1	238.7	15.0	505.6	2.65	2.73		Y/S

*c = minimum concrete cover; Notation: #L##L; # = rebar size (6 and 8 for 19 mm and 25 mm in diameter); L = C for enamel-coated rebar and L = B for black rebar; ## = splice length (36 and 43 for 914 mm and 1092 mm in length); L = N for no transverse reinforcement and L= T for transverse reinforcement provided. [+] Bending moment was evaluated at the end of lap splices that are outside the constant moment zone. ǂ Failure Mode: S-Splitting prior to Yielding; Y/S-Yielding prior to Splitting.

5.2.3 Test Setup and Instrumentation. Each specimen was tested as shown in Figures 4.6 and 4.7 under a 4-point loading system. Two roller supports at 914 mm (36 in.) apart were centered about the mid-span of the beam. Two jacks at 2,743 mm (9 ft.) apart, also centered about the mid-span, were used to simultaneously load the beam with a controlled displacement rate of approximately 1.27 mm (0.004 in.) per minute until failure. In this way, the middle 914 mm (36 in.) of the beam was subjected to a constant moment.

Two Linear Variable Differential Transformers (LVDTs) were deployed at the two sides of each beam specimen at mid-span, and one additional LVDT was provided at each end of the beam to monitor vertical deflections during the tests. Eight strain gages (two strain gages at one location) were also installed on the two longitudinal rebar at each end of the splice length (shown in Figures 4.6 and 4.7) to monitor the change of stress in the steel reinforcement during the tests. The average readings of strain gages at two pairs of spliced rebar were used as strain response.

5.3. RESULTS AND DISCUSSION

Among the 24 beams tested, 16 specimens failed in splitting of the concrete cover prior to the yielding of steel reinforcement, and 8 specimens experienced steel yielding prior to splitting of the concrete cover. The following is a presentation of a detailed analysis of the test data.

5.3.1 Data Analysis. *Beams with Concrete Splitting Failure* - The average bond strength was calculated using Eq. (5.1) from the calculated stress in the deformed rebar at failure. The reinforcement stress was determined from the measured strain using the stress-strain relationship of the rebar.

$$u_{avg} = \frac{A_s f_s}{\pi d_b l_d} = \frac{f_s d_b}{4 l_d} \tag{5.1}$$

where u_{avg} is the average bond stress along the splice length, f_s is the stress in single rebar, l_d is the splice length, A_s is the cross sectional area of rebar, and d_b is the diameter of rebar.

For a direct comparison among test specimens of various concrete strengths, the average bond strength of each test was normalized to a 28-day concrete compressive strength of 31 MPa (4,496 psi). The normalized average bond strength $u_{avg,n}$ is equal to u_{avg} multiplied by $(31/f_c')^{1/4}$ in which f_c' represents the actual compressive strength of concrete in MPa and a nominal concrete strength of 31 MPa (4,496 psi) is used in this normalization Note that the use of 1/4 power in $f_c'^{1/4}$ was based on Darwin et al. (1996).

Both the original and normalized average bond strengths are listed in Table 5.1. For each series of two beams, a bond ratio was then defined as the ratio of the normalized average bond strength of the coated reinforcement to the normalized average bond strength of the black rebar. The ultimate load (P_u) and its corresponding deflection (Δ_0) for each beam are also included in Table 5.1.

Beam with Steel Yielding prior to Concrete Splitting- For series E-H, and L, steel yielding occurred prior to splitting of the concrete cover in the splice region. The average bond strength was also calculated with Eq. (5.1).

5.3.2 Crack Pattern and Failure Details. *Beams with Concrete Splitting Failure* - Series A-D with No.19 (#6) rebar and Series I-K with No.25 (#8) rebar all failed in concrete splitting prior to yielding of the steel reinforcement. Flexural cracks were initiated at various locations along the tension side and within the constant moment region of the beams. Figures 5.1 and 5.2 show two typical crack patterns on the top/tension face of the concrete cover in the splice region of the tested beams with coated and black rebar when lateral confinement was not provided in the splice region. The number given along each crack represents the load at which the crack was extended. It can be seen from Figures 5.1 and 5.2 that the specimens with enamel-coated rebar appeared to have more transverse flexural cracks developed in the splice region but clearly delayed the formation of longitudinal splitting cracks. The beams suddenly failed immediately after the longitudinal splitting cracks appeared on the top/tension face. The failure mode included concrete splitting both on the top and side covers of the beam in the splice region.

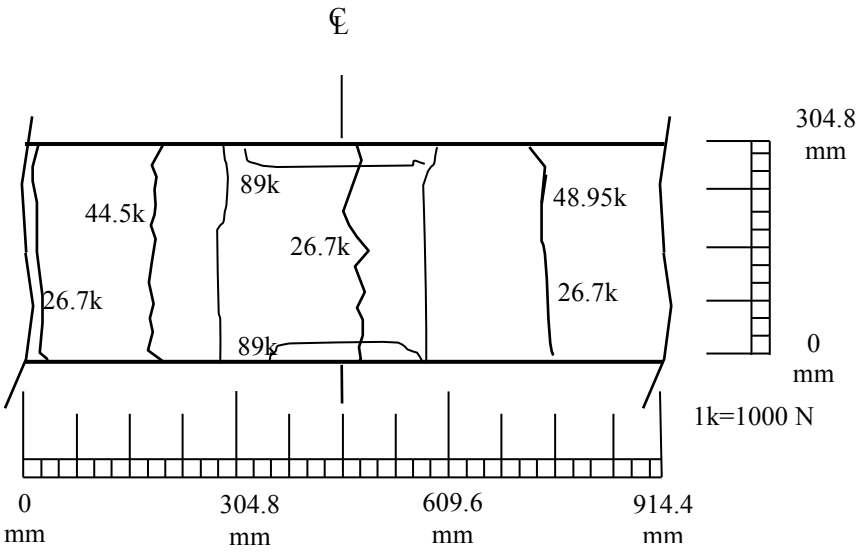

(a) 6B12N

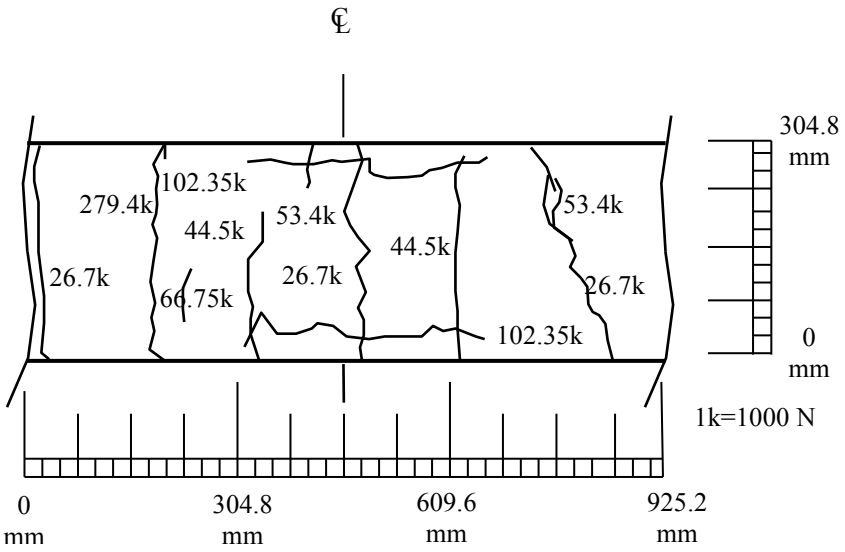

(b) 6C12N

Figure 5.1. Crack Patterns in Constant Moment Region of Series A

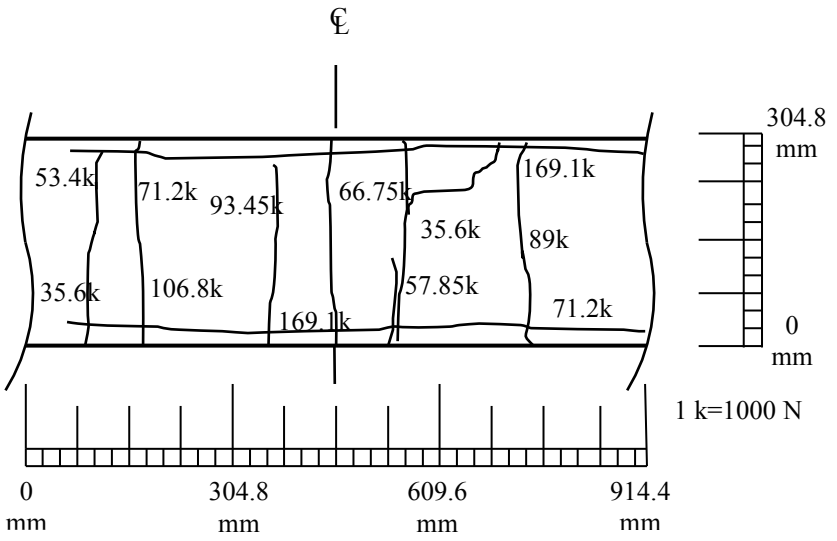

(a) 8B36N

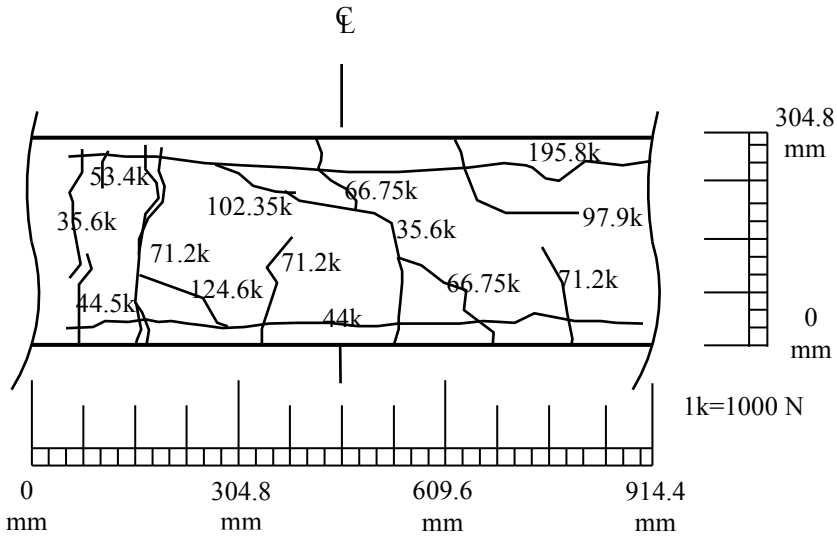

(b) 8C36N

Figure 5.2. Crack Pattern in Constant Moment Region of Series I

As the displacement increased, the concrete splitting cracks in the splice region were significantly widened and the concrete cover detached and could be easily removed without disturbing the surface condition of the rebar. For beams with enamel-coated rebar as illustrated in Figure 5.3, significant concrete residuals remained on the coating surface over the splice length, indicating a significant chemical adhesion between the coating and

concrete. Concrete crushing was also evident in the vicinity of rebar ribs, which indicated that the specimen failed in Mode 2 splitting (Cairns and Abdullah 1979). On the contrary, for beams reinforced with black rebar as shown in Figure 5.4, concrete residuals were present only at the rib-front areas due to steel bearing on the concrete.

Figure 5.3. View of Enamel Coated Rebar in Splice Region of Beam 6C32N

Figure 5.4. View of Black Rebar in Splice Region of Beam 6B32N

Beams with Steel Yielding prior to Concrete Splitting - Series E-H with No.19 (#6) rebar and series L with No.25 (#8) rebar experienced limited steel yielding before the concrete cover split on the top and side faces of the beams. Like the previous series of specimens that failed in concrete splitting, flexural cracks were initiated in the splice region; both local concrete crushing at the rib-front area of black rebar and strong adhesion between the enamel-coated rebar and concrete were observed. However, the beams with black rebar had fewer transverse flexural cracks in comparison with the previous series.

Overall, the beam specimens with coated rebar appeared to have a greater number of flexural cracks than those with black rebar. This observation indicated that the enamel-coated rebar can transfer stress more effectively due to a stronger steel-concrete bond. However, most flexural cracks of the two specimens with and without enamel coating occurred at similar locations of rebar termination.

5.3.3 Load-Deflection and Load-Strain Curves. To evaluate the effect of the enamel coating on the beam stiffness associated with the improved bond strength, the load-deflection and load-strain curves were compared in Figures 5.5 to 5.10 for six pairs of representative beams. Overall, no significant difference in stiffness was observed before and after the ultimate load. This observation differed from the conclusion that enamel coating increased the pre-peak stiffness of pin-mortar specimens as a result of their improved bonding. Adhesion between the enamel coating and cement was dominant in pin-mortar specimens but relatively small in rebar-concrete specimens due to the significant bearing effect of rebar deformation on concrete.

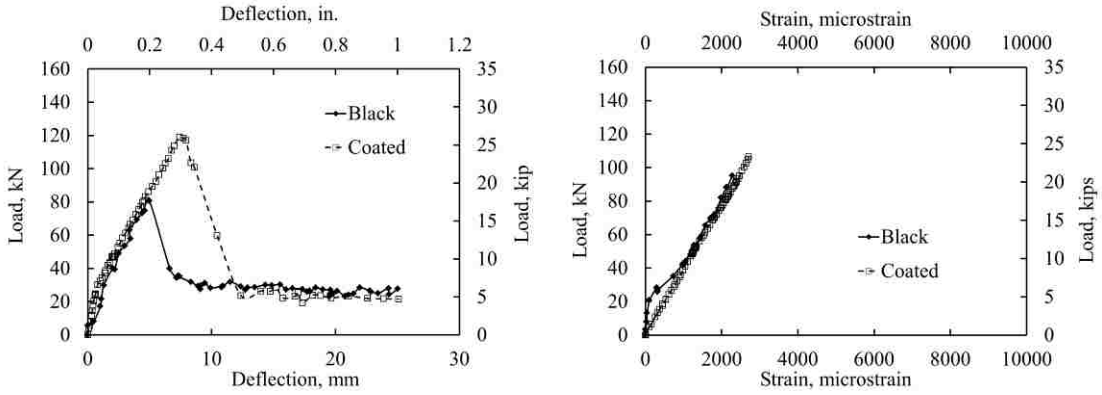

(a) Load-deflection curve (b) Load-strain curve

Figure 5.5. Load-Deflection and Load-Strain Curves for Series C

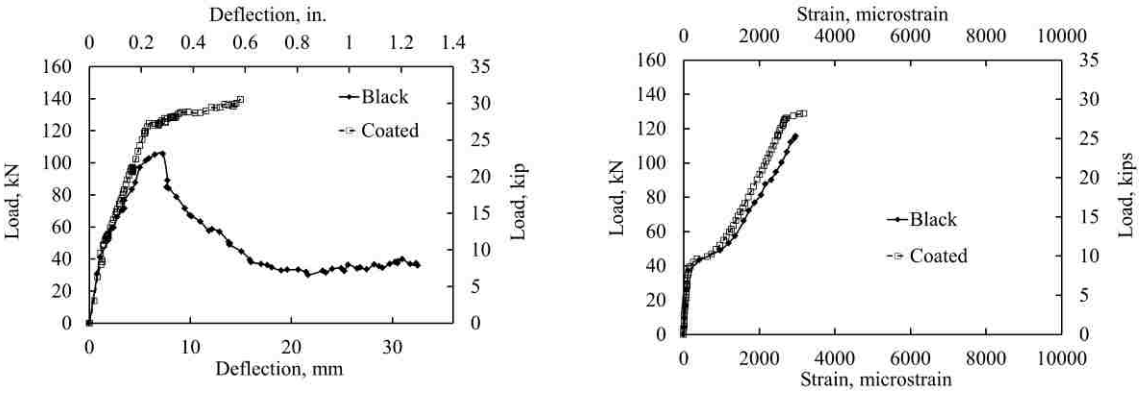

(a) Load-deflection curve (b) Load-strain curve

Figure 5.6. Load-Deflection and Load-Strain Curves for Series D

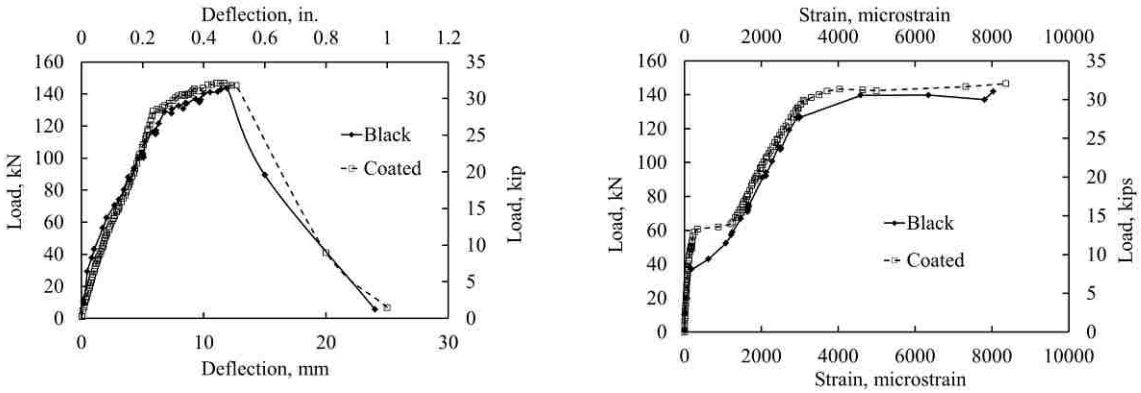

(a) Load-deflection curve (b) Load-strain curve

Figure 5.7. Load-Deflection and Load-Strain Curves for Series E

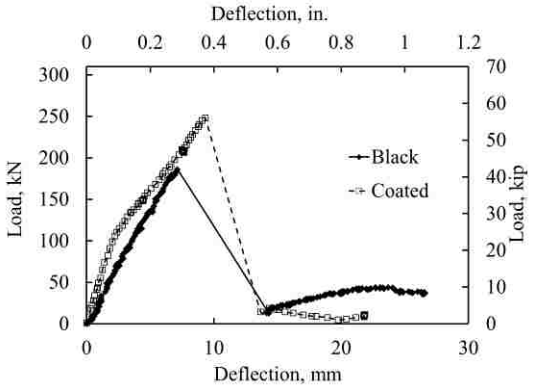

(a) Load-deflection curve

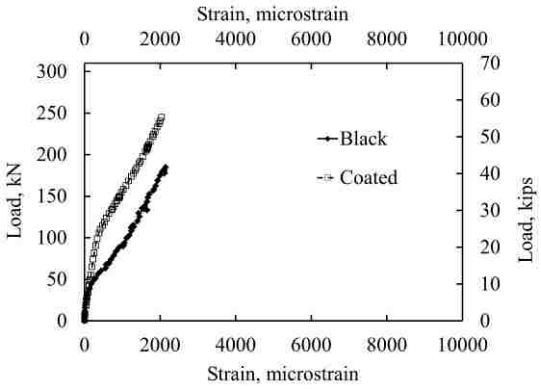

(b) Load-strain curve

Figure 5.8. Load-Deflection and Load-Strain Curves for Series I

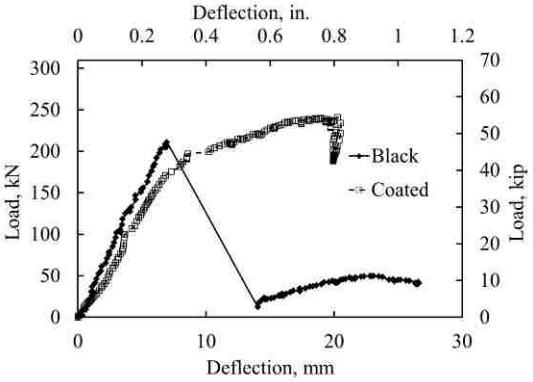

(a) Load-deflection curve

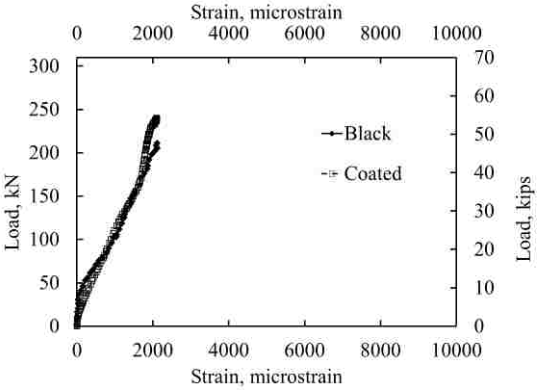

(b) Load-strain curve

Figure 5.9. Load-Deflection and Load-Strain Curves for Series K

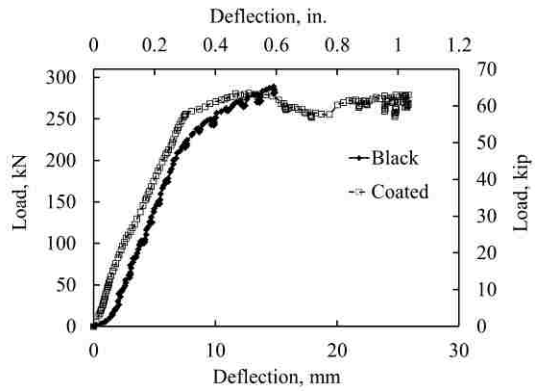

(a) Load-deflection curve

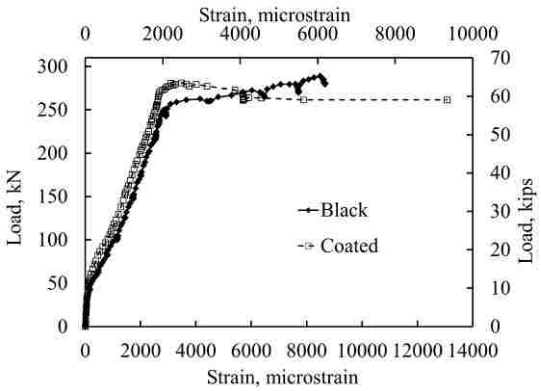

(b) Load-strain curve

Figure 5.10. Load-Deflection and Load-Strain Curves for Series L

Beams with Concrete Splitting Failure – As shown in Figures 5.5(a) and 5.8(a), when the beams were displaced gradually, the load increased linearly and rapidly at small displacement, continued to increase linearly at a reduced stiffness after concrete cracking, suddenly dropped at concrete splitting, and finally remained at a certain level mainly due to a friction effect. In comparison with the beams with black rebar, the beams with enamel-coated rebar endured larger deformation and a higher load due to the increased adhesion and friction of coated rebar in concrete. As illustrated by the load-strain curves in Figures 5.5(b) and 5.8(b), no steel yielding was observed in the steel rebar of these specimens.

Beams with Steel Yielding prior to Concrete Splitting - With sufficient splice lengths, yield strength was eventually developed in the spliced rebar, such as Series E-H, and L. As represented by Figure 5.10(a), a typical plateau was observed in the load-deflection curve. When the maximum load occurred after rebar yielding, the beams in each series had the same ultimate load resistance. The load-strain curves also confirmed yielding of the steel rebar. In these cases, the maximum strain of the beams with enamel-coated rebar is significantly larger than that with black rebar, which indicates a more effective transfer of stress from the concrete to the coated steel rebar. For beams with slightly shorter splice lengths, as illustrated in Figure 5.6(a) for Series E, a limited degree of inelastic deformation was developed after initial yielding and the effect of the coating was insignificant.

Transition in Failure Modes - As the splice length increased, more stress was transferred from the concrete to the steel rebar. At the same splice length, the stress in the coated rebar was significantly higher than that of the black rebar. For example, Figure 5.6(a) indicated that the maximum stress in the No.19 (#6) coated rebar spliced 406 mm (16 in.) in the confined beam was close to the yield strength and the load-deflection curve showed the beginning of a yielding plateau. The load-strain curves in Figure 5.6(b) confirmed the onset of initial yielding in the enamel-coated rebar. However, the stress in the corresponding No.19 (#6) black rebar was significantly lower than the yield strength, and the load-deflection curve showed a sudden drop of load as concrete splitting occurred. Therefore, the enamel coating changed the structural behavior from a brittle concrete splitting failure to a nearly ductile steel yielding failure. A similar conclusion

can be drawn for the No.25 (#8) rebar spliced 1,092 mm (43 in.) in the unconfined beams as illustrated in Figure 5.9(a, b).

5.3.4 Bond Ratio

Splice Length Effect - The bond ratio for each series of two beams in pair was calculated by dividing the ultimate bond strength of the enamel-coated rebar by that of the black rebar. As shown in Figure 5.11, the calculated bond ratios were plotted as a function of splice length over rebar diameter ratio (l_d / d_b) for different confinement conditions. It can be clearly observed from Figure 5.11 and Table 5.1 that the bond ratios for all pairs of the beams tested in this experimental program are greater than or equal to 1.0. The bond ratio first increases at short splice lengths from 1.0 to a maximum value such as 1.44, and then decreases to 1.0 when steel yielding occurs with long splice lengths. In theory, as the splice length approaches to zero, the bond strength is dominated by the strength of concrete between the two spliced rebar, becomes independent of coating conditions, and thus approaches to 1.0. As indicated in Figures 5.5, 5.6 and 5.8 for series C, D, and I beams, the maximum bond ratio corresponds to the maximum elastic stress that can be developed in the coated rebar, and lies in the range of 20 to 35 in splice length over rebar diameter ratio (l_d / d_b).

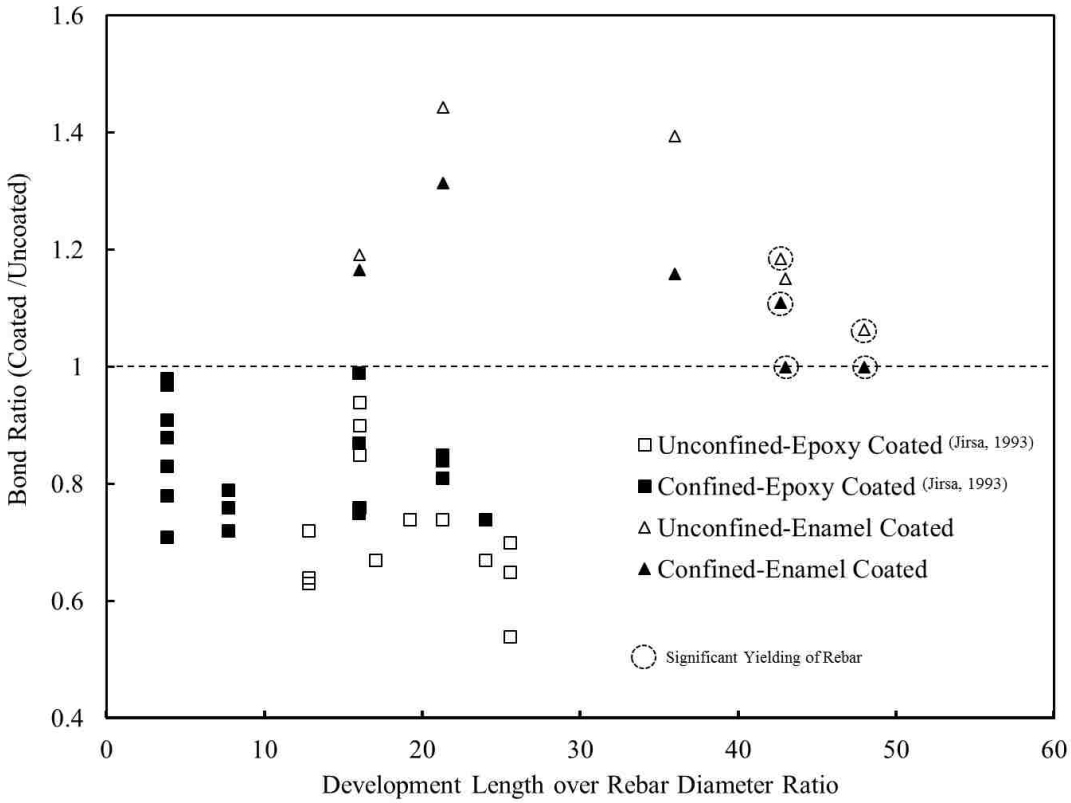

Figure 5.11. Bond Ratio Comparison between Epoxy-Coated and Enamel-Coated Rebar

Confinement Effect – As shown in Figure 5.11, beams with confined longitudinal rebar by transverse stirrups have lower bond ratios, indicating a relatively smaller coating effect of a confined splice joint. This is because confinement increases the bond strength of black rebar more rapidly than that of enamel-coated rebar. For enamel-coated rebar, an approximately 10% average increase in bond strength was observed due to confinement effect (with stirrup spacing of 100 mm or 4 in.) for Series A and B as well as for Series I and J, as shown in Table 5.1. However, as the splice length continued to increase, the stress in the spliced rebar was close to the yield strength; the effect of confinement on bond ratio gradually diminished.

Comparison with Epoxy-Coated Rebar – Figure 5.11 also compares the bond ratios for enamel-coated rebar with those of epoxy-coated rebar that were collected from the literature (Choi et al. 1999a, Hamda and Jirsa 1993, Treece and Jirsa 1989, DeVries and Moehle 1989). While enamel coating increases the bond strength of steel rebar in

concrete, the epoxy coating always reduces it. With epoxy coating, the bond ratio of deformed rebar in concrete likely starts from 1.0 at short splice lengths, reaches a minimum value, and then goes back to 1.0 as steel rebar begins yielding. Therefore, for practical designs, it is conservative to focus on the bond strength reduction of epoxy-coated rebar at l_d/d_b = 20 to 35 or the bond strength increase of enamel-coated rebar at l_d/d_b = 35 to 43, towards initial yielding of steel rebar. As such, experimental studies on RC beams with long splice lengths are crucial for enamel-coated rebar.

5.4. SUMMARY

To evaluate the bond strength of vitreous enamel-coated rebar in normal strength concrete, 24 beam splice specimens were cast and tested. Based on the experimental results, the following conclusions can be drawn:

(1) Enamel coating increases the bond strength of deformed rebar when spliced in normal strength, normal weight concrete. As the splice length increases, the ratio of bond strength between coated rebar and black rebar first increases from 1.0 to a maximum value of 1.44 and then decreases to 1.0. The maximum bond strength ratio corresponds to a splice length over rebar diameter ratio of 20 to 35 when the maximum elastic stress is developed in enamel-coated rebar. The bond strength ratio approaches 1.0 both at zero splice length and at a very long splice length since the bond strengths in the two cases are governed by concrete splitting and steel yielding, respectively.

(2) Confinement provided by transverse stirrups increases the bond strength of black rebar more rapidly than that of enamel-coated rebar. For enamel-coated rebar, an average of 10% increase in bond strength was observed due to the confinement effect obtained in this experiment for a splice length over rebar diameter ratio of less than 20. For very long splice lengths, the stress in the spliced rebar (black or coated) is equal to the yield strength and the confinement effect thus becomes negligible. Effect of different confinement level is in need for future study.

(3) The increase in bond strength due to the coating is reflected mainly in the ultimate load of the structures or beams tested in this study; it has little or no influence on the pre- and post-peak stiffness of the beams. It is unlikely that the coating alters the distribution pattern of slip between the reinforcement and concrete.

(4) The beams with coated steel rebar appear to have a greater number of smaller flexural cracks than those containing black rebar. This observation indicated that the enamel-coated rebar more effectively transfers stress from the concrete to the rebar due to a stronger steel-concrete bonding.

(5) Enamel and epoxy coatings respectively increase and reduce the bond strength of deformed rebar in concrete. For practical designs, conservative coating factors should be developed in a splice length over rebar diameter ratio of greater than 35 for enamel-coated rebar and 20 to 35 for epoxy-coated rebar. It is critical to investigate the bond strength of enamel-coated rebar in concrete with long splice lengths, corresponding to initial yielding of steel rebar.

6. DEBONDING INDUCED FRACTURE PROCESS: A MESO-SCALE PROBABILISTIC MODEL

6.1. INTRODUCTION

Splitting in concrete confinement is crucial to the bond strength of rebar in concrete. Concrete splitting and strain softening were incorporated into the unified bond theory for the determination and interpretation of the post-fracture strength of confinement materials (concrete or mortar). The proposed unified theory as discussed in Chapter 2 can thus be used to accurately evaluate the bond strength at the final failure state. To understand the bond mechanism and local bond-slip process, an in-depth study on the complete confinement splitting/fracture process is needed numerically.

Rebar debonding associated fracture of quasi-brittle materials such as concrete and mortar has been extensively studied in the past few decades. Numerous finite element models (FEMs) were proposed to reveal the complex stress field and crack propagation during the debonding process under monotonic loads. In these methods, smeared cracking model is often used to compute the confinement strength of concrete, which is difficult to capture the actual crack propagation. Instead, an average effect is estimated by smearing the discrete cracks in terms of damaging mechanism so that continuum mechanics can be applied with softened material properties.

In this chapter, the limitations of concrete smeared cracking model are first discussed through simulation results on the fracture behavior of mortar materials (similar to concrete in constituents) from pin-pull tests. A three-dimensional (3D) probabilistic model in meso scale is then proposed and implemented in ABAQUS. The numerical results are validated with experimental data from pullout test specimens.

6.2. SMEARED CRACKING SIMULATIONS OF CONCRETE

6.2.1 Meso-scale Model. Pin-pull mortar specimens (57.2 mm or 2.25 in. in diameter and 38.1mm or 1.5 in. in height) tested by Yan et al. (2012) are considered for this numerical study. The schematic elevation and cross sectional views of the specimens are presented in Figure 6.1a. The top surface of mortar is restrained from vertical movement as the steel pin/rod is pulled upwards. To improve computational efficiency,

half of a test specimen is modeled as shown in Figure 6.1b with 12,000 solid 8-node brick elements for the mortar cylinder, 600 cohesive elements for the interface layer, and 1,600 solid 8-node brick elements for the steel pin/rod. The average size of the 8-node mortar elements is 0.5 mm (0.02 in.), which is comparable to the diameter of natural sand particles. The average material properties of steel, mortar, and enamel coating are considered.

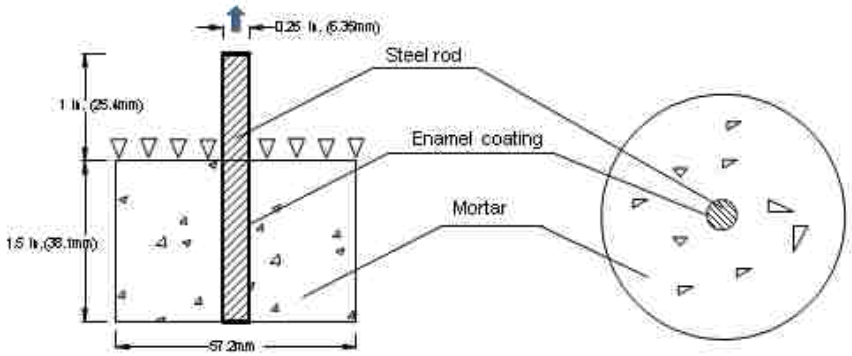

(a) Test setup

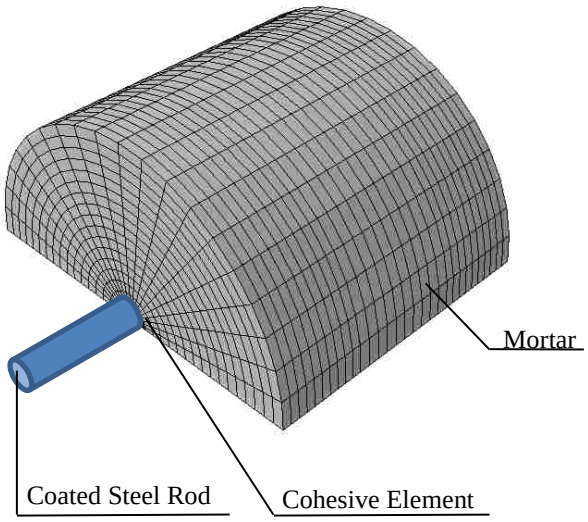

(b) Numerical model

Figure 6.1. Meso-scale Model for Pin-Pull Specimens

6.2.2 Concrete Cracks Treatment. One of the most popular crack models for quasi-brittle materials is to smear the discrete cracks over an area of interest like a

softening elastic medium. The smeared model computes the material stiffness at each integration point of the meso-scale elements. The individual macro cracks are not tracked throughout the fracturing process. Instead, the strain in mortar is decomposed into elastic and plastic components upon the detection of cracks. The strain softening materials are then considered after the crack detection. Based on the stress and corresponding plastic strain, the damage can be evaluated according to the stress state at the integration points.

The material anisotropy caused by mortar cracks is considered in the smeared model through different damage distributions in various directions based on the crack plane. The effective material stiffness and other parameters of the smeared model can be theoretically derived as found in Hillerborg's work in 1976.

The meso-scale model of each mortar specimen with the concrete smeared model was implemented on commercial software ABAQUS®. The mean compressive and tensile strengths of 25 MPa (3,600 psi) and 3.5 MPa (507 psi) were used for mortar at 28 days of curing. The Young's modulus values of 19 GPa and 25 GPa (2,755 ksi and 3,625 ksi) were used as the mean value of mortar at 14 and 28 days of curing, respectively. The shear stiffness of the interface layer was given as 0.1479 MPa (21.45 psi) for splitting failure. The coefficient of friction was set to be 0.53 for enamel coated steel based on the test results. These properties were uniformly distributed in each specimen.

6.2.3 Limitations of Smeared Cracking Representation. The stress state of the pin-pull mortar specimen with the smeared cracking model was calculated at the point where radial cracks reached a critical length beyond which the radial cracks will suddenly penetrate through concrete confinement and lead to splitting failure (Tepfers 1979). Corresponding to the critical crack length, the damage indices both at the cross section (bottom face in Figure 6.1a) and the middle section are plotted in Figures 6.2a and 6.2b. As indicated by Figure 6.2, no sudden change in damage extent can be visually identified in the cross sectional view. The discrete radial cracks often observed from experiments cannot be captured by the smeared model. The "cracked" areas appear continuous near the pullout end, which is not a good representation of actual "splitting" behavior. The radial crack front as shown in Figure 6.2(c) seems in a plane, indicating an average growth of radial cracks without taking into account the effect of cement-sands bond. Figure 6.2(d) shows the local damage due to compression near the interface, which is

limited at the pull end and inconsistent with experimental findings.

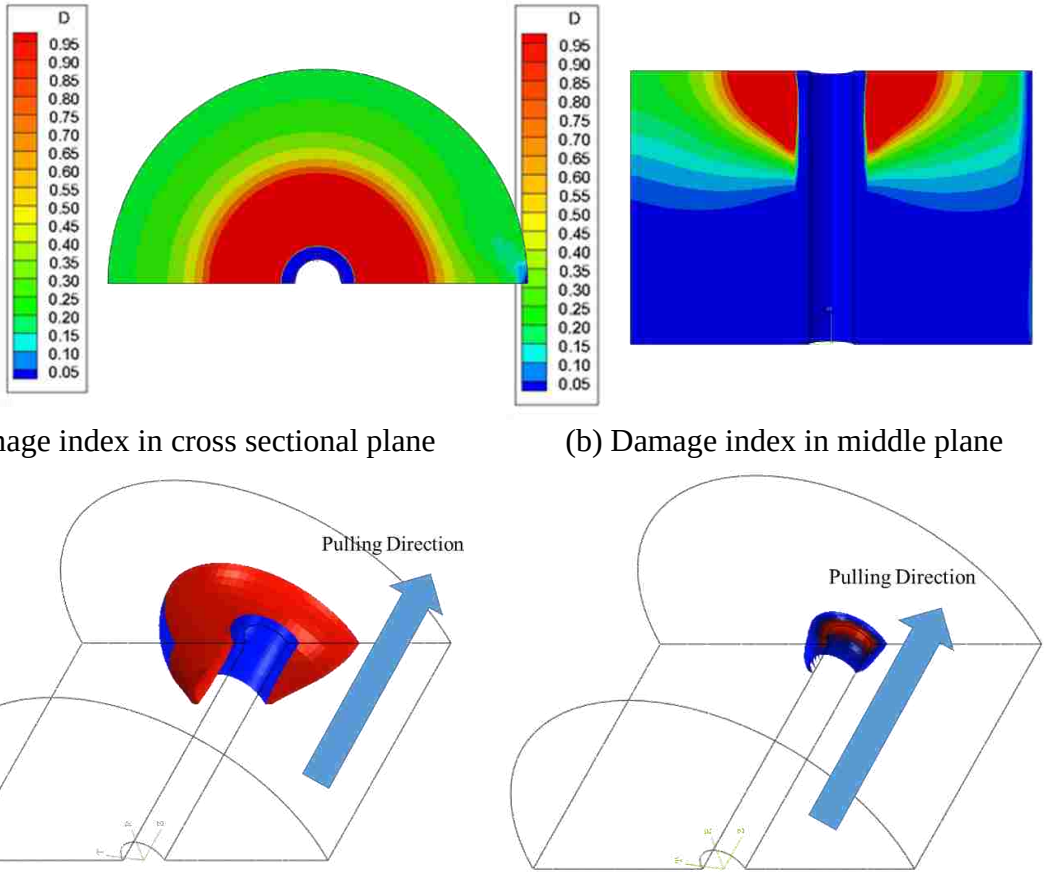

(a) Damage index in cross sectional plane (b) Damage index in middle plane

(c) Crack front surface (d) Local compression damage

Figure 6.2. Numerical Results from the Smeared Cracking Model

The discrepancies between the numerical results and the experimental observations can be further seen from the bond stress versus slip curves in Figure 6.3. The overall bond strength is over-estimated due to the uniform distribution of materials and load-induced damage in the smeared model. The lower limit on the mortar splitting strength from the experiment is most likely attributed to the overall effect of mortar mix design variations and the spatial distribution effect of material properties so that the bond strength corresponds to the weakest link in the specimen.

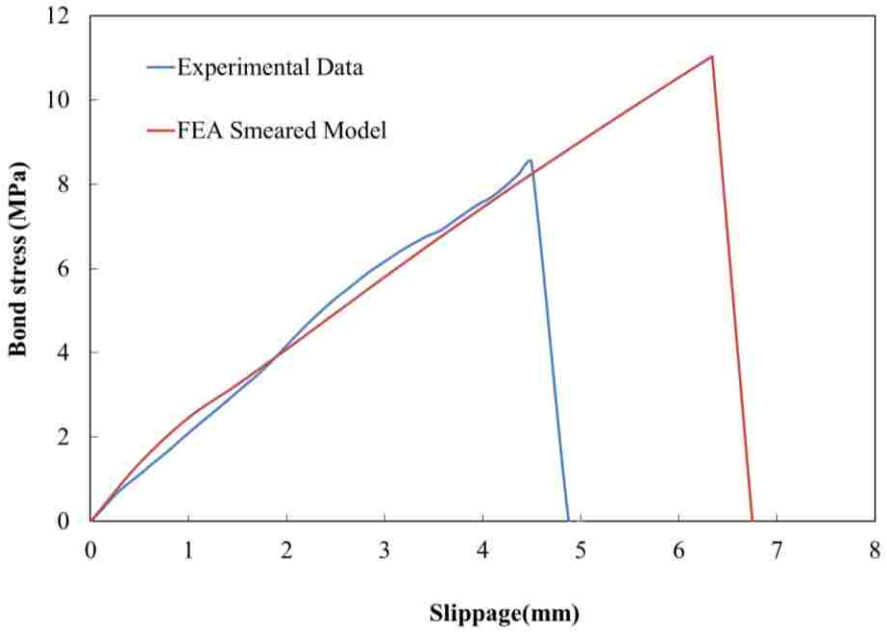

Figure 6.3. Comparison of Numerical and Experimental Bond Stresses

6.3. THREE DIMENSIONAL PROBABILISTIC SIMULATIONS

A 3D FEM of pin-pullout specimens with randomly distributed properties of heterogeneous mortar materials is proposed and developed. The same meso-scale finite elements as presented in Figure 6.1a are adopted here. In this new model, however, the bond between the coated pin and mortar is simulated using the damage-based cohesive element that is defined by the fracture property of the pin-enamel-mortar interface layer (shear stiffness). A Mohr-Coulomb failure criterion is used and the residual strength attributed to post-splitting friction of mortar is considered after debonding has occurred. As a result, the stress-strain relation of the interface layer is linear before the peak bond stress has been reached.

Both direct and indirect approaches can be taken to simulate the heterogeneity of quasi-brittle materials. In the direct approach, geometrical properties, locations, and material properties are explicitly assigned to all elements that represent various stages of loading. In the indirect approach, the spatial distribution of material properties is randomly generated to represent the material heterogeneity as detailed in Figure 6.4a. One of the most commonly used probability distribution functions in the indirect

approach is the Weibull distribution. However, the application of Weibull distribution requires that the size of the representative volume element be much smaller than the size of material aggregates (Bazant et al. 2007). Therefore, meso-scale (e.g. mm in length scale) elements are used to simulate the random field of fracture properties using the Weibull distribution as exemplified in Figure 6.4b. The nonlinear fracture process of the heterogeneous quasi-brittle materials can then be treated as an overall behavior of an assembly of the meso-scale elements with linear material properties to failure and randomly assigned material properties (Romstad et al. 1974). Some of the aggregate interlocking behaviors are simulated through classic contact mechanics proposed by Jonhson (1985).

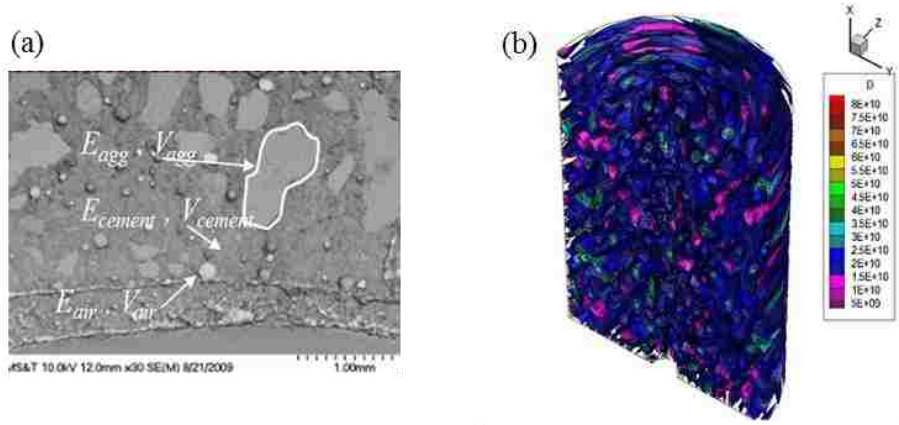

(a) SEM image for material constituents (b) Mortar with randomly distributed properties

Figure 6.4. Mortar Constituents and Meso-Scale Model:

The 3D probabilistic damage model in meso scale, presented in this study, represents the first extension of two dimensional meso-scale concrete models developed by Tang et al. (2003) and Zhu et al. (2004). In the proposed 3D model, the concrete and mortar heterogeneities are described by the Weibull distribution function of material properties. An equivalent principle strain is introduced and applied as the damage criterion for various mortar splitting associated failure modes of finite elements. Both the

bond stress versus displacement curves and the failure patterns are compared with their corresponding experimental results.

6.3.1 Probabilistic Model of Material Properties. The classical Weibull probability density function used to simulate the random property of materials can be written as follows,

$$f(x) = \frac{\beta x^{\beta-1}}{u_0^{\beta}} e^{-\frac{x^{\beta}}{u_0^{\beta}}} \tag{6.1}$$

where x is a random variable that represents the fracture property of meso-scale elements, β is a parameter that describes the shape of the density function as illustrated in Figure 6.5a, and u_0 represents a mean-value related parameter that also influences the shape of the density function as shown in Figure 6.5b. As β increases, the density function becomes narrower and sharper. The mean value of the random variable can be obtained by

$$E(x) = \int_{-\infty}^{+\infty} x f(x) dx = u_0 \Gamma(1+\beta^{-1}) \tag{6.2}$$

where $\Gamma(.)$ represents a Gamma function of the argument in the bracket. As β increases to infinity, the Gamma function approaches to a unit value and u_0 approaches to the mean value of the random variable.

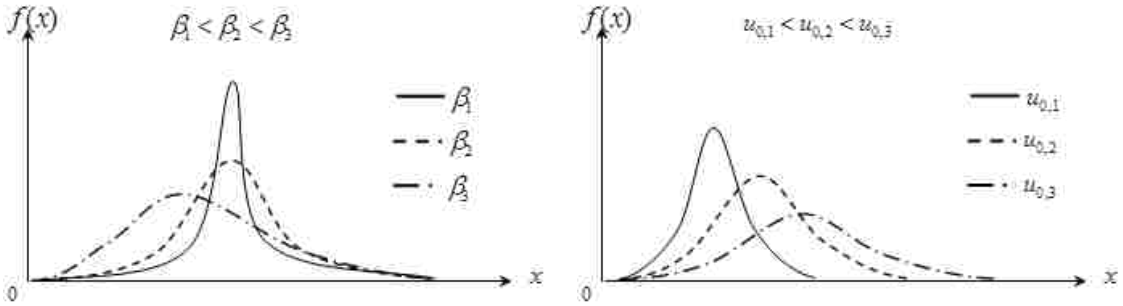

(a) Influence of β (b) Influence of u_0

Figure 6.5. Characteristics of Weibull Probability Density Function

In the proposed model, it was assumed that the uniaxial compressive/tensile strength, Poisson's ratio, and the modulus of elasticity all follow the Weibull distribution with different β values. Samples of the heterogeneous material properties were taken from the random distribution at the beginning of computation. Deterministic analysis was then followed up.

6.3.2 Fracture Behavior of Mortar. A piecewise linear stress-strain relationship to failure is applied to each element of mortar. To account for various types of failure modes, different damage processes are assigned to compression and tension regions of the elements in principal stress space. The coupling of damage along different principal axles is taken into account through the introduction of an equivalent uniaxial strain.

6.3.2.1 Tension. The stress-strain relationship in the proposed tension fracture model is presented in Figure 6.6a. The damage factor D_t can be represented by the strain of a mortar element:

$$D_t = \begin{cases} 0 & \varepsilon_t < \varepsilon_{t0} \\ 1 - \dfrac{\eta - \lambda}{\eta - 1}\dfrac{\varepsilon_{t0}}{\varepsilon_t} + \dfrac{1-\lambda}{\eta - 1} & \varepsilon_t < \varepsilon_{t0} \\ 1 - \lambda\dfrac{\varepsilon_{t0}}{\varepsilon_t} & \varepsilon_{tr} < \varepsilon_t < \varepsilon_{t0} \\ r_t & \varepsilon_t > \varepsilon_{tu} \end{cases} \tag{6.3}$$

where ε_t is the effective tensile strain to account for the 3D stress state effect, ε_{t0} is the strain corresponding to the tensile strength of mortar f_{t0}, $\varepsilon_{tr} = \eta\varepsilon_{t0}$ represents a residual strain corresponding to the residual tensile strength of the mortar f_{tr}, η $(1 < \eta < 5)$ is an index of the residual strain, $\lambda = f_{tr} / f_{t0}$ is the ratio between the residual strength and the tensile strength, ε_{tu} is the maximum tensile strain when the element no longer carries any load, $\xi = \varepsilon_{tu} / \varepsilon_{t0}$ ξ $(> \eta)$ represents the ratio between the maximum strain and the strain at the tensile strength, and r_t is a total damage factor. Therefore, the secant modulus of elasticity of the damage element E can be related to the original modulus E_0 by the damage factor D_t

$$E = E_0(1 - D_t) \tag{6.4}$$

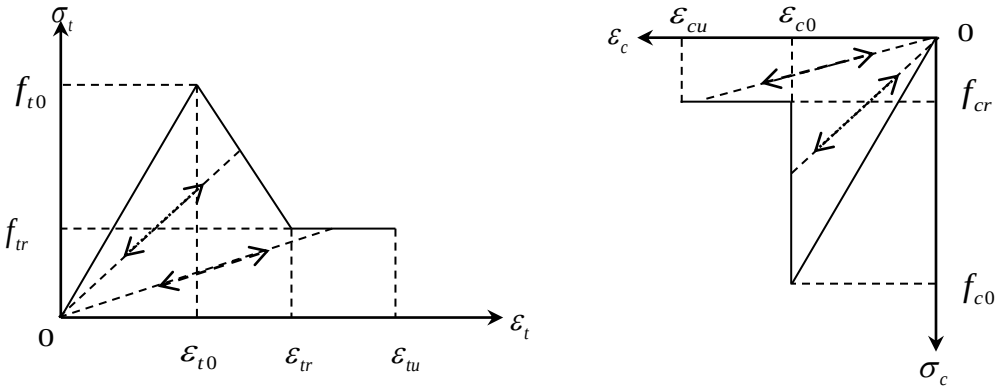

(a) Tension (b) Compression

Figure 6.6. Constitutive Law for Meso-scale Elements

6.3.2.2 Compression. Under compressive loads, the constitutive law of mortar is presented in Figure 6.6b. In this case, the damage factor D_c can be evaluated by:

$$D_c = \begin{cases} 0 & \varepsilon_c < \varepsilon_{c0} \\ 0 & \varepsilon_{c0} < \varepsilon_c < \varepsilon_{cu} \\ r_c & \varepsilon_{c0} < \varepsilon_c < \varepsilon_{cu} \end{cases} \tag{6.5}$$

where ε_c is the effective compressive strain to account for the 3D stress state effect, ε_{c0} is the strain corresponding to the compressive strength of mortar f_{c0}, ε_{cu} (0.0035 in this study) is the ultimate strain beyond which the element can no longer bear any loading, and f_{cr} in Figure 6.6b represents the residual strength in compression.

6.3.2.3 Effective Stress and Strain Considering Poisson Effect. Based on their principal stresses, the overall stress condition for a 3D mortar element can be categorized into four types: Tension-Tension-Tension (TTT), Tension-Tension-Compression (TTC), Tension-Compression-Compression (TCC), and Compression-Compression-Compression (CCC). Depending on the ratio of their principal stresses, the mortar element can experience a tensile fracture failure (I), a cylindrical compression failure (II), a layered splitting failure (III), an inclined shear failure (IV), or a J2 flow failure by crushing (V). These failure modes are visually illustrated in Figure 6.7.

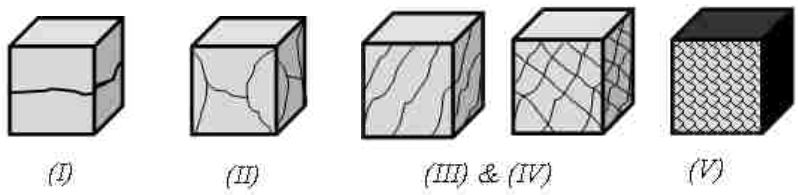

Figure 6.7. Fracture Patterns under Different Stress Conditions

To describe the five types of damage states, the overall failure of the mortar element in meso scale can be described by equivalent uniaxial-tension and uniaxial-compression failures. In this case, the effect of secondary principal stresses is added to that of the dominant principal stress, simply following the general Hooke's law and the Poisson effect.

$$\overline{\sigma_1} = E\overline{\varepsilon_1},\ \overline{\varepsilon_1} = \varepsilon_1 + \frac{\nu}{E}(\sigma_2 + \sigma_3) \tag{6.6}$$

$$\overline{\sigma_3} = E\overline{\varepsilon_3},\ \overline{\varepsilon_3} = \varepsilon_3 + \frac{\nu}{E}(\sigma_1 + \sigma_2) \tag{6.7}$$

where σ_1, σ_2, and σ_3 are the principal stresses; ε_1, ε_2, and ε_3 are the principal strains; $\overline{\sigma_1}$ and $\overline{\sigma_3}$ are the equivalent principal stresses; $\overline{\varepsilon_1}$ and $\overline{\varepsilon_3}$ are the equivalent principal strains.

6.3.3 Characteristics of Interface Layer. The interface layer is simulated with a series of cohesive elements whose behaviors are governed by a contact algorithm in bonding, debonding, and post-debonding stages during pull-out tests. The cohesive elements are selected to represent the fracture process of the interface between a steel pin and mortar. They are subjected to a combined effect of normal and shear forces. The maximum strain and the Mohr-Coulomb stress are two major failure evaluation criteria (Chen and Saleeb 1982). The maximum strain of a damaged element is equivalent to that caused by the effective stress of its corresponding undamaged element (Lemaitre 1985). The maximum strain criterion, however, plays a more important role in the understanding of quasi-brittle material behaviors. Once the maximum strain is reached, damage initiates regardless of the Mohr-Coulomb stress criterion. However, if the stress reaches its maximum according to the Mohr-Coulomb criterion, damage initiates.

6.3.3.1 Effect of a single stress component. For a pure shear-mode fracture, the chemical adhesive force and static frictional force dominate the interface behavior prior to the peak stress, which is represented by a linear ascending stage in the bond stress-slip relationship as shown in Figure 6.8a. After the peak stress, the decrease in bond stress depends upon the level of damage in cohesive elements, which gradually transfers from the elastic behavior to the Mohr-Coulomb friction failure of the cohesive elements. In this case, the residual bond stress mainly comes from the dynamic friction force that is neglected in this study. Note that δ_{s0} in Figure 6.8a represents the slip at the maximum shear stress τ_{s0}, and δ_{su} is the maximum slip that the cohesive elements can endure in the shear mode.

For a pure tension-mode fracture, the stress increases linearly with slip prior to the peak stress and drops to near-zero strength as indicated in the stress-slip relationship in Figure 6.8b. Note that δ_{n0} in Figure 6.8b represents the slip at the maximum normal stress σ_{n0}, and δ_{nu} is the maximum slip that the cohesive elements can endure in the normal mode.

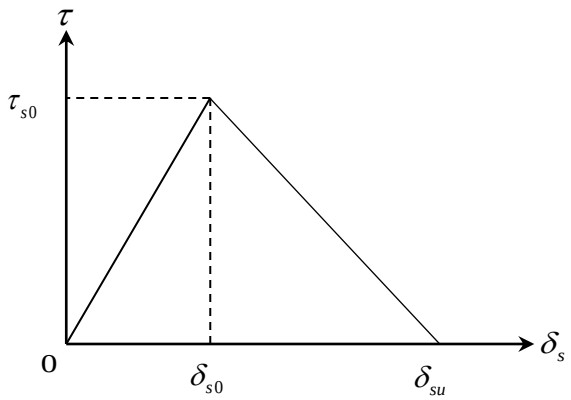

(a) Pure shear mode

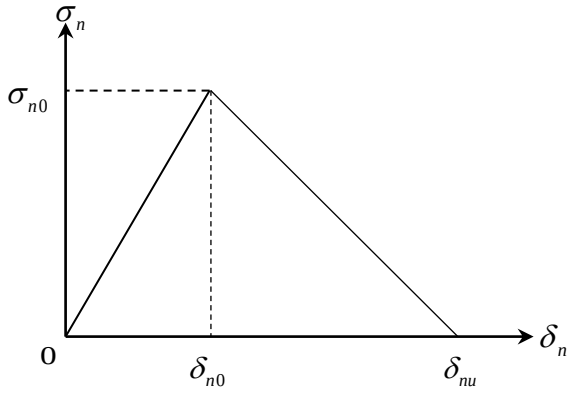

(b) Pure tension mode

Figure 6.8. Stress-slip Relationships for Cohesive Elements

6.3.3.2 Cohesive elements. The fracture failure of cohesive elements is often caused by the combined effect of shear and normal modes. To illustrate various failure modes, a stress vector on the interface as illustrated in Figure 6.9 can be decomposed into two components: one normal stress σ_n and one total shear stress τ_s. The total shear can further be decomposed into two shear components τ_{s1} and τ_{s2}. The failure mode index ϕ_{sn} due to the normal and total shear components and the failure mode index ϕ_{ss} due to the two shear components are defined by

$$\begin{cases} \phi_{sn} = (\frac{2}{\pi}) \tan^{-1}(\frac{\tau_s}{\sigma_n}) \\ \phi_{ss} = (\frac{2}{\pi}) \tan^{-1}(\frac{\tau_{s2}}{\tau_{s1}}) \end{cases} \tag{6.8}$$

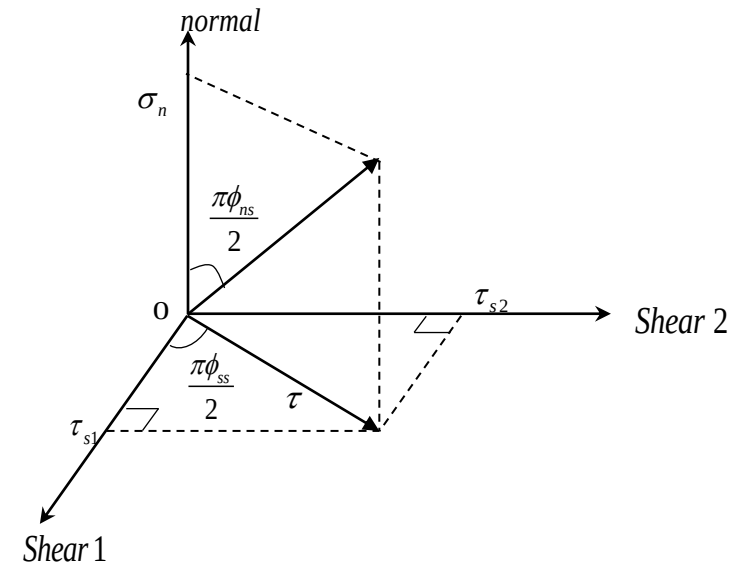

Figure 6.9. A General Stress Vector on the Interface

When $\phi_{sn} = 0$, the interface element is subjected to normal stress effect. When $\phi_{sn} = 1$, the element is subjected to shear stress effect. In either case, the damage factor D_n due to normal stress effect and the damage factor D_s due to shear stress effect can be evaluated by:

$$D_n (or\ D_s) = \frac{\delta_m (\delta_{mu} - \delta_{m0})}{\delta_{mu} (\delta_m - \delta_{m0})} \tag{6.9}$$

$$\delta_m = \sqrt{\delta_n^2 + \delta_{s1}^2 + \delta_{s2}^2} \tag{6.10}$$

where δ_m represents the total effective slip, δ_n is the slip along the normal direction, δ_{s1} and δ_{s2} are the slips along the directions of the two shear stress components, and δ_{m0} and δ_{mu} respectively denotes the slip corresponding to the maximum elastic stress and the maximum slip beyond which the element can no longer carry loading. The subscript *m* in

Eq. (6.9) and Eq. (6.10) signifies the mixed mode of stress effect. The stress for both normal and shear fracture modes prior to the softening of an interface element can be expressed as a linear function of its respective displacement:

$$\sigma_n = k_n \delta_n, \quad \tau_s = k_s \delta_s \tag{6.11}$$

where k_n and k_s are the normal and shear fracture stiffness coefficients, respectively, and δ_n and δ_s represent the slips resulting from the normal and shear stress effects.

The initiation of the softening process can be approximately predicated using the following quadratic failure criterion:

$$(\frac{\sigma_n}{\sigma_{n0}})^2 + (\frac{\tau_{s1}}{\tau_{s10}})^2 + (\frac{\tau_{s2}}{\tau_{s20}})^2 = 1 \tag{6.12}$$

where σ_{n0}, τ_{s10} and τ_{s20} represent the normal strength, shear strength in the direction of *s1*, and shear strength in the direction of *s2*, respectively, corresponding to the onset of strain softening. When the isotropic shear behavior is considered prior to the softening, the shear and normal stresses and their corresponding slips are related by:

$$\frac{\delta_s}{\delta_n} = \frac{\sqrt{\delta_{s1}{}^2 + \delta_{s2}{}^2}}{\delta_n} = \frac{\tau_s}{\sigma_n} = \tan(\frac{\pi\phi_{sn}}{2}) \tag{6.13}$$

in which δ_{s1} and δ_{s2} represent the slips along the directions of the two shear stress components, respectively. Therefore, the effective slip at the onset of softening due to the combined normal and shear forces or the mixed mode can be determined by:

$$\delta_{m0} = \delta_{n0}\sqrt{1 + \tan(\frac{\pi\phi_{sn}}{2})^2} \tag{6.14}$$

where δ_{n0} and δ_{m0} represent the slips corresponding to the maximum elastic normal stress and the maximum mixed-mode stress, respectively, as illustrated in Figure 6.10.

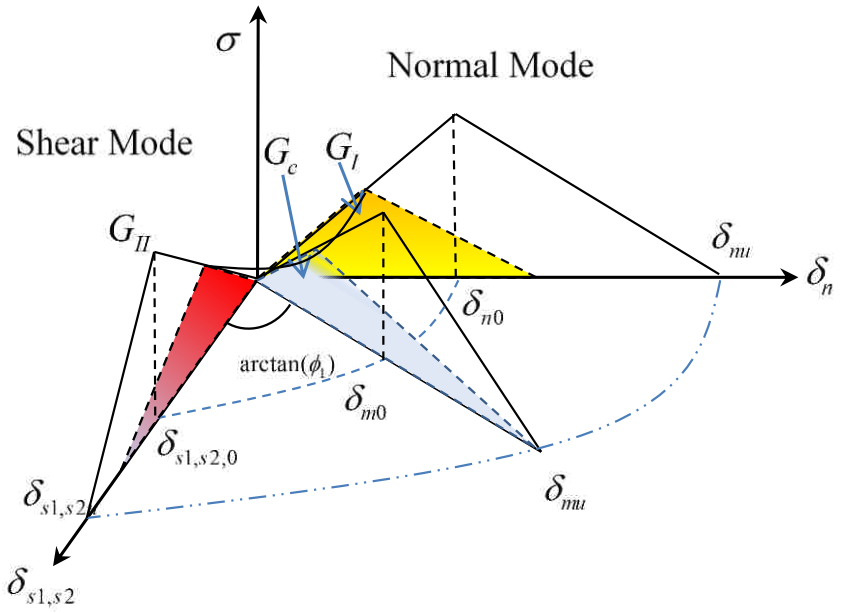

Figure 6.10. Illustration of a Mixed-Mode Fracture

In Figure 6.10, the shaded area represents the fracture energy generated by slippage, which is designated as fracture toughness by G_n , G_s , and for the normal, shear, and mixed modes, respectively. The fracture energy in the mixed mode can be related to those of the normal and shear modes by

$$G_m = G_{IC} + (G_{IIC} - G_{IC})(\frac{G_s}{G_n + G_s})^{\eta} \tag{6.15}$$

where G_{IC} and G_{IIC} are the critical fracture energy for mode I (tension) and mode II (shear), and η (=2.28) is the empirical interpolation index determined by fitting Eq. (6.15) to the experimental data.

The fracture toughness can be calculated by the area under the stress-slip curve by:

$$G_n = \int_0^{\delta_{nu}} \sigma_n d\delta_n \,,\; G_s = \int_0^{\delta_{su}} \tau_s d\delta_s \tag{6.16}$$

By combining Eq. (6.8) with Eqs. (6.10-6.15), the maximum mixed-mode slip corresponding to the complete failure can be derived and calculated by:

$$\delta_{mu} = \frac{2\sigma_{n0}}{\delta_{n0}\delta_{m0}} \left\{ G_{IC} + (G_{IIC} - G_{IC}) \left[\frac{\tan(\frac{\pi\phi_{sn}}{2})^2}{1+\tan(\frac{\pi\phi_{sn}}{2})^2} \right]^{\eta} \right\} \tag{6.17}$$

6.3.3.3 Frictional stress. The frictional mechanism for debonding between a pin and mortar involves both static and dynamic friction effects. The static friction is coupled with the chemical adhesion; it has been taken into account in the cohesive elements discussed in Section 6.3.3.2. The dynamic friction is modeled as an additional inelastic stress; it is added to the shear stress at the interface. In this case, the total shear effect can be expressed into:

$$\tau_{total} = \tau_s + \sigma_n \mu_0 \tag{6.18}$$

where μ_0 is the dynamic coefficient of friction. It is noted that the dynamic friction is activated immediately after the onset of damage in cohesive elements (controlled by δ_{m0}), and coupled with the damage of the cohesive elements due to other loading effects.

6.4. SIMULATION RESULTS AND DISCUSSION

6.4.1 Parameters and Failure Modes. The finite element analysis (FEA) of the meso-scale model with randomly distributed material properties was conducted on the ABAQUS® software platform. The contact algorithm for cohesive elements and the equation solver in ABAQUS® were directly used in parallel computations. However, the generation of a random field, the meso-scale fracture, and the cohesive element subroutines were coded separately in Fortran 77 for this study. The Newton-Raphson iterative scheme was applied with a time step time of 10^{-5} sec to meet the accuracy and convergence requirements. The model and analysis flow chart is presented in Figure 6.11.

Mean compressive and tensile strengths of 25 MPa (3,600 psi) and 3.5 MPa (507 psi) were used for mortar after 28 days of curing. At 14 days of curing, the mean compressive and tensile strengths of mortar were assumed to be 18.75 MPa (2,700 psi) and 1.6 MPa (230 psi), respectively. The Young's modulus values of 19 GPa and 25 GPa (2,755 ksi and 3,625 ksi) were used as the mean values for mortar at 14 and 28 days of curing, respectively. The shear stiffness values of the interface layer were given as 0.1479 MPa (21.45 psi) and 0.045 MPa (6.5 psi) for the splitting failure and partial splitting

failure, respectively. The coefficient of friction was set to be 0.53 for enamel coated steel based on the test results. The shear stiffness for the partial splitting failure mode is much lower than that for the splitting failure mode due to different coatings and curing ages.

The three major failure types observed from the pin-pull tests are the pull-out failure, fully splitting failure, and partially splitting failure. For the pull-out failure, the "weakest link" is the debonding (or interface failure) between the pin and mortar, and the majority of the mortar cylinder remains elastic. In this case, the proposed model is not so advantageous over a conventional layer model. Therefore, the following presentation is focused on the fully and partially splitting failures.

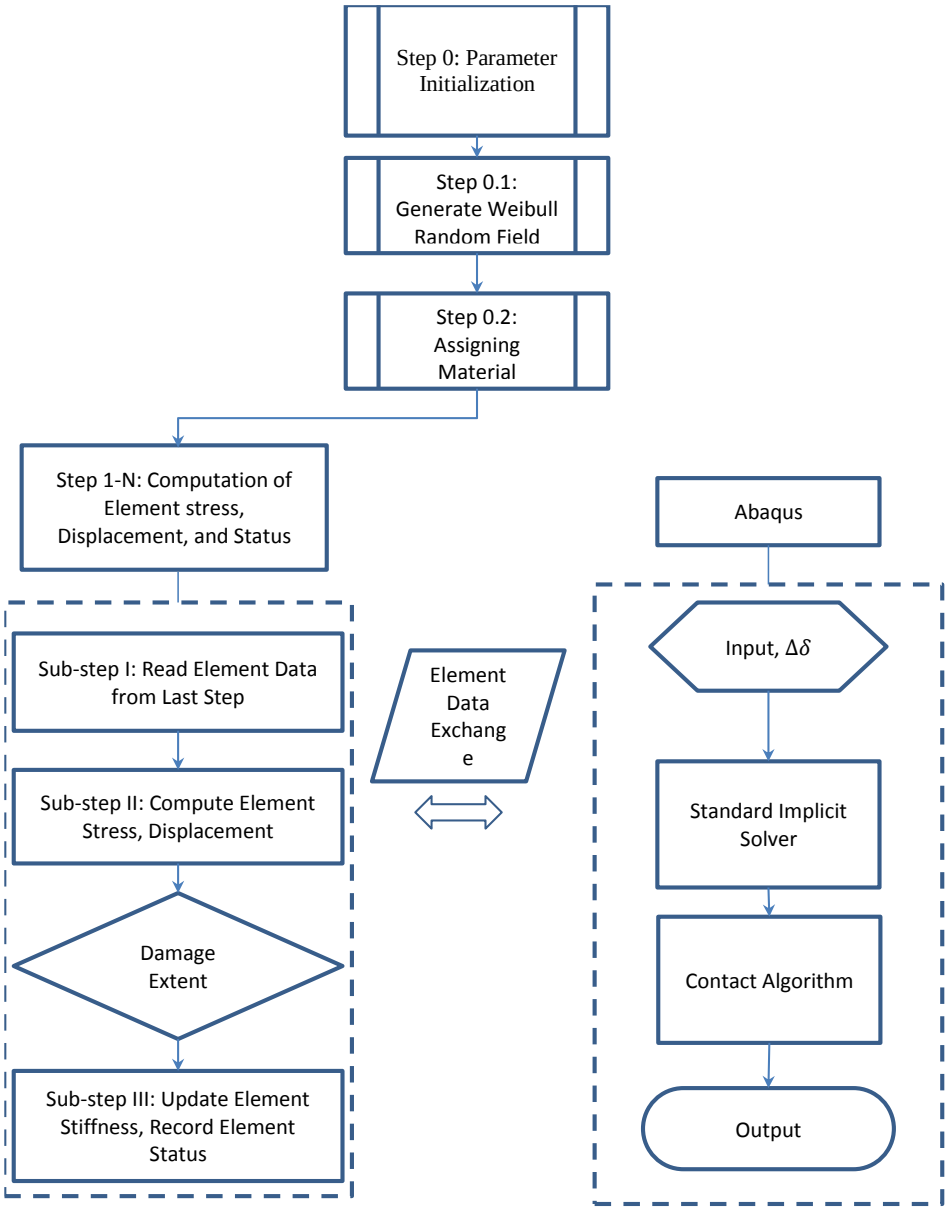

Figure 6.11. Flow Chart for the Meso-Scale Model and Analysis

6.4.2 Main Findings. Numerous specimens tested by Yan et al. (2012) were modeled with the proposed meso-scale model and good agreements were achieved between the numerical and experimental results. Following is a presentation of two representative analyses for the cases of fully and partially splitting failure modes. The fully splitting mode was observed on specimens with enamel-coated steel pins after 14 days of curing. The partially splitting failure mode was observed after 28 days of curing.

6.4.2.1 Fully splitting failure. The bond stress versus slip curve of a representative specimen with 35/65 enamel coating tested by Yan et al. (2012) is plotted in Figures 6.12. As indicated by the top cross sectional view in Figure 6.12, a radial crack penetrated through the cross section of mortar after 14 days of curing. The stress-slip curve is compared with various numerical results associated with randomly distributed properties of the analyzed specimen.

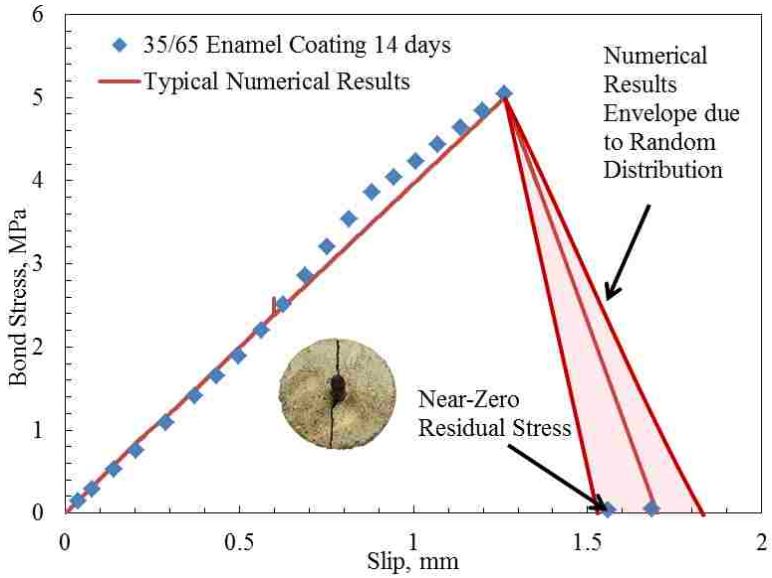

Figure 6.12. Simulated Stress-slip Curves and Their Comparison with Test Data: Fully Splitting Failure Mode

For the fully splitting failure mode, the bond force linearly increased to its peak value and suddenly dropped after the peak force or bond strength has been reached, indicating a brittle failure. In this case, the cohesive elements did not experience any damage prior to the bond strength. Therefore, the kinematic friction effect was not observed in the numerical analysis. The slopes of the load versus slip curves from various numerical analyses, both for ascending and descending segments, agreed well with the experimental results.

Figure 6.13 presents the failure mode and the extent of damage both experimentally and numerically. The stress distribution from the numerical analysis was

compared with the failure mode observed from the experiments. In reference to Section B-B in Figure 6.13, a damage zone around the pin with high stress concentration is clearly observed, corresponding to the pullout of the pin during tests. In addition, the radial stress distribution coincides with the cutting-through radial crack observed from the experiment. In reference to Section A-A in Figure 6.13, it can be seen that excessive stresses are concentrated along the pin-mortar interface. Despite the fully splitting failure, a significant number of elements along the interface area are not totally damaged, which correlates well with experimental observations since the pin was still attached to the cracked mortar. It is also found from the FEA that the simulated results are mostly sensitive to the material properties of mortar and the shear stiffness of cohesive elements.

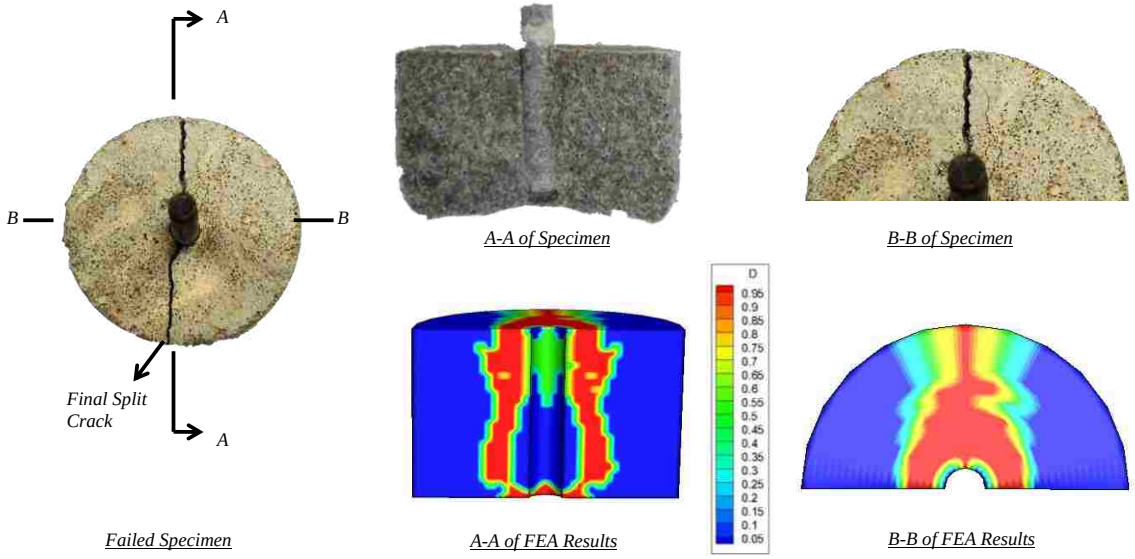

Figure 6.13. Comparison of Failure Mode and Damage Extent: Fully Splitting Failure

6.4.2.2 Partially splitting failure. The experimental bond stress versus slip of a representative specimen with 50/50 enamel coating tested by Yan et al. (2012) is presented in Figure 6.14. As indicated by the top cross sectional view in Figure 6.14, the specimen experienced a pin pullout failure mode with partial mortar splitting after 28 days of curing.

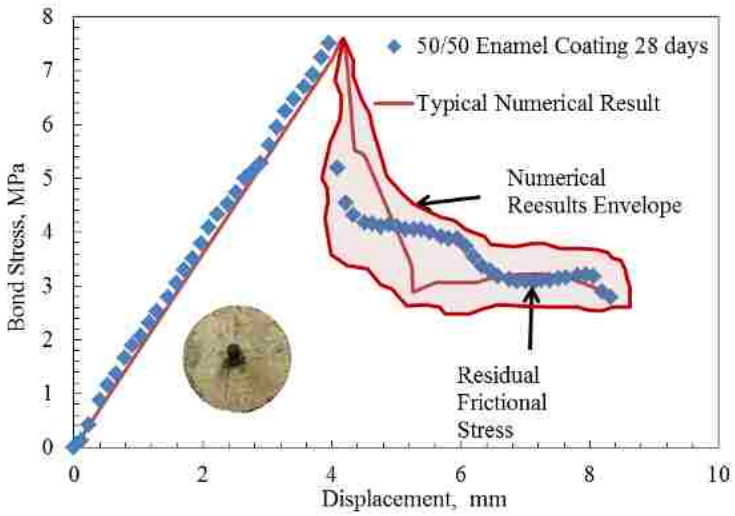

Figure 6.14. Simulated Stress-slip Curves and Their Comparison with Test Data: Partially Splitting Failure Mode

In the partial splitting failure mode, the radial crack did not penetrate through the mortar cover as the enamel-coated pin was pulled out. The bond stress linearly increased to its peak value or bond strength and gradually dropped to the residual friction induced stress. It can also be observed from Figure 6.14 that various simulations with randomly distributed properties of mortar cover the test data pretty well.

Figure 6.15 compares the experimental and numerical results in terms of failure mode and damage extent. The stress distribution patterns obtained from the FEA at Sections A-A and B-B can be well correlated to the experimental phenomena. In particular, the continuous damaged zone in the interface area is a clear indication of the local damage of the mortar cylinder in the vicinity of the pin. This demonstrated that the total separation of the pin from mortar dominates the ultimate behavior of the specimen failed in partial splitting mode.

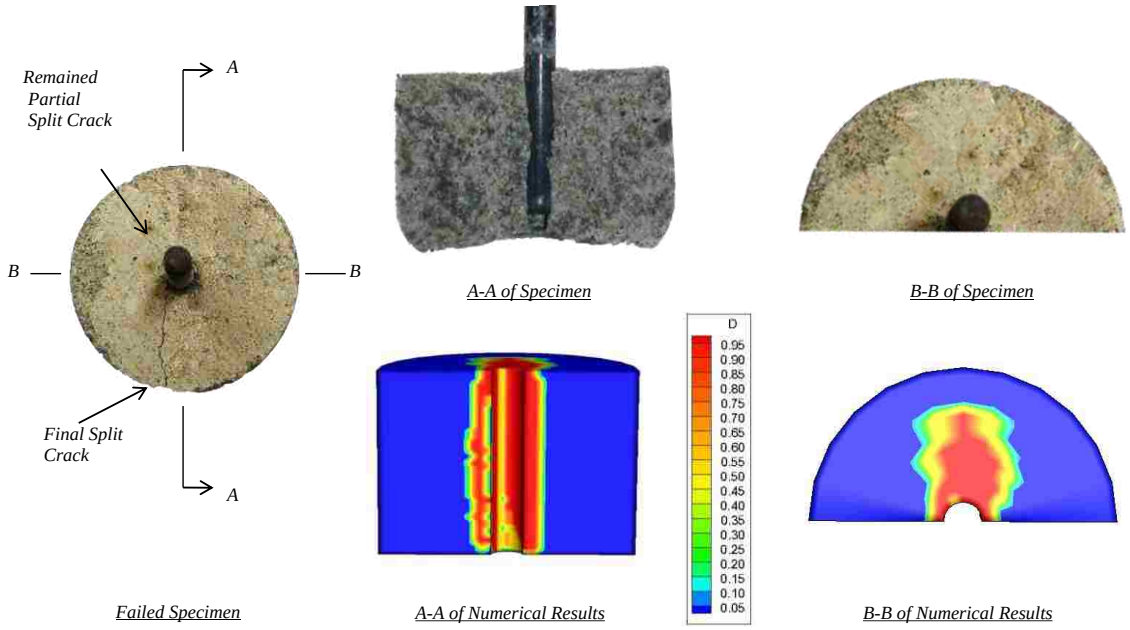

Figure 6.15. Comparison of Failure Mode and Damage Extent: Partially Splitting Failure

6.5. SUMMARY

The proposed 3D probabilistic model in meso scale represents the first attempt of meso-scale modeling and simulations for complex 3D problems with randomly distributed properties of quasi-brittle materials. It has been successfully applied to investigate the mechanical behavior of steel-enamel-mortar cylindrical specimens. Based on extensive analyses and validations, the following conclusions can be drawn:

The proposed meso-scale model can accurately detect the discrete fracture zones in quasi-brittle materials such as mortar. The fracture zones exhibited through the finite element analysis showed their dependence on the randomness of material properties. The simulated fracturing zones were in good agreement with those observed from experiments. Therefore, the proposed meso-scale model is advantageous over the smeared cracking model that can only provide an average damage extent after the discrete fracture has been smeared over the entire mortar cylinder.

The proposed meso-scale model can accurately distinguish and predict fully and partially splitting fracture modes. The fully penetrated radial crack of a mortar cylinder with the embedded enamel-coated pin attached to the mortar was successfully modeled

and represented by the high stress concentration away from the pin-enamel-mortar interface and through the mortar cover. The partially penetrated radial crack of a mortar cylinder with the embedded enamel-coated pin pulled out of the mortar was represented by the high stress concentration at the interface and extended to a critical crack length. With realistic modeling of steel-enamel-mortar interfaces and discrete fracture zones, the fracture growth of quasi-brittle materials can be simulated by the accumulating damage under incremental loading.

The load-slip curves obtained from the finite element analysis can be well correlated with those of the tested specimens deterministically under low loads and statistically under high loads. Under low loads, the linear increase of slip up to the peak stress was accurately simulated by using the average material properties. Under high loads, the post-peak increase of slip until the failure of specimens was compared well with a range of sample simulations using different properties of mortar. These comparisons clearly demonstrate the unique feature of the proposed probabilistic meso-scale model that can accurately represent the heterogeneity of quasi-brittle materials.

7. CONCLUSIONS AND FUTURE STUDIES

7.1. MAIN FINDINGS FROM OVERALL DISSERTATION WORK

In this dissertation, a new unified bond theory has been developed to understand the bond behavior of deformed rebar in quasi-brittle materials. Both local and global bond mechanisms were studied analytically and the close-form solutions for bond strengths were derived. Experimental observations provided insights for simplifications and assumptions in the development of bond strength equations and validated the model predictions with pullout specimens, concrete beams and columns. The empirical bond-slip relation introduced in the global bond model described the shear lag effect between reinforcement and concrete. To understand the concrete fracture process associated with various bond failures, a novel probabilistic concrete model in meso scale was developed and validated with experimental data for the modeling and simulation of complex three dimensional problems with randomly distributed concrete properties. It has been successfully applied to investigate the mechanical behavior of steel-enamel-mortar cylindrical specimens. The overall study has resulted in the following main findings.

7.1.1 The Unified Theory and Local Bond Behavior. (1) The unified local bond theory combined an indentation analogy for near-rebar stress analysis and a hydraulic pressure analogy for concrete confinement analysis. It can be applied to study various failure modes and mechanisms by varying rebar-concrete interface strengths. It can unify two traditionally distinct bond models based on the shear stress analysis and the concrete confinement analysis, respectively.

(2) At low rib spacing-to-height ratios, the potential failure modes near rebar ribs were “plow through” with concrete shear-off along the key line between ribs. At medium and high rib spacing-to-height ratios, the likely failure modes involved concrete crushing and both interface and concrete shear-off at an effective rebar-concrete bearing angle that directly relates the interface behavior to confinement loss. As the rib spacing-to-height ratio increased, the confinement role became more critical to the occurrence of failure modes.

(3) The relative error of predicted average bond strengths by the unified local bond theory is within 6%. The proposed bond equations are more accurate than four existing models available in the literature. They were demonstrated to be robust in all practical application scenarios with various coatings and confinement conditions.

(4) The use of vitreous enamel coating can increase the bond strength of deformed rebar in concrete by approximately 15% because the rebar surface became roughened and its chemical adhesion with concrete was increased. Concrete confinement increased the bond strength of coated rebar in concrete by approximately 15%, which is controlled by concrete splitting.

(5) The failure of the specimens confined by external steel jackets (simulating the effect of transverse reinforcement) was initiated with concrete splitting and followed by shear-off of the concrete keys between rebar ribs as the rebar was pulled out of concrete cylinders. However, the bond slip required from concrete splitting to shear-off was small. In most cases, bond strengths can be approximated at concrete splitting.

(6) Due to increased frictional resistance, enamel-coated rebar was pulled out of the concrete cylinders with a smaller concrete crushing angle than that in uncoated rebar. The crushing angles changed slightly along the length of the rebar mainly due to the uneven distribution of radial stresses.

7.1.2 The Analytical Model with Bond-slip Function and Global Bond Behavior. (7) The local bond theory can be applied to concrete members with lap spliced reinforcement to investigate the global bond behavior of concrete structures. For reinforced concrete beam specimens, the relative errors in the prediction of maximum crack spacing and ultimate load were within 5.56% and 25.6%, respectively. These agreeable comparisons validated the assumption made for the sectional bond-slip distribution function.

(8) The use of enamel coating slightly reduced the maximum crack spacing by 4%-12%, and notably increased the ultimate load. Therefore, the proposed analytical model can be applied to explicitly take into account rebar-concrete interface parameters and study the effect of corrosion protective coating on the rebar-concrete bond behavior.

(9) Enamel coating increased the bond strength of deformed rebar when spliced in concrete beam specimens. As the splice length increased, the ratio of bond strength

between enamel-coated rebar and uncoated rebar first increased from 1.0 to a maximum value of 1.44 and then decreased to 1.0. The bond strength ratio approached 1.0 both at zero splice length and at a very long splice length since the bond strengths in the two cases were governed by concrete splitting and steel yielding, respectively.

(10) Confinement provided by transverse stirrups with 100 mm (4 in.) spacing increased the bond strength of uncoated rebar more rapidly than that of enamel-coated rebar. For enamel-coated rebar, an average of 10% increase in bond strength was observed due to the confinement effect for a splice length over rebar diameter ratio of less than 20. For very long splice lengths, the stress in the spliced rebar (uncoated or coated) is equal to the yield strength and the confinement effect thus becomes negligible.

(11) The increase in bond strength due to enamel coating was reflected mainly in the ultimate load of beam specimens. It had little or no influence on the pre- and post-peak stiffness of the beams. It is unlikely that the coating altered the distribution pattern of slip between the reinforcement and concrete.

(12) The beam specimens with enamel-coated rebar appeared to have a greater number of smaller flexural cracks (in width) than those containing black rebar. This observation indicated that the enamel-coated rebar more effectively transferred stress from concrete to rebar due to stronger rebar-concrete bonding.

(13) Enamel and epoxy coatings respectively increased and reduced the bond strength of deformed rebar in concrete specimens. For practical designs, conservative coating factors should be developed in a splice length over rebar diameter ratio of greater than 35 for enamel-coated rebar and 20 to 35 for epoxy-coated rebar. It is critical to investigate the bond strength of enamel-coated rebar in concrete with long splice lengths, corresponding to initial yielding of steel rebar.

7.1.3 Finite Element Modeling and Fracture Process to Bond Failure. (14) The proposed meso-scale model can accurately detect the discrete fracture zones in quasi-brittle materials. The fracture zones exhibited through the finite element analysis of mortar specimens depended upon the random distribution of material properties. The simulated fracturing zones were in good agreement with experimental observations. Therefore, the proposed model is advantageous over the smeared cracking model that can only provide an average damage extent after the discrete fracture has been smeared over the entire mortar cylinder.

(15) The meso-scale model can accurately distinguish and predict fully and partially splitting fracture modes. The load-slip curves obtained from the model can be well correlated with those of the tested specimens deterministically and statistically under low and high loads, respectively. These comparisons clearly demonstrated the unique feature of the proposed probabilistic model that can accurately represent the heterogeneity of quasi-brittle materials.

7.2. RELATED PUBLICATIONS

The research work presented in Chapters 2-6 can potentially result in five major journal publications. During the Ph.D. study, the author has already published the following papers:

Journal Publications:

Wu, C.L., Chen, G.D., Volz, J.S., Brow, R.K., and Koenigstein, M.L. (2012). "Local bond strength of vitreous enamel coated rebar to concrete," Construction and Building Materials, 35, pp. 428-439.

Wu, C.L., Chen, G.D., Volz, J.S., Brow, R.K., and Koenigstein, M.L. (2013). "Global bond strength of vitreous enamel coated rebar to concrete," Construction and Building Materials, 40, pp. 793-801.

Conference Publications:

Wu, C.L., Chen, G.D., Volz, J.S., Brow, R.K., and Koenigstein, M.L. (2012). "Anchorage strength of enamel coated hooked rebar in normal strength concrete," Proceedings of the 91st Transportation Research Board Annual Meeting, Washington, DC.

Wu, C.L., Chen, G.D., Volz, J.S., Brow, R.K., and Koenigstein, M.L. (2012). "Bond strength of vitreous enamel coated rebar to concrete," Proceedings of the 4th International Symposium on Bond in Concrete: Bond, Anchorage, Detailing, Brescia, Italy.

Wu, C.L., Li, J.B., Chen, G.D., and Li, G. (2012). "Probabilistic modeling of bond behavior of enamel coated steel to mortar," Proceedings of the ASCE Engineering Mechanics and the 11th ASCE Joint Specialty Conference on Probabilistic Mechanics and Structural Reliability, Notre Dame, IN.

7.3. FUTURE STUDIES

This dissertation presents an integrated experimental, analytical, and numerical study on the bond mechanism of deformed rebar in normal strength concrete. Both the unified bond theory and the three dimensional probabilistic model in meso scale represent the first attempt of exploratory nature. The key link between local and global bond models is the bond-slip distribution function that was established based on experimental observations. Although the current study has already laid a solid computational framework for bond behavior studies, several key components and potential future extensions must be further investigated to perfect the theory based on combined indentation and hydraulics pressure analogies and address new applications. Some of the critical technical issues for future studies are summarized as follows:

(1) The effect of transverse reinforcement on local bond mechanics and behavior must be taken into account. The transverse cracking induced by slipping of the wedge formed from concrete crushing can be analyzed to establish a local bond-slip law. The local bond behavior of enamel-coated rebar in high strength and light weight concrete is of great significance to the development of high performance structures.

(2) The analytical global bond model can be extended to include the effect of strain rate and investigate the dynamic performance of enamel-coated rebar in normal strength concrete. Empirical and analytical bond-slip models for enamel-coated rebar will be established to facilitate the engineering design and analysis of reinforced concrete structures.

(3) The Weibull probability distribution still depends upon the configuration of meshes. Geometric properties such as the size and shape of concrete mixtures should be explicitly accounted for by generating subdomains in simulation space.

(4) Non-local theory can be developed and implemented in the meso-scale model with explicit account for the material characteristic length. The weighted damage mechanism in the non-local theory can properly describe the fracture process of quasi-brittle materials.

(5) Coupled interfacial elements should be incorporated into the proposed meso-scale model. To this end, an energy-based coupled interfacial element can be developed and implemented in the proposed model.

(6) The rib geometrical configuration can be incorporated into the finite element model. The failure mechanism of each meso-scale element can be improved to study highly nonlinear behavior due to bearing action of ribs. An improved plasticity model is needed to reduce the computational cost and improve the convergence rate.

(7) The effect of other types of concrete on bond strength is in need of investigation. They include high performance concrete, high strength concrete, ultra-high strength concrete, fiber-reinforced concrete, and self-consolidating concrete.

(8) Bond of rebar with hooks in various structural applications is in need of study. In particular, the coating effect on rebar with end books must be investigated.

BIBLIOGRAPHY

AASHTO (2011). *LRFD Bridge Design Specifications*, American Association of State Highways and Transportation Officials (AASHTO), AASHTO-2011.

ACI (2011). *Building Code Requirements for Structural Concrete*, American Concrete Institute (ACI), ACI 318-11.

ASTM (2007). *Standard Specification for High-Strength Low-Alloy Columbium-Vanadium Structural Steel*, American Society of Testing Methods (ASTM), A572.

ASTM (2009). *Standard Specification for Deformed and Plain Carbon-Steel Bars for Concrete Reinforcement*, American Society of Testing Methods (ASTM), A615/A615M.

ASTM (2010). *Standard Test Methods and Definitions for Mechanical Testing of Steel Products*, American Society of Testing Methods (ASTM), A370.

ASTM (2010). *Standard Guide for Measuring and Reporting Friction Coefficients*, American Society of Testing Methods (ASTM), G115.

Bazant, Z. P, Pang, S. D., Vorechovsky, M., and Novak, D. (2007). "Energetic-statistical size effect simulated by SFEM with stratified sampling and crack band model," *International Journal for Numerical Methods in Engineering*, 71(11), pp. 1297-1320.

Cairns, J. (1979). "Analysis of the ultimate strength of lapped joints of compression reinforcement," *Magazine of Concrete Research*, 31(106), pp. 19-27.

Cairns, J., and Abdullah, R. B. (1996). "Bond strength of black and epoxy-coated reinforcement-a theoretical approach," *ACI Materials Journal*, 93(4), pp. 362-369.

Cairns, J., and Jones, K. (1995). "Influence of rib geometry on strength of lapped joints: an experimental and analytical study," *Magazine of Concrete Research*, 47(172), pp. 253-262.

Canbay, E., and Frosch, R. J. (2005). "Bond strength of lap-spliced bars," *ACI Structural Journal*, 102(4), pp. 605-614.

Cappellini, L. (1996). "On the ultimate capacity of short anchorages embedded in elastic-cohesive cement composites (in Italian)," *MS Thesis*, Milan University of Technology, Milan, Italy, 171 pp.

CEB-FIP Task Group (2000). *Bond of reinforcement in concrete*, CEB-FIP Bond Models, ISBN 2-88394-050-9.

Chamberlin, S. J. (1956). "Spacing of reinforcement in beams," *ACI Journal Proceedings*, 53(7), pp.113-134.

Chen, G., Brow, R., Baird, J., Volz, J., Yan, D., Reis, S., Tan, F., Wu, C., Cheng, X., Werner, C., Tao, X., and Koenigstein, M. (2010). "Enamel-Coated Steel for Life-Cycle Performance of RC Structures – Characterization and Performance Validation," *Proc. Int. Sym. on Life-Cycle Perf. of Bri. & Struct.*, Changsha, China.

Chen, G., Volz, J.S., Brow, R. K, Yan, D. M., Reis, S., Wu, C., Tang, F., Werner, C., and Tao, X. (2010). *Coated steel rebar for enhanced concrete-steel bond strength and corrosion resistance*, Report No. NUTC R236, Rolla, MO.

Chen, W. F., and Saleeb, A. F. (1982). *Constitutive equations for engineering materials, Vol. 2*, Wiley Inter-science, New York, 580 pp.

Choi, O. C., and Lee, W. S. (2002). "Interfacial bond analysis of deformed bars to concrete," *ACI Structural Journal*, 99(6), pp. 750-756.

Choi, O. C., Darwin, D., and McCabe, S. L. (1990b). *Bond strength of epoxy-coated reinforcement to concrete*, SM Report No. 25, Lawrence, KS, 217pp.

Choi, O. C., Hadje-Ghaffari, H., Darwin, D., and McCabe, S. L. (1991). "Bond of epoxy-coated reinforcement: bar parameters," *ACI Materials Journal*, 88(2), pp. 207-217.

Choi, O. C., Hadje-Ghaffari, H., Darwin, D., and McCabe, S. L. (1990a). *Bond of Epoxy-Coated Reinforcement to Concrete: Bar Parameter*, Report No. 90-1, Lawrence, KS, 43 pp.

Cox, J. V., and Herrmann, L. R. (1998). "Development of a plasticity bond model for steel reinforcement," *Mechanics of Cohesive-Frictional Materials*, 3(2), pp.155-180.

Darwin, D., and Graham, E. K. (1993). "Effect of deformation height and spacing on bond strength of reinforcing bars," *ACI Structural Journal*, 90(6), pp. 646-657.

Darwin, D., Mccabe, S. L., Brown, C. J., and Tholem, M. L. (1994). "Fracture analysis of steel-concrete bond," *Fracture and Damage of Quasi-brittle Structures*, Ed. by Bazant, Bittnar, Jirasek and Mazars, pp. 549-556.

Darwin, D., McCabe, S. L., Idun, E. K., and Schoenekase, S. P. (1992). "Development length criteria: Bars not confined by transverse reinforcement," *ACI Structural Journal*, 89(6), pp. 709-720.

Darwin, D., Tholen, M. L., Idun, E. K., Zuo, J. (1996). "Splice strength of high relative rib area reinforcing bars," *ACI Structural Journal*, 93(3), pp. 95-107.

Day, D. C., Weiss, C. A., Malone, P. G., and Hackler, C. L. (2006). "Innovative method of bonding Portland cement concrete to steel using a porcelain interface," *Proceedings of Materials Science and Technology (MS&T) Conference*, Westerville, OH, The American Ceramic Society.

De Anda, L., Courtier, C., and Moehle, J. P. (2004). *Bond strength of prefabricated epoxy-coated reinforcement*, Report No. UCB/EERC/04-01, Berkeley, CA.

Den Uijl, J. A., and Bigaj, A. J. (1996). "A bond model for ribbed bars based on concrete confinement," *HERON*, 41(3), pp. 201-226.

DeVries, R. A. and Moehle, J. P. (1989). *Lap splice strength of plain and epoxy-coated reinforcement*, Report No. UCB/SEMM-91/02, Berkeley, CA, 117 pp.

Eligehausen, R., Ropov, E. P., and Bertero, V. V. (1983). *Local bond stress-slip relationships of deformed bars under generalized excitation*, Report No. UCB/EERC-83/23, Berkeley, CA, 169 pp.

Esfahani, M. R., and Kianoush, M. R. (2005). "Development/splice length of reinforcing bars," *ACI Structural Journal*, 102(1), pp.22-30.

Esfahani, M. R., and Rangan, B. V. (1998). "Local bond strength of reinforcing bars in normal strength and high-strength concrete (HSC)," *ACI Structural Journal*, 95(2), pp. 96-106.

Fernández Ruiz, M., Muttoni, A., and Gambarova, P. (2007). "Analytical modeling of the pre- and post-yield behavior of bond in reinforced concrete," *Journal of Structural Engineering*, 133(10), pp. 1364-1372.

Gambarova, P., and Rosati, G. (1996). "Bond and splitting in reinforced concrete: test results on bar pull-out," *Materials and Structures*, 29 (189), pp. 267-276.

Giuriani, E. (1981). "Experimental investigation on the bond-slip law of deformed bars in concrete," *Proc., IABSE Colloquium on Advanced Mechanics of Reinforced Concrete*, Delft, The Netherland, pp. 121-142.

Hadje-Ghaffari, H., Choi, O. C., Darwin, D., and McCabe, S. L. (1994). "Bond of epoxy-coated reinforcement: cover, casting position, slump, and consolidation," *ACI Structural Journal*, 91(1), pp. 59-68.

Hamad, B. S., and Jirsa, J. O. (1993). "Strength of epoxy-coated reinforcing bar splices confined with transverse reinforcement," *ACI Structural Journal*, 90(1), pp. 77-88.

Hanson, M. T. (1992). "The elastic field for conical indentation including sliding friction for transverse isotropy," *Journal of Applied Mechanics*, 59(2), pp. S123-S130.

Hillerborg, A., Modeer, M., and Petersson, P. E. (1976). "Analysis of crack formation and crack growth in concrete by means of fracture mechanics and finite elements," *Cement and Concrete Research*, 6(6), pp. 773-781.

Idun, E. K., and Darwin, D. (1999). "Bond of Epoxy-Coated Reinforcement: Coefficient of Friction and Rib Face Angle," *ACI Structural Journal*, 96(4), pp. 609-615.

Inglis, C. E. (1913). "Stresses in a plate due to the presence of cracks and sharp corners," *Proc. Inst. Naval Architecture*, 55, pp.219-230.

Johnson, K. L. (1985). *Contact Mechanics*, Cambridge University Press, Cambridge.

Johnston, D. W. and Zia, P. (1982). *Bond characteristics of epoxy coated reinforcing bars*, Report No. FHWA-NC-82-002, Raleigh, NC, 163 pp.

Koch, G. H., Brongers, M. P. H., Thompson, N. G., Virmani, Y. P., and Payer, J. H. (2002). Corrosion Costs and Preventive Strategies in the United States, Publication No. FHWA-RD-01-156, NACE International, Houston TX, USA.

Lackner, R., and Mang, H. A. (2003). "Scale transition in steel-concrete interaction. I: model," *Journal of Engineering Mechanics*, 129(4), pp. 393-402.

Lemaitre, J. (1985). "Coupled elasto-plasticity and damage constitutive equations," *Computer Methods in Applied Mechanics and Engineering*, 51(1-3), pp. 31-49.

Losberg, A., and Olsson, P. A. (1979). "Bond failure of deformed reinforcing bars based on the longitudinal splitting effect of the bars," *ACI Journal*, 76(1), pp. 5-18.

Lutz, L. A., and Gergely, P. (1967). "Mechanics of bond and slip of deformed bars in concrete," *ACI Journal Proceedings*, 64(11), pp. 711-721.

Malvar, L. J. (1992). "Bond of reinforcement under controlled confinement," *ACI Materials Journal*, 89(6), pp. 593-601.

Miller, G. G., Kepler, J. L., and Darwin, D. (2003). "Effect of epoxy coating thickness on bond strength of reinforcing bars," *ACI Structural Journal*, 100(3), pp. 314-320.

Morefield, S.W., Weiss, C. A., Malone, P. G., and Koenigstein, M. L. (2009). "Reactive silicate coatings for protecting and bonding reinforcing steel in cement-based composites," *Corrosion*, NACE International, 09492.

Nielsen, C. V., and Bicanic, N. (2002). "Radial fictitious cracking of thick-walled cylinder due to bar pull-out," *Magazine of Concrete Research*, 54(3), pp. 215-221.

Noghabai, K. (1995). "Splitting of concrete in the anchoring zone of deformed bars-a fracture mechanics approach to bond," *PhD Thesis*, Lulea University of Technology, Lulea, Sweden.

Olofsson, T., and Ohlsson, U. (1995). "A simple fracture mechanics model for mixed-mode failure in concrete," *Proc., International Conference on Fracture Mechanics of Concrete Structures*, pp. 473-482.

Orangun, C. O., Jirsa, J. O., and Breen, J.E. (1977). "A reevaluation of test data on development length and splices," *ACI Structural Journal*, 74(3), pp. 114-122.

Pantazopoulou, S. J., and Papoulia, K. D. (2001). "Modeling cover-cracking due to reinforcement corrosion in RC structures," *Journal of Engineering Mechanics*, 127(4), pp. 342-351.

Rehm, G. (1957). "Fundamental law of bond," *Proc., Symposium on Bond and Crack Formation in Reinforced Concrete*, RILEM, Paris, Tekniska Hogskolans Rotaprinttrychkeri, Stockholm.

Rehm, G. (1961). "Uber die Grunlagen des Verbundes Zwischen Stahl und Beton," *Deutscher Ausschuss fur Stahlberton*, 1381, pp. 59, (C & CA Library Translation No. 134, 1968. "Basic principle of the bond between steel and concrete.").

Reinhardt, H. W. (1992). "Bond of steel to strain-softening concrete taking account of loading rate," *Fracture Mechanics of Concrete Structures*, Elsvier, London, pp. 809-820.

Reynolds, G. C., and Beeby, A. W. (1982). "Bond strength of deformed bars," *Bond in Concrete*, Applied Science Publishers, London, pp. 434-445.

Richard, B., Ragueneau, F., Cremona, C., Adelaide, L., and Tailhan, J. L. (2010). "A three-dimensional steel/concrete interface model including corrosion effects," *Engineering Fracture Mechanics*, 77(10), pp. 951-973.

Romstad, K. M., Taylor, M. A., and Hermann, L.R. (1974). "Numerical biaxial characterization for concrete," *Journal of Engineering Mechanics*, 100(5), pp. 935-948.

Rosati, G., and Schumm, C. (1992). "Modeling of local bar-to-concrete bond in reinforced concrete beams," *Proc., International conference on Bond in Concrete-From Research to Practice*, pp. 12-43.

Russo, G., Pauletta, M., and Mitri, D. (2009). "Solution for bond distribution in asymmetric R.C. structural members," *Engineering Structures*, 31(3), pp. 633-641.

Sneddon, I. N. (1948). "Boussinesq's problem for a rigid cone," *Mathematical Proceedings of the Cambridg Philosophical Society*, 44(4), pp. 492-507.

Soretz, S., and Holzenbein, H. (1979). "Influence of rib dimensions of reinforcing bars on bond and bendability," *ACI Journal Proceedings*, 76(1), pp. 111-128.

Tang, C. A., and Zhu, W. C. (2003). *Concrete damage and fracture-numerical test*, Science Press, Beijing.

Tang, F., Chen, G., Brow, R. K., Volz, J. S., and Koenigstein, M. L. (2012). "Corrosion resistance of steel rebar coated with three types of enamel," *Corrosion Science*, 59, pp. 157-168.

Tang, F., Chen, G., Brow, R., Volz, J., and Koenigstein, M. (2012). "Corrosion Resistance of Steel Rebar Coated with Three Types of Enamel," *Corr. Sci.*, 59, pp. 157-168.

Tang, F., Chen, G., Volz, J., Brow, R., and Koenigstein, M. (2013). "Cement-modified Enamel Coating for Enhanced Corrosion Resistance of Steel Reinforcing Bars," *Cement & Conc. Comp.*, 35(1), pp. 171-180.

Tassios, T. P. (1979). "Properties of bond between concrete and steel under load cycles idealizing seismic actions," *Proc., AICAP-CEB Symposium*, Rome, CEB Bulletin, 131, pp. 67-122.

Tepfers, R. (1973). "A theory of bond applied to overlapped tensile reinforcement splices for deformed bars," *Publication No. 73:2, Division of Concrete Structures*, Charlmers University of Technology, Goteborg, 328 pp.

Treece, R. A., and Jirsa, J. O. (1985). *Bond Strength of Epoxy-Coated Reinforcing Bars*, PMFSEL Report No. 87-1, Austin, TX, 85 pp.

Treece, R. A., and Jirsa, J. O. (1989). "Bond strength of epoxy-coated reinforcing bars," *ACI Materials Journal*, 86(2), pp. 167-174.

van der Veen, C. (1990). "Cryogenic bond stress-slip relationship," *Delft University of Technology, Doctoral thesis*, Delft, The Netherland, 111 pp.

Wang, H. (2009). "An analytical study of bond strength associated with splitting of concrete cover," *Engineering Structures*, 31(4), pp. 968-975.

Wang, X., and Liu, X. (2003). "A strain-softening model for steel-concrete bond," *Cement and Concrete Research*, 33(10), pp. 1669-1673.

Weiss, W. J., Guler, K., and Shah, S. P. (1999). "An experimental investigation to determine the influence of size on the flexural behavior of high strength concrete beams," *Proc., the Fifth International Symposium on the Utilization of High Strength/High Performance Concrete*, Sandefjord, Norway, 1, pp. 709-718.

Wright, J. K., and MacGregor, J. G. (2009). *Reinforced concrete mechanics and design (5th ed.)*, Pearson and Prentice Hall, Upper Saddle River, New Jersey, 1112 pp.

Wu, C., Chen, G., Volz, J. S., Brow, R. K., and Koenigstein, M. L. (2012). "Local bond strength of vitreous enamel coated rebar to concrete," *Construction and Building Materials*, 35, pp. 428-439.

Yan, D. M, Reis, S., Tao, X., Chen, G., Brow, R. K., and Koenigstein, M. L. (2012). "Effect of chemically reactive enamel coating on bonding strength at steel/mortar interface," *Construction and Building Materials*, 28(1), pp. 512-518.

Yang, Z. J., Su, X. T., Chen, J. F., and Liu, G. H. (2009). "Monte Carlo simulation of complex cohesive fracture in random heterogeneous quasi-brittle materials," *International Journal of Solids and Structures*, 46(9), pp. 3222-3234.

Zhu, W. C., Teng, J. G., and Tang, C. A. (2004). "Mesomechanical model for concrete. Part I: model development," *Magazine of Concrete Research*, 56(6), pp. 313-330.

Zuo, J., and Darwin, D. (2000). "Splice strength of conventional and high relative rib area bars in normal and high-strength concrete," *ACI Structural Journal*, 97(4), pp. 630-641.

VITA

Mr. Chenglin Wu was born in Luoyang, Henan, the People's Republic of China. He was admitted to Tongji University, Shanghai, China in 2002 and received his B.S. degree in Civil Engineering in 2006. Mr. Wu began his graduate studies at Lawrence Technological University, Michigan, USA, and received his M.S. degree in Civil Engineering in 2009.

Since August 2009, Mr. Chenglin Wu has been enrolled in the Ph.D. Program in Civil Engineering at Missouri University of Science and Technology (formerly University of Missouri-Rolla), Rolla, Missouri, USA. He has served as both a Graduate Research Assistant and Graduate Teaching Assistant between August 2009 and December 2013 in the Department of Civil, Architectural, and Environmental Engineering. During this period, his research interests have been focused on experimental, analytical and computational solid mechanics, and vision-based, computer aided non-contact sensing techniques. Based on his graduate research work, he has authored and co-authored seven journal articles (four as the first author, two as second author, and one as the third author). In May 2014, he will receive his Ph.D. degree in Civil Engineering at Missouri University of Science and Technology, Rolla, Missouri, USA.